Gradient Smoothing in Finite Elasticity: near-incompressibility

Chang-Kye Lee

Supervisors: Prof Stéphane P. A. Bordas

Dr Pierre Kerfriden

A thesis submitted to Cardiff University in partial fulfilment of the requirement for the degree of Doctor of Philosophy

School of Engineering

Cardiff University

Cardiff, Wales, UK,

August 11, 2016

Progress is impossible without change,
and those who cannot change their mind
cannot change anything.
— George Bernard Shaw

To family...

Acknowledgements

Completion of this thesis would not have been possible without the support of people around me. First of all, I extremely appreciate my supervisor Professor Stéphane P. A. Bordas for his supervision, guidance and supports for the last four years. His consistent encouragement and valuable advice on both research and my career have been priceless. Furthermore I would like to thank Dr. Pierre Kerfriden for all discussions on research and conversation on other topics. I am also grateful to Dr. L. Angela Mihai and Dr. Jack. S. Hale for brilliant suggestions and concise comments for my topic. I would especially like to acknowledge my friends and colleagues I have met in my research group for making friendship and enjoyable moment in Cardiff.

I would like to express a special note to Professor Sang-Jin Lee. He has inspired and encouraged me to grow as a researcher.

Lastly but the most important, a special thank to my family. Words cannot express how grateful I am to my grandmother, father, mother and my brother. Without their unconditional love, consistent supports and trust, I cannot see this achievement come true. I owe a debt of gratitude from them.

Cardiff, March 30, 2015 Lee, Chang-Kye

Abstract

This thesis presents the extension of the gradient smoothing technique for finite element approximation (so-called Smoothed Finite Element Method (S-FEM)) and its bubble-enhanced version for non-linear problems involving large deformations in nearly-incompressible and incompressible hyperelastic materials.

Finite Element Method (FEM) presents numerous challenges for soft matter applications, such as incompressibility, complex geometries and mesh distortion from large deformation. S-FEM was introduced to overcome the challenges mentioned of FEM. The smoothed strains and the smoothed deformation gradients are evaluated on the smoothing domain selected by either edge information, nodal information or face information.

This thesis aims the extension of S-FEM in finite elasticity as a means of alleviating locking and avoiding mesh distortion. S-FEM employs a "cubic" bubble enhancement of the element shape functions with edge-based and face-based S-FEMs, adding a linear displacement field at the centre of the element. Thereby bubble-enhanced S-FEM affords a simple and efficient implementation.

This thesis reports the properties and performance of the proposed method for quasi-incompressible hyperelastic materials. Benchmark tests show that the method is well suited to soft matter simulation, overcoming deleterious locking phenomenon and maintaining the accuracy with distorted meshes.

Abbreviations

Notations

A_k Area of smoothing domain

$a(\cdot,\cdot)$ Bilinear form

$\mathbf{b}$ Element force vector

$\mathbf{B}$ The left Cauchy-Green tensor

$\mathbf{B}_0, \mathcal{B}, \tilde{\mathbf{B}}_0, \tilde{\mathcal{B}}$ The strain-displacement matrices

$\mathbf{C}, \tilde{\mathbf{C}}$ The right Cauchy-Green tensor

$\mathbb{C}$ Fourth-order elasticity tensor

$D\mathcal{R}(\mathbf{u}) \cdot \mathbf{u}$ The energy fucntion directional derivatives

$\mathbf{E}$ Green-Lagrange strain tensor

E Young's modulus

$\mathbf{f}$ The body force

$\mathbf{F}, \tilde{\mathbf{F}}$ The deformation gradient tensor

$\tilde{\mathbf{F}}$ Smoothed deformation gradient

$\mathbf{g}$ The traction

GDof Global degrees of freedom

Abbreviations

G_k Set of nodes

$\mathbb{H}^1$ Hilbert space

I_1, I_2, I_3 The principal invariants of a second-order tensor

i, j, k, l Indices

k Target edge, node or face

$\mathbf{K}, \tilde{\mathbf{K}}$ Stiffness matrix

L^2 Lebesque space

$\mathbf{n}$ Outward normal vector

N_{SD} Number of smoothing domain

p Pressure

$\mathbf{P}$ The first Piola-Kirchhoff stress tensor

$\mathcal{R}(\mathbf{u})$ The energy function

$\mathbf{S}$ The second Piola-Kirchhoff stress

$\mathbf{u}$ Displacement fields

$\mathbf{u}^{\mathrm{h}}$ Trial functions

$\mathbf{v}^{\mathrm{h}}$ Test functions

$\mathcal{W}$ Strain energy function

x Coordinates of current configuration

X Coordinates of initial configuration

$\alpha_{\text{distorted}}$ Magnitude of mesh distortion

Γ_N Natural boundary

Γ_k^s Boundary of smoothing domain

$\boldsymbol{\varepsilon}$ Infinitesimal strain tensor

κ Bulk moudulus

$\lambda_1, \lambda_2, \lambda_3$ Eigenvalues

λ Lamé's first parameter

μ Lamé's second parameter (shear modulus)

ν Poisson's ratio

Φ Weight function

Ψ Shape functions

Ω Domain of current configuration

Ω_0 Domain of initial configuration

Ω_k^s Smoothing domain

∇ Gradient operator

$\boldsymbol{\sigma}$ Cauchy stress tensor

(r, θ, z) Cylindrical coordinates

(ξ, η) Natural coordinates

Acronym

ALE Arbitrary Lagrangian-Eulerian

Abbreviations

BCs Boundary Conditions

bES-FEM Bubble-enriched Edge-based Smoothed Finite Element Method

bFS-FEM Bubble-enriched Face-based Smoothed Finite Element Method

CS-FEM Cell-based Smoothed Finite Element Method

DOFs Degrees of Freedoms

ES-FEM Edge-based Smoothed Finite Element Method

FEM Finite Element Method

FEs Finite Elements

FS-FEM Face-based Smoothed Finite Element Method

NEM Natural Element Method

NS-FEM Node-based Smoothed Finite Element Method

PK2 the second Piola-Kirchhoff stress tensor

S-FEM Smoothed Finite Element Method

SCNI Stabilized Conforming Nodal Integration

Contents

List of Figures

List of Tables

1 Introduction

1.1 Introduction

Linear elasticity is a suitable assumption in many engineering applications where strains are small and are proportional to the loads. However many engineering and natural applications involve soft matter; hydrogels, polymers, rubbers and biological structures such as human organs and soft tissues. These materials are potentially subject to very large, non-linear (often inelastic) deformations. Non-linear problems are very sensitive to material models, load and even meshes, and advanced approximation schemes and solution procedures are required to solve the equations. It is thus important to design approaches which are well-suited to their robust and accurate simulation [15, 21, 40]. In particular, the design of a simple and robust approach to model and solve patient specific models of human organs for computerised surgical simulation and computer guided therapy is an important issue in surgical simulation, planning and guidance.

The first step to solve such problems numerically is to obtain and adequate discretisation of the organs as automatically and rapidly as possible, so as to fit within the time scales required by clinical practice.

Tetrahedral elements are the best suited to automatic generation and there exist schemes that allow the generation of millions of tetrahedral elements per second [134].

However, those elements are also notorious for their excessive stiffness and their sensitivity to volumetric locking. Hexahedral (HEX) elements are more insensitive to these deleterious effects, but generating HEX meshes automatically remains a serious challenge in spite of recent advances in polyhedral element mesh generation [26] and element technology [99, 147, 149, 11]. Other approaches to increase accuracy is the use of higher order approximation such as higher order tetrahedral elements, isogeometric analysis or NURBS-based analyses [102, 48, 141] and meshless methods [103]. However, these approaches are non-standard, computationally expensive and cannot be easily implemented within existing finite element codes. Moreover, they are computationally expensive, and as far as higher-order finite elements, those tend to be sensitive to mesh distortion.

This thesis focuses on the development of a simple alternative to enable the use of linear tetrahedral elements for quasi-incompressible large deformations. The elements sought should be insensitive to mesh distortion, to volumetric locking, should be easily implemented in existing finite element code, and, if possible, adapted to GPU computing in order to enable real-time simulations [39].

1.2 Competing numerical approaches

In this section, numerical approaches proposed to tackle the difficulties of the FEM are reviewed, in particularly concerning incompressibility. These approaches are commonly used in either solid or fluid mechanics and it has been shown that locking, instability or over-stiff behaviour can be effectively handled.

Nodally averaged elements. Bonet and Burton introduced the idea of nodally averaged pressure for a linear tetrahedral element in a nearly-incompressible hyperelastic model in 1998 [18]. The volumetric strains were computed at nodes and a nodal pressure was averaged over elements. Although the proposed tetrahedra performed very well comparing to hexahedra, their computational time is more expensive than the standard hexahedra. Dohrmann et al. [49] introduced the node-based uniform strain element which is closely related to the average nodal pressure technique. Since previous researches were concerned with linear elasticity, Bonet et al. [19] extended the nodal averaging scheme to large strains. However it is shown that this approach still suffers from overly stiff behaviour in the case of bending problems [20].

In the context of explicit dynamics, Andrade Pires et al. [1] introduced an implicit version of the nodal averaging approach. They proposed the average nodal volume change ratio defined by the fraction of initial nodal volume and deformed nodal volume. Then, using the proposed volume ratio, the modified deformation gradient F-bar was evaluated. Since the F-bar technique could not be directly used for linear triangular and tetrahedral elements, the extended F-bar approach was introduced for low-order FEs [45]. However, the tangent matrix requires additional treatments to assemble globally because rows and columns of the tangent stiffness matrix represent the degrees of freedom of different elements on the different patches [45].

Stabilised elements. Stabilised finite element methods were introduced to prevent numerical instabilities, especially for fluid dynamics. They allow the use of equal-order interpolation for pressure and velocity. This makes their methods attractive for large-scale multi-physics simulations conquered to mixed-Galerkin methods. Generally the methods can be classified into two approaches: adding a

stabilising term (so-called least-square stabilisation) for fluid mechanics and adding a displacement field (so-called bubble functions) for non-linear solid mechanics [30, 133].

Stabilised finite element methods for nearly-incompressible problems in linear elasticity were introduced by Franca et al., in 1988 [55] and Douglas and Wang, in 1989, proposed an absolstely stabilised FEM [51]. Klaas et al. extended the concept of stabilisation into mixed finite element method [71].

Since Hughes introduced a sub-grid scale stabilisation method [66] for the scalar convection-diffusion equation, Chiumenti et al. [36] extended the approach to solid mechanics. This idea stabilises elastic incompressible formulations for quadrilateral and triangular elements. The concept of sub-grid scales was employed in mixed formulations to stabilise the displacement/pressure (u/p) formulations for incompressible and nearly-incompressible materials using orthogonal sub-grid scale method (Cervera et al. [32]). Moreover, stabilisations were extended to meshfree Galerkin methods for incompressible Navier-Stokes ideas [56].

Caylak and Mahnken [30] introduced a mixed finite element formulation with area bubble functions to stabilise the formations for linear and non-linear elastic materials.

Mixed and enhanced elements. Mixed and enhanced elements also can be considered. The governing equation is explained by velocity and pressure for the linear incompressible problem in fluid mechanics [37] and the equation is expressed by displacement and pressure for the linear incompressible problems in solid mechanics [150, 167]. Pantuso and Bathe introduced $u/p/e$ formulations combined with displacement, pressure and enhanced strain for linear analysis [129] and for problems involving large strains [130]. Kasper and Taylor [69] introduced

a mixed-enhanced strain formulation based on the Hu-Washizu variational principle with three approximation fields: displacements, strains and stresses in the incompressible limit in linear elasticity. Lovadina and Auricchio [92], using the concept proposed by Pantuso and Bathe [129], proposed displacement/pressure formulation for three-noded triangular element (T3) for linear incompressible materials, using assumed strain methods. Schröder et al. [139] developed tetrahedral elements in the incompressible limit based on a Hu-Washizu functional derived by deformation, co-factor and volumetric dilatation.

Auricchio et al.[4] stabilised the discrete formulation for incompressible materials using the MINI mixed finite elements and quadrilateral mixed-interpolated elements, and Cervera et al. [31] introduced a mixed finite element formulation based on their previous study in 2003 [32], stabilising stress-displacement and strain-displacement formulations using linear/linear interpolations in triangular elements and bilinear/bilinear interpolations in quadrilateral elements for non-linear problems.

Mahnken et al. [94] derived a five field weak formulation involving compatible displacements, incompatible displacements, pressure, enhanced strains and stresses, and three field weak formulations for a mixed method with incompatible modes - displacements are split into a compatible and an incompatible part - and an enhanced strain method. To derive a mixed finite element, area bubble functions were used to augment the displacement and strain fields. Later they extended the idea to non-linear problems [93]. Recently Lamichhane [74] proposed a mixed finite element method for nearly incompressible materials and Stokes equations in non-linear elasticity. In this study, displacements and velocity fields were derived by space enrichment with bubble functions, however the pressure field was approximated by dual meshes introduced in [73] for quadrilateral and hexahedral elements.

While mixed and enhanced approach prevent locking in the incompressible limit, it was shown that enhanced simplex elements commonly lead to unstable methods for large deformation problems [5, 36].

Non-mesh based methods. Non-mesh based techniques often called meshfree (or meshless) methods [14, 81, 83] are another option. A general review of the field was done by Nguyen et al. [103] and Belytsckho et al. [13] presented a notable study for stability. These techniques improve the accuracy on heavily distorted nodal layout, however Galerkin meshfree methods are more computationally costly than the FEM and the locking problem is still a challenging problem [34, 65].

Nodal integration is often employed in meshfree/meshless methods [76, 131, 148]. In nodal integration, all discretised variables are defined at nodes and the integration is much faster than Gaussian integration [12]. In Beissel and Belytschko [12], it was shown that stabilised nodal integration in element-free Galerkin (EFG) decreases the stability. This was attributed to vanishing derivatives at the nodes. To avoid nodal integration instability, Chen et al. [33, 35] introduced a stabilised conforming nodal integration (SCNI) technique into the EFG approximation. This concept was applied to plastic limit analysis [77], error estimation [75]. Puso and Solberg improved the study [49], augmenting the stabilisation term with a nodal integration scheme [132]. This approach was extended to Mindlin-Reissner plates to remove shear locking, introducing Kirchhoff mode reproducing conditions into the construction of shape functions for the translational and rotational degrees of freedom in Wang and Chen [152].

1.3 Strain smoothing

The approaches mentioned in the previous section perform very well for either incompressible or quasi-incompressible materials, they however still may encounter difficulties that should be overcome, e.g. instability of linear elements in large deformations [92, 130, 155], sensitivity to mesh distortion as well as overly-stiff behaviour.

Herein we consider *gradient smoothing* as a possible way forward. Gradient smoothing was shown for linear elastic materials to prevent locking and alleviate most of the deleterious effects of element distortion. The basic idea of gradient smoothing relies on stabilised conforming nodal integration (SCNI) proposed by Chen et al. [33, 35], and extended to the natural element method (NEM) by Yoo et al. [161].

Liu et al. [82] combined the idea of strain smoothing to FEM and called the method, the smoothed finite element method (S-FEM). Since S-FEM was introduced, its properties have been studied from a theoretical viewpoint: Liu et al. [82] studied the performance of triangular and quadrilateral sub-domains for triangular, quadrilateral and polygonal elements, and explained the relation between strain smoothing approximation and Hellinger-Reissner principles [85]. Also, the convergence of displacement and strain energy error norms are given in [88]. Different types of S-FEM were introduced depending on the construction of the smoothing domains [84]: cell-based (CS-FEM), edge-based (ES-FEM), node-based (NS-FEM) and face-based (FS-FEM). In such approaches, the mesh structure is used to construct the sub-domain used as smoothing domain (Fig. 1.1). The sub-domain can be designed as not only triangle but also arbitrary polygonal geometries. CS-FEM uses bilinear quadrilateral (Q4) element divided

quadrilateral smoothing domains [85]. Bordas et al. [25] showed the important properties of the four-noded Quadrilateral CS-FEM: (1) one smoothing domain is equivalent to under-integrated FEM Q4 (quasi-equilibrium element) and increases the stress accuracy, (2) four smoothing domains show intermediate behaviour, and (3) the accuracy of displacements is increased when the number of smoothing domains is ($N_{SD} \rightarrow +\infty$). In contrast to CS-FEM, ES-FEM, NS-FEM and FS-FEM use linear triangular and tetrahedral elements with triangular and tetrahedral smoothing domains, respectively. The target smoothing domain of ES-FEM is created by smoothing domains sharing a target edge of each elements[1] and the smoothing domains, in NS-FEM, are built node-wise[2]. Face-based S-FEM was developed for 3D problems analogously to edge-based approach in 2D. A linear simplex tetrahedral element is used in FS-FEM and therefore its smoothing domains are also tetrahedrons. Similarly to ES-FEM, the smoothing domains of FS-FEM are built by the combination of smoothing domains associated by target face of each finite element. Node-based smoothing is similarly extended from 2D to 3D.

Cell-based smoothed finite element method (CS-FEM). Early studies on S-FEM, in general, showed remarkable features of S-FEM: (1) Liu et al. [85] in 2007 presented the theoretical bases of S-FEM, the Galerkin weak form was formulated by the Hu-Washizu mixed variational principle, and indicated numerically that four-quadrilateral smoothing domains in each Q4 element was optimal, (2) Dai et al. investigated suitable shape functions for polygonal elements and showed stable and accurate results [44], and (3) Bordas and Natarajan studied the construction of shape functions in physical space [23].

Additional applications of CS-FEM were studied by Liu's team, e.g. plane problems

[1] Target edge is one of edges of the finite elements.
[2] Target node is a field node of the finite elements.

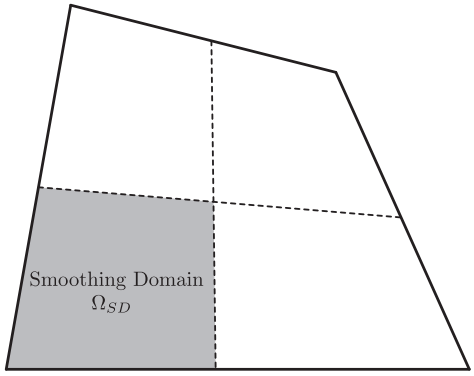

(a) Smoothing Domain of CS-FEM

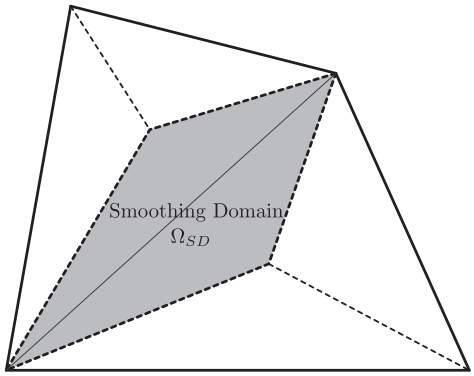

(b) Smoothing Domain of ES-FEM

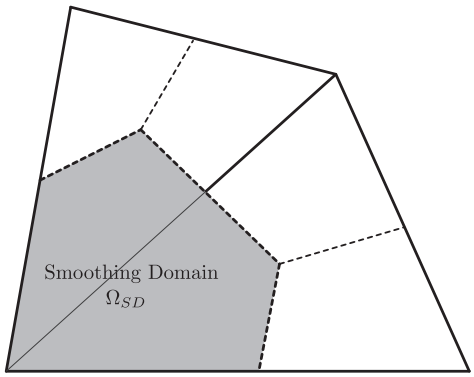

(c) Smoothing Domain of NS-FEM

Figure 1.1: Smoothing domains of S-FEM models: (a) four-noded element is divided into four smoothing domains for Cell-based S-FEM, (b) three-noded element is divided into three smoothing domains and four-noded smoothing domain is constructed for Edge-based S-FEM and (c) three-noded element is divided into three smoothing domains and six-node smoothing domain is constructed for Node-based S-FEM

in kinematic limit analysis (Le et al. [78]) and they provided accurate solutions with fewer degree of freedoms (DOFs) than FEM. Cui et al. [42] solved linear and geometrically non-linear plate and shell problems avoiding shear locking and reaching faster convergence. Nguyen-Xuan et al. smoothed the curvature for Reissner-Mindlin plates and shells [118]. Shear locking for thin plates and shells is avoided by the proposed method, although the performance of the method for heavily distorted meshes was not satisfying. This problem was addressed by Wu et al. [157] who combined the curvature smoothing and an enhancement through the mixed interpolation technique. Moreover further applications of CS-FEM were introduced by Dai and Liu [43] for the free and forced vibration analyses for 2D dynamic problems and in acoustics by Yao et al. [159], respectively. To solve forced vibrations Dai and Liu [43] employed implicit and explicit time integration approaches. Yao et al. [159] used the cell-based acoustic pressure gradient smoothing operation and obtained accurate results for distorted meshes and high wave number without increasing computational efforts (2D acoustic problems). Bordas' team created enriched extensions of S-FEM: SmXFEM in [8, 24, 25, 166] and proposed adaptive schemes in fracture mechanics [116] using node/edge based approaches.

Edge-based smoothed finite element method (ES-FEM). Due to its simplicity and efficiency, ES-FEM is one of the most popular strain smoothing approaches. The following features of ES-FEM are given by Liu and his colleagues [84, 86]: 1) any element shape can be used but it normally prefers a triangular mesh, 2) the smoothed stiffness matrix is computed over smoothing domains associated with a target edge and 3) a domain-based selective ES/NS-FEM can alleviate the locking problems because ES-FEM itself does not effectively handle them.

ES-FEM with the stabilised discrete shear gap method (DSG), which was proposed

for static, free vibration and buckling analysis, was used for Reissner-Mindlin plates by Nguyen-Xuan et al. [118]. Accuracy of low-order Reissner-Mindlin plate elements often degrades due to shear locking, however the authors prove in [118] that ES-FEM improves the quality of such elements, avoiding locking issues. Nguyen-Xuan et al. [117] employed ES-FEM for static and frequency analyses and solved 2D piezoelectric problems. ES-FEM provides accuracy, insensitivity to mesh distortion and softer stiffness also for piezoelectric models stability. On the other hand, Cui et al. [41] formulated ES-FEM based on Hencky's deformation theory to solve elastic-plastic problems and which alleviated over-stiffness. Moreover a structural-acoustic problem: plate fluid interaction was investigated by He et al. [61], coupling ES-FEM and FEM. In their study, the solid domain was discretized by ES-FEM and the fluid domain was formulated by FEM. A rlecent study is a 3D spatial membrane structure under large deformation, rotation and strain done by Zhang and Liu [165]. Stresses and strains were smoothed in local coordinates and the rigid body motion was removed by the transformation from the global Cartesian coordinates to the local coordinates.

Node-based smoothed finite element method (NS-FEM). In NS-FEM, similarly to ES-FEM, strains/stresses and the stiffness matrix are smoothed and computed over the smoothing domain [84]. A notable character of NS-FEM is that the method provides an upper-bound solution, for problems with non-homogeneous Dirichlet boundary conditions (BCs) and zero external forces, whereas ES-FEM gives a lower-bound solution under the same condition [107]. Furthermore NS-FEM is able to use n-sided arbitrary polygonal elements and is immune to any locking issue [87].

Similarly to CS-FEM and ES-FEM, static, free vibration and mechanical/thermal buckling problems for Reissner-Mindlin plates were solved with NS-FEM and

using the discrete shear gap method by Nguyen-Xuan et al. [119]. In addition, 2D and 3D visco-elastoplastic analyses were addressed by Nguyen-Thoi et al. [111]. Perfect visco-elastoplasticity and visco-elastoplasticity with isotropic hardening and linear kinematic hardening were considered. Adaptive analyses were also considered by Nguyen-Thoi et al. [109], enriched by NS-FEM. They proposed an error indicator based on the recovery strain scheme for a three-node triangular (T3) element. Stresses and strains were computed at field nodes and the T3 element was divided into two new sub-triangles by connecting the top field node and mid-point of base edge of element.

Face-based smoothed finite element method (FS-FEM). In 3D, the face-smoothed FEM (FS-FEM) was introduced by Nguyen-Thoi et al. [105]. Smoothing domains of FS-FEM are constructed using faces of tetrahedral or hexahedral elements. Similar to other S-FEM, the stiffness matrix and strain are smoothed over the smoothing domains associated with element faces [106].

Nguyen-Thoi et al. [106] extended the concept of ES-FEM to 3D solid mechanics problems. They presented that: 1) the two-field Hellinger-Reissner principle for FS-FEM has displacements as unknowns while those of mixed formulation in FEM are stresses or strains, 2) FS-FEM gives more accurate results than FEM for linear and geometrically non-linear analyses, and 3) a combined FS/NS-FEM suppresses volumetric locking in the incompressible limits for linear materials. Jiang et al. [68] used the same method, selective FS/NS-FEM, for nearly-incompressible anisotropic materials. FS-FEM (and 3D-ES-FEM) was used for the deviatoric part of deformation and NS-FEM was used for the volumetric parts. They improved a four-node tetrahedral (T4) element to prevent locking. A FS-FEM combined with the method of Carstensen and Klose [29] was proposed by Nguyen-Thoi et al. [110] for perfect visco-elastoplasticity and visco-elastoplasticity with isotropic

hardening and linear kinematic hardening. Further application for structural-acoustic problems was done by Li et al. [80] using ES-FEM for the deformable solid (plates) and FS-FEM for the acoustic fluid domain. Heat transfer and thermal mechanical problems were studied in Feng et al. [54] using the von Mises yield criterion for non-isothermal and isotropic hardening conditions.

1.3.1 Key contributions

The aforementioned section indicates the clear benefits of the smoothed FEM to alleviate locking and to mesh distortion sensitivity. Soft matter is a crucial area of physics and mechanics, with wide industrial applications (e.g. tyre manufacturing and optimisation). A soft matter is also widely encountered in nature: soft tissues, organs, cells, biofilms, hydrogels, and is used to build tissue scaffolds [38, 39, 46]. For this, it is mandatory that meshes are generated automatically. One approach is the use of linear TETs which are also prone to lock. This work investigates the potential of strain smoothing for such applications. Although existing S-FEM research showed that the method is able to overcome such concerns in linear incompressibility or quasi-incompressibility, non-linear elasticity still opens vast unexplored area.

This work focuses on the development of a number of variants of the smoothed finite elements to simulate the large deformations of nearly-incompressible and incompressible soft matter. The following novelties are introduced in this work:

- The weak form for the smoothed finite element method in finite elasticity is expressed in Chapter 4.

  The smoothed deformation gradient, essential in finite elasticity approximation, is introduced and approved in section 4.2 and appendix B. Detailed formulations for the smoothed strain-displacement and the smoothed tangent

stiffness matrices are also introduced in section 4.2.

Using the introduced smoothed formulations, the smoothed global system of equations is solved by a Newton-Raphson method.

- Bubble stabilisation is coupled to edge-based and face-based S-FEMs in Chapter 5.

  The "Cubic" bubble functions for 2D and 3D, that satisfy the partition of unity, are transformed from the basic bubble functions in section 5.1. The mixed formulations in the framework of S-FEM are given in section 5.2.

  In section 5.3, the bubble-enriched ES-FEM is shown that it is very effective to alleviate locking in finite elasticity without any additional terms in the strain smoothing approximation.

1.4 Overview

This work endeavours to develop and improve the quality of low-order FEs for incompressible and nearly-incompressible hyperelastic materials undergoing large deformations. Variants of a novel numerical approach, so-called smoothed finite element (S-FEM) are proposed and discussed. The work is organised as three main parts.

Chapter 2 explains non-linearity and material descriptions which are commonly used. Materials involving large deformations, particularly hyperelastic models, are introduced. In hyperelastic models, relation of stress-strain is derived from a strain energy function and this models are path-dependent. In this work, to describe non-linear behaviour, a Lagrangian description and a neo-Hookean model are used.

The combination of the strain smoothing technique and FEM in linear elasticity is recalled in Chapter 3.

Chapter 4 presents the strain smoothing approach for finite elasticity in general and hyperelastic materials in particular. The non-linear equilibrium equations solved by Newton-Raphson are given using both a finite element approximation and a smoothed finite element approximation. In the same manner as the smoothed strains in S-FEM in linear elasticity, the smoothed deformation gradient is built using smoothing domains. The stored energy function of neo-Hookean material is derived by the smoothed deformation gradient.

Edge-based S-FEM (ES-FEM) enriched by the "Cubic" bubble functions in finite elasticity is introduced in Chapter 5. Since the standard ES-FEM cannot effectively avoid locking, bubble function enrichment/stabilisation associated with an internal node located at the centroid of each T3 element gives excellent locking-free results. Benchmark tests undergoing large deformation are discussed and provided with all details necessary to be reproduced, including Dirichlet and Neumann boundary conditions and full analytical solutions. Such fully developed solutions are rare in the literature which makes verification tedious.

Finally the conclusions of the work, remarks and as well as the suggestions are explained in Chapter 6.

2 Fundamentals

Material descriptions are used to describe motion of a continuum body with respect to coordinates and time and are also required for the governing equations and their descretisation. Fig. 2.1 indicates the initial configuration Ω_0 of a body and the current configuration denoted by Ω.

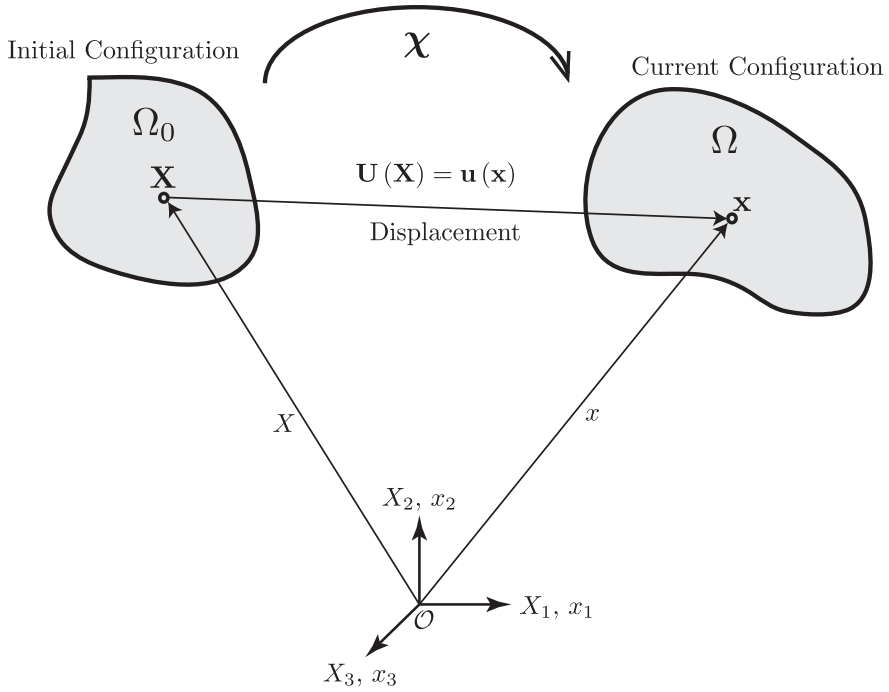

Figure 2.1: The motion of a continuum body from the initial configuration Ω_0 to the current configuration Ω

2.1 Mesh descriptions

There are three mesh descriptions: Lagrangian, Eulerian and arbitrary Lagrangian Eulerian descriptions [1]. One of the notable differences between Lagrangian and Eulerian meshes are the behaviour of the nodes [15, 22, 95]. Fig. 2.2 represents the movement of node and material points of both Lagrangian and Eulerian descriptions. As shown in Fig. 2.2, nodes and material points (meshes and materials) deform in Lagrangian formulation, whereas nodes are fixed and materials flow into elements in Eulerian formulation. Lagrangian formulations have two

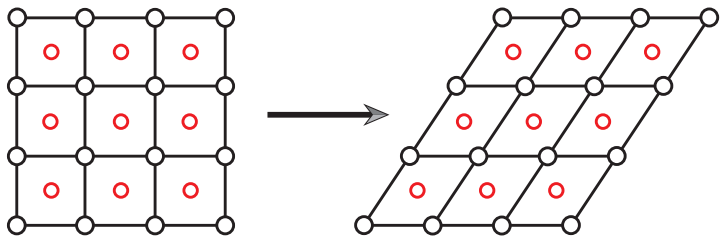

Node Point

Material Point

(a) Lagrangian Description

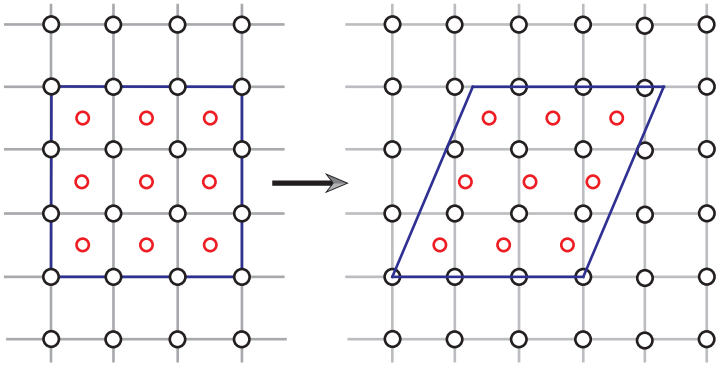

Node Point

Material Point

(b) Eulerian Description

Figure 2.2: Lagrangian and Eulerian descriptions

[1] Euler (1762) introduced Lagrangian coordinates (the material coordinates) and d'Alembert introduced Eulerian coordinates (the spatial coordinates) in 1752 from References [95, 151].

possible descriptions, one is the total Lagrangian formulation. The second is the updated Lagrangian formulation. Variables in the total Lagrangian formulation are described in the initial configuration, while they are described in the current configuration in the updated Lagrangian formulation [15]. Additionally different stress and deformation measures are used in both formulations: a total measure of strain and the second Piola-Kirchhoff (PK2) stress for the total Lagrangian formulation and a rate measure of strain and Cauchy stress for updated Lagrangian formulation. However, Green Lagrange strain can also be used in both total and updated Lagrangian formulations. The momentum equation and its weak form can be simply evaluated using the nominal stress rather than using the PK2 stress. Since PK2 stress is symmetric, the constitutive equations can be easily obtained. Fig. 2.3 illustrates a 2D polygonal element in the initial (reference

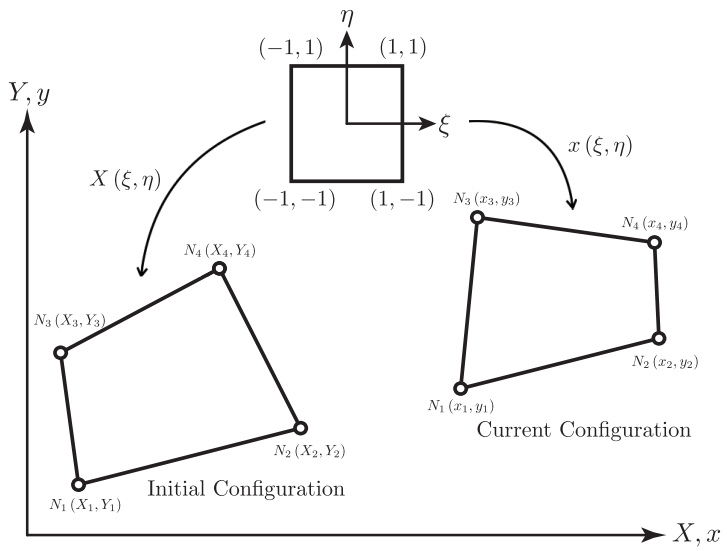

Figure 2.3: Mapping to initial and current configurations in a Lagrangian mesh description

or undeformed) and current (deformed) configuration. The 2D parent domain (ξ, η) maps onto the initial (X, Y) and current (x, y) configurations. Current coordinates (x, y) are defined by initial coordinates (X, Y) with displacement, $(x, y) = (X, Y) + (u_X, u_Y)$.

2.1.1 Lagrangian mesh

The Lagrangian (material) coordinates of the nodes coincide with material points [9, 10, 15, 62].

- The Lagrangian coordinates of nodes moves with the material, and material points are time invariant;
- The material does not pass between elements;
- Meshes can be severely distorted because the meshes deform with the material;
- Boundary nodes remain on the boundary. Hence the implementation of boundary condition is straightforward;
- Lagrangian coordinates are in general well-suited to solid mechanics.

2.1.2 Eulerian mesh

The Eulerian coordinates of the nodes are coincident with spatial points [9, 10, 15, 96].

- The Eulerian coordinates of the nodes are fixed;
- The material flows through the element;
- Since elements are fixed in space, mesh distortion never occurs;
- Boundary nodes and the boundary of material domain are not coincident, therefore a treatment of moving boundary conditions is required;
- Eulerian coordinates are well-suited for fluid mechanics.

2.1.3 Arbitrary Lagrangian-Eulerian approach

A Lagrangian approach is ill-suited some cases in fluid mechanics and the accuracy suffers due to severely distorted elements. Eulerian methods, on the other hand, do not cause distortion because elements are fixed in space. However, the treatment of moving boundaries, interfaces and constitutive equations is complicated in Eulerian frame work. Arbitrary Lagrangian-Eulerian (ALE) formulation takes the advantages of Lagrangian and Eulerian approaches but avoids their shortcomings [3, 50, 70, 72, 145, 153]. This technique is often used in engineering, e.g. metal forming [7, 58, 153], metal cutting [57, 125], fluid-structure interface [138, 144, 162], free surface flow problems [27, 146] and free boundary problems [53, 158].

2.2 Hyperelastic materials

Hyperelastic (or Green elastic) materials are elastic materials. The stress is defined by the current strain and is independent of strain. The stress-strain curve is derived from a strain energy function (or stored energy function) $\mathcal{W}$ per undeformed unit volume and fully reversible. Since the deformation of hyperelastic materials is not directly proportional to the load, their behaviour is non-linear. In [15, 22], compressible and incompressible hyperelastic materials, neo-Hookean materials in particular, are expressed.

The second Piola-Kirchhoff (PK2) stress is obtained by a differentiation of the stored energy function with respect to the Green-Lagrange strain

$$\mathbf{S} = 2\frac{\partial \mathcal{W}(\mathbf{C})}{\partial \mathbf{C}} = \frac{\partial \mathcal{W}(\mathbf{E})}{\partial \mathbf{E}} \tag{2.1}$$

where $\mathbf{S}$ is the PK2 stress, $\mathbf{E}$ is the Green-Lagrange strain defined as $\mathbf{E} = 1/2\left(\mathbf{F}^{\mathrm{T}}\mathbf{F} - \mathbf{I}\right)$ in terms of the deformation gradient $\mathbf{F}$. $\mathbf{C}$ is the right Cauchy-Green strain tensor $\mathbf{C} = \mathbf{F}^{\mathrm{T}}\mathbf{F}$. From Eq. (2.1), the Cauchy (true) stress is

determined as

$$\boldsymbol{\sigma} = -p\mathbf{I} + 2\frac{\partial \mathcal{W}(\mathbf{E})}{\partial I_1}\mathbf{C} - 2\frac{\partial \mathcal{W}(\mathbf{E})}{\partial I_2}\mathbf{C}^{-1} \tag{2.2}$$

where I_1, I_2 and I_3 are the principal invariants of $\mathbf{C}$. If the second-order tensor is symmetric, the principal invariants of the right Cauchy-Green strain can be expressed as

$$\begin{aligned} I_1(\mathbf{C}) &= \mathrm{tr}\mathbf{C} = \lambda_1 + \lambda_2 + \lambda_3 \\ I_2(\mathbf{C}) &= \frac{1}{2}\left\{(\mathrm{tr}\mathbf{C})^2 - \mathrm{tr}\left(\mathbf{C}^2\right)\right\} = \mathrm{tr}(\mathrm{cof}\mathbf{C}) = \lambda_1\lambda_2 + \lambda_2\lambda_3 + \lambda_3\lambda_1 \\ I_3(\mathbf{C}) &= \det\mathbf{C} = (\det\mathbf{F})^2 = \lambda_1\lambda_2\lambda_3 \end{aligned} \tag{2.3}$$

where λ_1, λ_2 and λ_3 are the eigenvalue of the right Cauchy-Green tensor $\mathbf{C}$. The average properties of rubber and other materials, human bone, steel, glass, concrete, plastic and human tissues, are represented in Table 2.1 from [137] and [143][2].

Table 2.1: Average material properties of rubber and other materials

Material	Young's modulus (MPa)	Poisson's ratio	Shear modulus (MPa)	Bulk modulus (MPa)
Rubber (typical range)	0.76∼7.60	0.5	0.35∼1.38	3,000∼3,500
Human Bone	10,021	0.3	3,854	8,350
Mild Steel	207,348	0.29∼0.3	79,483	158,967
Glass	55,292	0.25	22,117	36,631
Concrete	27,646	0.18	11,714	14,398
Polyethylene	138∼380	0.25	55∼152	89∼255
Stomach	0.1349∼0.2399	0.4995∼0.49991	0.008∼0.045	480
Liver	0.1109∼1.0195	0.49939∼0.49999	0.0037∼0.34	280
Heart	0.1799∼0.4439	0.4997∼0.4999	0.06∼0.148	250∼490
Lung	0.0299∼0.1619	0.4998∼0.4999	0.01∼0.054	150

[2]This paper is a technical paper written by MSC Software Corporation (http://www.mscsoftware.com/application/nonlinear-analysis).

There are numerous hyperelastic materials, e.g. St. Venant-Kirchhoff material, neo-Hookean materials, Mooney-Rivlin materials, Ogden materials, the Yeoh model as well as Blatz-Ko model. St. Venant-Kirchhoff material is the simplest hyperelastic material [79]. The behaviour is large displacement but small strains. In the linear elastic law, the stress is replaced by the second Piola-Kirchhoff (PK2) stress and the linear strain is replaced by the Green-Lagrange strain. Mooney-Rivlin materials are widely used for the large strain non-linear incompressible materials, particularly rubbers [98, 135, 136]. These materials are incompressible and initially isotropic. Ogden material was introduced by Ogden in 1972 [121] to describe highly elastic materials such as rubbers or tissues. Ogden materials are isotropic, incompressible and their strain rate are independent [122, 124]. The Yeoh model was introduced to characterise the incompressible hyperelastic rubber-like materials [140, 160] and Blatz-Ko material was introduced for the compressible isotropic non-linearly elastic solids (foam-rubber material) [16, 17, 63].

In this work, neo-Hookean materials are considered. The neo-Hookean materials are the extension of Hooke's raw (isotropic linear law) and are normally used for large deformation, e.g. rubber-like material [142, 154].

The stored energy function for a compressible neo-Hookean model [15] is

$$\mathcal{W}(\mathbf{C}) = \frac{1}{2}\lambda_0 (\ln J)^2 - \mu_0 \ln J + \frac{1}{2}\mu_0 (\mathrm{tr}\mathbf{C} - 3) \tag{2.4}$$

where the Jacobian is $J = \det \mathbf{F}$.

By Eq. (2.1), the PK2 stress is given as

$$\mathbf{S} = \lambda_0 \ln J \mathbf{C}^{-1} + \mu_0 \left(\mathbf{I} - \mathbf{C}^{-1}\right) \tag{2.5}$$

and the fourth-order elastic tensors are

$$\mathbb{C}_{ijkl} = \lambda C^{-1}_{ij} C^{-1}_{kl} + \mu \left(C^{-1}_{ik} C^{-1}_{jl} C^{-1}_{jl} + C^{-1}_{il} C^{-1}_{kj} \right) \tag{2.6}$$

where $\lambda = \lambda_0$ and $\mu = \mu_0 - \lambda \ln J$. Note that μ_0 is the shear modulus and Lamé's first parameter $\lambda_0 = \kappa - 2/3\mu_0$ where the bulk modulus is κ.

2.3 Finite element method for linear elasticity

The principles of linear elasticity are reviewed and summarised in this section. When either an external force or an internal force is applied to a continuum body, all points of the body are influenced by these forces. The external force leads a change of size and/or shape of the medium and the internal force resists this deformation. Then when the external force is removed, the medium "tries" to return to its initial shape and/or size. If the medium returns to its undeformed shape perfectly, this medium is called *elastic*. A material is called linear elastic if the relationship between the applied forces and the resulting displacements or that of the applied displacements and resulting internal forces is linear.

Linear elasticity is a simplification of finite elasticity. In linear elastic, there exists a linear relation between the components of strains and stresses. For most materials, this is true when strains are small (less than 10%). In linear elasticity, strain does not depend on the rate or history of loading but it depends on the stress.

2.3.1 Formulation of linear elastic 2D problem

For an isotropic linear elastic solid, the equilibrium equations state that the divergence of the stress equals the body forces:

$$-\nabla\boldsymbol{\sigma} = \mathbf{f} \tag{2.7}$$

The variational form of Eq. (2.7) can be expressed as

$$\int_{\Omega} \boldsymbol{\sigma} \cdot \nabla\mathbf{v} \mathrm{d}\Omega = \int_{\Omega} \mathbf{f} \cdot \mathbf{v} \mathrm{d}\Omega + \int_{\Gamma_N} \mathbf{g} \cdot \mathbf{v} \mathrm{d}\Gamma \tag{2.8}$$

where $\mathbf{f}$ is the vector of body forces, $\mathbf{g} = \boldsymbol{\sigma} \cdot \mathbf{n}$ is the prescribed traction vector on natural boundary Γ_N and $\mathbf{v}$ is a test function belonging to the space of admissible displacement field vanishing on the Dirichlet Boundary.

The stress tensor $\boldsymbol{\sigma}$ is

$$\boldsymbol{\sigma} = 2\mu\boldsymbol{\varepsilon} + \lambda \mathrm{tr}\left(\boldsymbol{\varepsilon}\right)\mathbf{I} \tag{2.9}$$

where μ is the shear modulus and λ is Lamé's parameter, which can be expressed in terms of Young's modulus E and Poisson's ratio ν as follows

$$\mu = \frac{E}{2\left(1+\nu\right)}, \quad \lambda = \frac{E\nu}{\left(1+\nu\right)\left(1-2\nu\right)} \tag{2.10}$$

and the infinitesimal strain tensor $\boldsymbol{\varepsilon}$ is

$$\boldsymbol{\varepsilon} = \left\{\varepsilon_{ij}\right\}, \quad \varepsilon_{ij} = \frac{1}{2}\left(\frac{\partial u_i}{\partial X_j} + \frac{\partial u_j}{\partial X_i}\right) \tag{2.11}$$

or equivalently

$$\boldsymbol{\varepsilon} = \frac{1}{2}\left(\nabla\mathbf{u} + \nabla\mathbf{u}^{\mathrm{T}}\right) \tag{2.12}$$

In Voigt notation, the stress tensor can be expressed as follows

$$\begin{Bmatrix} \sigma_{11} \\ \sigma_{22} \\ \sigma_{12} \end{Bmatrix} = \mathbb{C} \begin{Bmatrix} \varepsilon_{11} \\ \varepsilon_{22} \\ 2\varepsilon_{12} \end{Bmatrix} \tag{2.13}$$

where $\mathbb{C}$ is the elasticity tensor

$$\mathbb{C} = \begin{bmatrix} 2\mu + \lambda & \lambda & 0 \\ \lambda & 2\mu + \lambda & 0 \\ 0 & 0 & 2\mu \end{bmatrix} \tag{2.14}$$

The discrete equation of finite element method (FEM) from the Galerkin weak form is to find the finite element relation $\mathbf{u}^{\mathrm{h}}$ in the discrete space of admissible solutions satisfying Dirichlet BCs such that for all test functions $\mathbf{v}^{\mathrm{h}}$ with set of admissible displacements with homogeneous Dirichlet BCs

$$\int_{\Omega} \mathbb{C}\boldsymbol{\varepsilon}\left(\mathbf{u}^{\mathrm{h}}\right) \cdot \boldsymbol{\varepsilon}\left(\mathbf{v}^{\mathrm{h}}\right) \mathrm{d}\Omega = \int_{\Omega} \mathbf{f} \cdot \mathbf{v}^{\mathrm{h}} \mathrm{d}\Omega + \int_{\Gamma_N} \mathbf{g} \cdot \mathbf{v}^{\mathrm{h}} \mathrm{d}\Gamma \tag{2.15}$$

This is written, in matrix form

$$\mathbf{K}\mathbf{u}^{\mathrm{h}} = \mathbf{b} \tag{2.16}$$

where $\mathbf{K}$ is the stiffness matrix and $\mathbf{b}$ is the element force vector:

$$\begin{aligned} K_{IJ} &= \int_{\Omega} \mathbb{C}\boldsymbol{\varepsilon}\left(\Psi_I\right) \cdot \boldsymbol{\varepsilon}\left(\Psi_J\right) \mathrm{d}\Omega \\ b_I &= \int_{\Omega} f\Psi_I \mathrm{d}\Omega + \int_{\Gamma_N} g\Psi_I \mathrm{d}\Gamma \end{aligned} \tag{2.17}$$

where Ψ is the shape functions.

2.4 Summary

This chapter recalled the fundamental background necessary to understand the forthcoming developments.

3 Smoothed finite element method

3.1 Review of gradient smoothing approach for finite elements

Gradient (strain) smoothing originated in the meshless literature from a stabilised conforming nodal integration (SCNI) introduced by Chen et al. [33]. Direct nodal integration faces numerical instability. SCNI improves accuracy and stability by moving the evaluation of the shape function derivatives from the nodes where they vanish to the boundary of smoothing domains, using the divergence theorem. Yoo et al. [161] extended SCNI to the natural element method and solved nearly-incompressible large deformation problems without any modification. Liu et al. [82] employed strain smoothing in finite element method (smoothed finite element method (S-FEM)), converting domain integration to boundary integration also through the divergence theorem. The basic idea of S-FEM is to divide the computational domains into sub-domains where strains are smoothed. The gradients (strains) are constant over the smoothing domains but they are discontinuous across the boundaries of smoothing domains. Sub-domains are usually constructed using the topology provided by the mesh. Depending on this construction, various solution behaviours are observed, offering the use of a spectrum of methods with

particular properties [25, 84, 85].

3.1.1 Main features of S-FEM

The smoothed finite element method (S-FEM) was introduced to enable the use of simplex meshes, which are relatively simple to generate, even for complex geometries, whilst avoiding the major drawbacks of such low order elements. The methods that ensued have a range of properties, depending on the choice of the background cells. Without giving details at this point, which will be revisited later the salient features of S-FEM are as follows:

- ability to deal with almost arbitrary element distortion (because the suppression of the Jacobian transformation from parent to physical coordinates: integration is performed in physical space);
- ability to use elements of arbitrary shape, including polyhedral elements;
- relative insensitivity to locking (volumetric and shear).

When used with bilinear elements (quadrilaterals or hexahedral elements), the method provides a range of behaviours ranging from a quasi-equilibrium element, or, equivalently an under-integrated 4-node quadrilateral (for one single subcell) to a displacement-based finite element (in the limit where the number of subcells reaches infinity).

But S-FEM also has drawbacks

- the bandwidth is larger, which increases memory requirements and computational time. However, for most problems addressed to date, for the same computational time, accuracy is usually superior for S-FEM [25];

- the use of higher order and non-polynomial functions in the approximation space is not yet well-understood in the context of strain smoothing.

3.2 Different smoothed finite elements

Four different types of S-FEM were developed [84], depending on how smoothing domains are built: cell-based S-FEM (CS-FEM), edge-based S-FEM (ES-FEM), node-based S-FEM (NS-FEM) and face-based S-FEM (FS-FEM). Each S-FEM has different properties as follows:

- **Volumetric locking** NS-FEM can handle effectively nearly-incompressible materials where Poisson's ratio $\nu \to 0.5$ [84, 87], while ES-FEM does not completely suppress volumetric locking. But combining NS- and ES-FEM: *the selective smoothing ES/NS-FEM* overcomes the locking problem [84]. In the case of CS-FEM, volumetric locking can be avoided by selective integration [101, 113]. Each method performed well with Poisson's ratio up to $\nu = 0.4999999$.

- **Upper and lower bound properties** For most problems, NS-FEM gives an upper bound solution and FEM obtains a lower bound solution. While, in the case of a problem with no external forces (displacement-based) but non-zero prescribed Dirichlet boundary conditions, NS-FEM and FEM provide respectively lower and upper bounds for the energy [84, 89, 104].

- **Static and Dynamic Analyses** ES-FEM gives accurate and stable results when solving either static or dynamic problems [86]. In contrast, although NS-FEM is spatially stable, it is temporally unstable. Therefore, to solve dynamic problems, NS-FEM requires stabilisation techniques [163, 164]. CS-FEM can also be extended to solve dynamic problems [43].

- **Other features** In NS-FEM, the accuracy of the displacement norm is

comparable to that of the standard FEM using the same mesh, whereas the accuracy of stress solutions in the energy norm is superior to that of FEM [84]. In CS-FEM, four smoothing domains can be used for isochoric and one smoothing domain can be used for volumetric components, respectively. In terms of computational time, in general, S-FEM is more expensive than conventional FEM for the same set of nodes [84].

3.2.1 Edge-based smoothed finite element method

The smoothing domain Ω_k in ES-FEM is constructed around a target edge k which is the boundary segment of each element sharing edge k (as shown in Fig. 3.1). In general, S-FEM is more accurate than FEM for the same computational expense. The smoothed strain-displacement matrix $\tilde{\mathbf{B}}_I$ for node I is computed

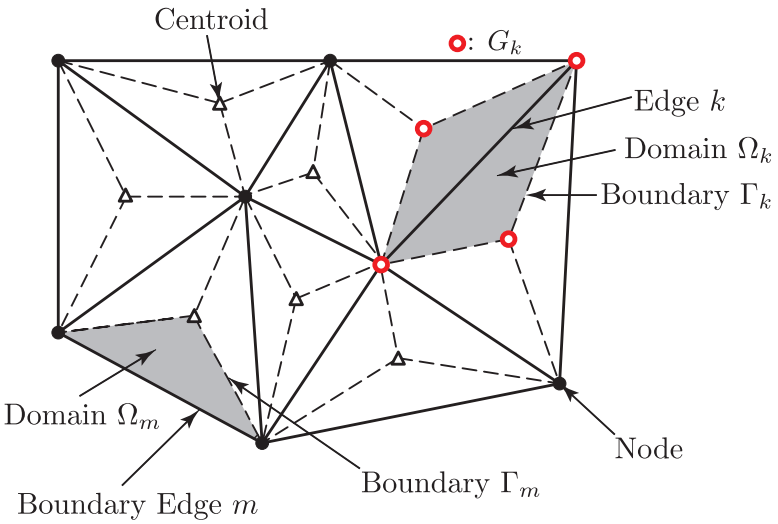

Figure 3.1: Smoothing domain associated with edge k for T3 ES-FEM

with shape functions evaluated at Gauss points on the mid-point of boundary Γ_k of the smoothing domain Ω_k and the outward normal vector (See Fig. 3.2). A number of Gauss point is one on each segment of the smoothing domain and therefore four Gauss points are used in the whole smoothing domain Ω_k.

The smoothed strain-displacement matrix $\tilde{\mathbf{B}}_I$ is defined as

$$\tilde{\mathbf{B}}_I(\mathbf{x}) = \frac{1}{A_k}\int_{\Gamma_k} \mathbf{n}(\mathbf{x})\,\Psi_I \mathrm{d}\Gamma \tag{3.1}$$

where A_k is the area of the smoothing domain, $\mathbf{n}$ is the outward normal vector and Ψ is the shape functions. In particular, when a linear T3 element is used, the following form of smoothed strain-displacement matrix can be used

$$\tilde{\mathbf{B}}_I(\mathbf{x}) = \frac{1}{A_k}\sum_{p=1}^{N_p^e}\frac{1}{3}A_p^e\mathbf{B}_p^e \tag{3.2}$$

where N_p^e is the number of elements of the smoothing domain associated with edge k, A_p^e is the area of element sharing edge k and $\mathbf{B}_p^e$ is the standard compatible strain-displacement matrix of a T3 element in the standard FEM. The smoothed

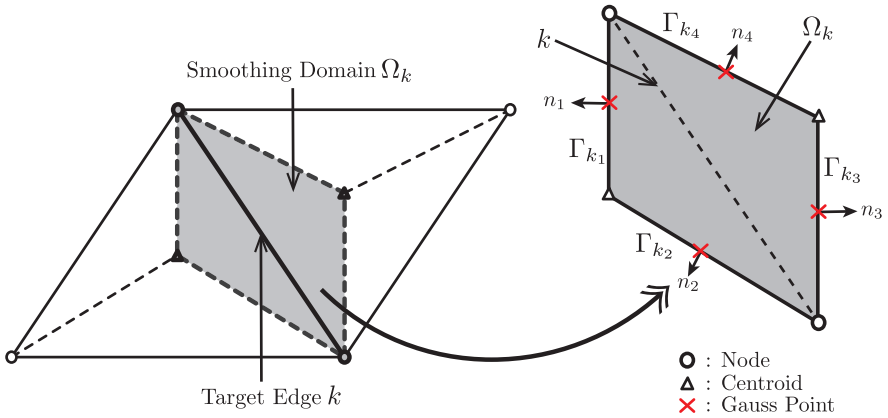

Figure 3.2: Gauss point and outward normal evaluated on the boundary of smoothing domain associated with target edge k in ES-FEM with linear T3 element

stiffness matrix is (shown in Fig. 3.3)

$$\tilde{\mathbf{K}} = \sum_{k=1}^{N_e}\tilde{\mathbf{B}}_k^{\mathrm{T}}(\mathrm{x})\,\mathbb{C}\tilde{\mathbf{B}}_k(\mathbf{x})\,A_k \tag{3.3}$$

where N_e is the number of edges, $\mathbb{C}$ is the elasticity tensor and the area of smoothing domain $A_k = \int_{\Omega_k^s}\mathrm{d}\Omega$. Note that the central point of each T3 element,

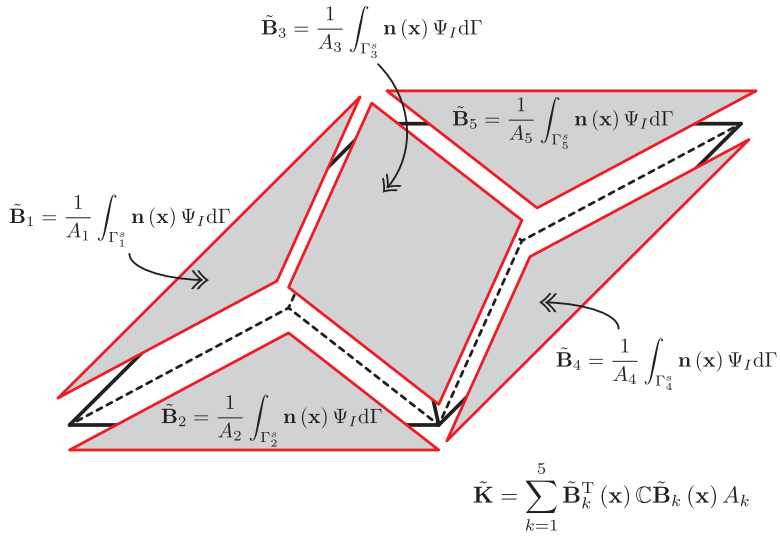

Figure 3.3: Construction of the stiffness matrix in ES-FEM: Two T3 elements have five edges and the smoothed strain-displacement matrices are built in each smoothing domain

associated with edge-based strain smoothing, has no additional degrees of freedom (DOF) and no additional field variables.

3.2.2 Node-based smoothed finite element method

In node-based smoothing, similarly to ES-FEM, the problem domain Ω is split into smoothing domains created by grouping sub-domains of each element sharing target node k (shown in Fig. 3.4). Sub-domains for NS-FEM are created using the centroid of the finite elements and the mid-point of each edges.

As in ES-FEM, numerical integration for node-based strain smoothing is done on the boundary of the smoothing domain (see Fig. 3.5). The smoothed strain-displacement matrix in NS-FEM is given as

$$\tilde{\mathbf{B}}_I(\mathbf{x}) = \frac{1}{A_k}\int_{\Gamma_k} \mathbf{n}(\mathbf{x})\,\Psi_I \mathrm{d}\Gamma \tag{3.4}$$

where A_k is the area of the smoothing domain, $\mathbf{n}$ is the outward normal vector and

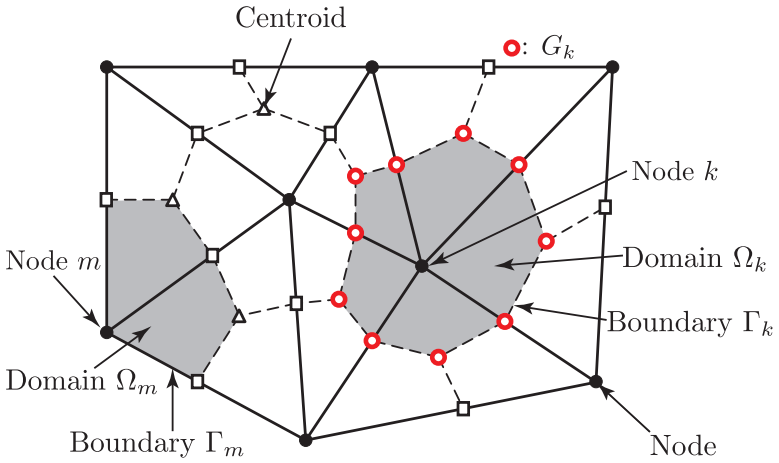

Figure 3.4: Smoothing domain associated with node k for NS-FEM with T3 element

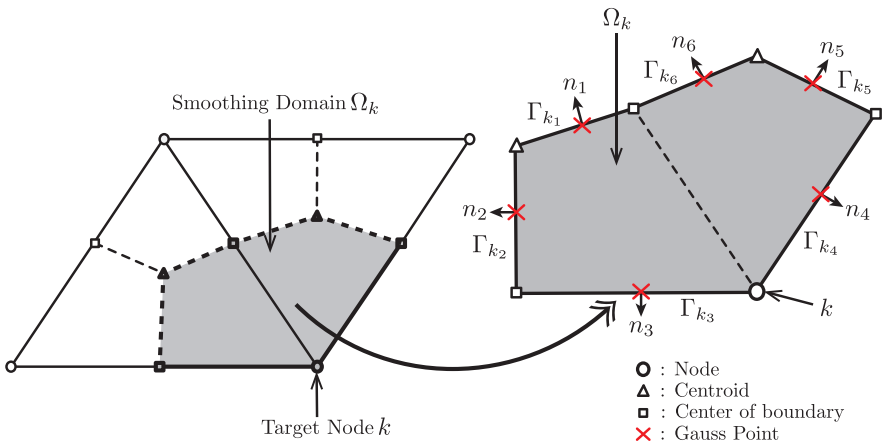

Figure 3.5: Gauss point and outward normal evaluated on the boundary of smoothing domain associated with target edge k in NS-FEM with linear T3 element

Ψ is the shape functions. Similarly to ES-FEM, the smoothed strain-displacement matrix can be also defined as

$$\tilde{\mathbf{B}}_I(\mathbf{x}) = \frac{1}{A_k} \sum_{p=1}^{N_p^e} \frac{1}{3} A_p^e \mathbf{B}_p^e \tag{3.5}$$

where N_p^e is the number of elements associated with node k, A_p^e is the area of element sharing node k and $\mathbf{B}_p^e$ is the standard compatible strain-displacement matrix of a linear T3 element in the FEM. As shown in Fig. 3.6, the smoothed

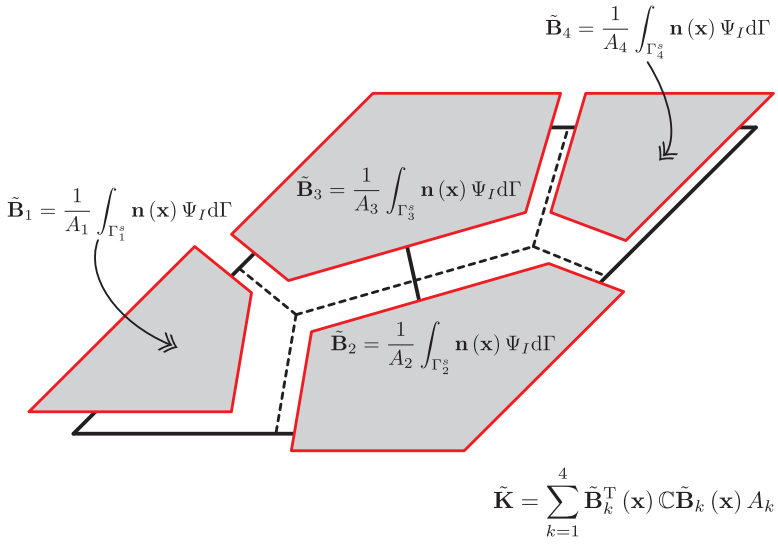

Figure 3.6: Construction of the stiffness matrix in NS-FEM: Two T3 elements have four nodes and the smoothed strain-displacement matrices are built in each smoothing domain

stiffness matrix is

$$\tilde{\mathbf{K}} = \sum_{k=1}^{N_n} \tilde{\mathbf{B}}_k^{\mathrm{T}} \mathbb{C} \tilde{\mathbf{B}}_k A_k \tag{3.6}$$

where N_n is the number of nodes, $\tilde{\mathbf{B}}_k$ is the smoothed strain-displacement matrix, $\mathbb{C}$ is the elasticity tensor and A_k is the area of the smoothing domain.

3.2.3 Face-based smoothed finite element method

Strain smoothing was extended to 3D problems, e.g. the *face-based smoothed finite element method (FS-FEM)*. The idea behind FS-FEM is shown in Fig. 3.7. A T4 element is split into four sub-domains by a standard Delaunay triangulation algorithm and smoothing domain is constructed using target face k of each face (surface) of sub-domains.

In Reference [112], an integration scheme for 3D CS-FEM with hexahedral element is explained. Similar to 3D CS-FEM, Gauss points for FS-FEM are located in

the middle of each face of smoothing polyhedra, evaluating outward normals and shape functions. Fig. 3.8 depicts positions of Gauss points for T4 FS-FEM. The

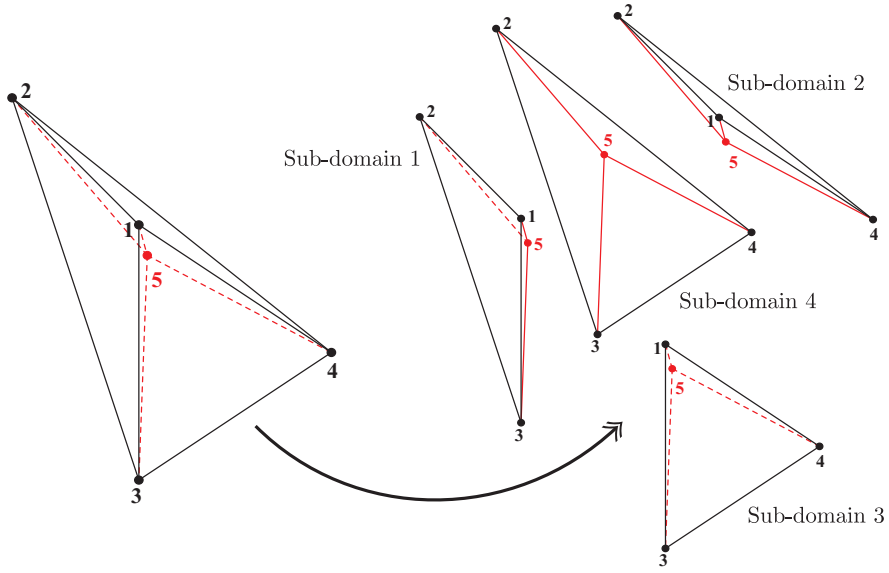

(a) Sub-domains for tetrahedral element

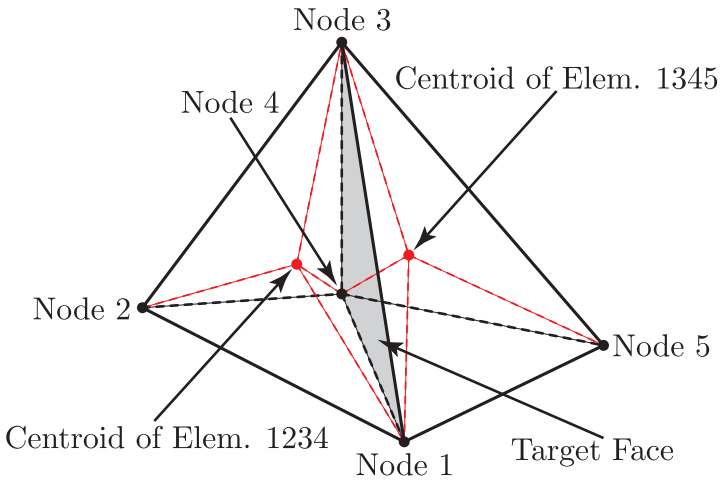

(b) Smoothing domain associated to target face

Figure 3.7: Smoothing domain of face-based S-FEM with tetrahedral elements: (a) four sub-domains for tetrahedral element and (b) smoothing domain associated to target face

smoothed strain-displacement matrix for face-based smoothing is represented as

$$\tilde{\mathbf{B}}\left(\mathbf{x}\right) = \frac{1}{V_k}\int_{\Omega_k^s} \mathbf{B}_I\left(\mathbf{x}\right) \mathrm{d}\Omega = \frac{1}{V_k}\sum_{n=1}^{N_p^e} \frac{1}{4} V_p^e \mathbf{B}_p^e \tag{3.7}$$

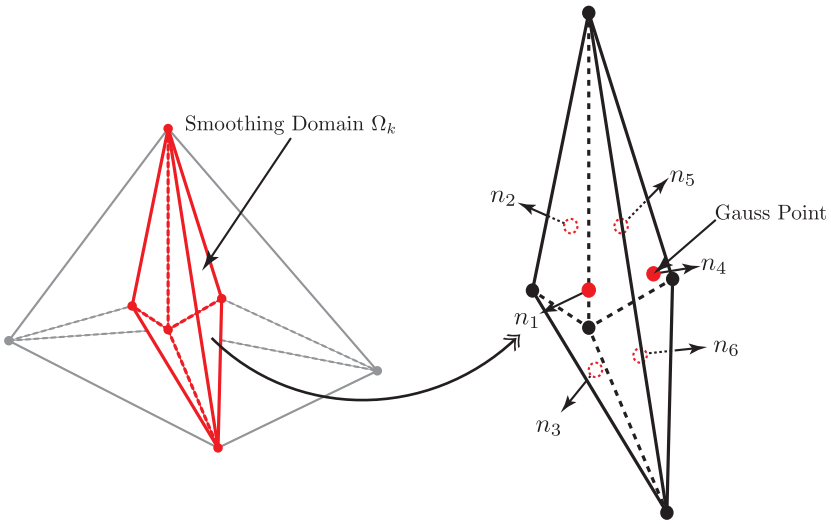

Figure 3.8: Face-based Smoothing: Gauss Points where shape functions and outward normal vectors are evaluated

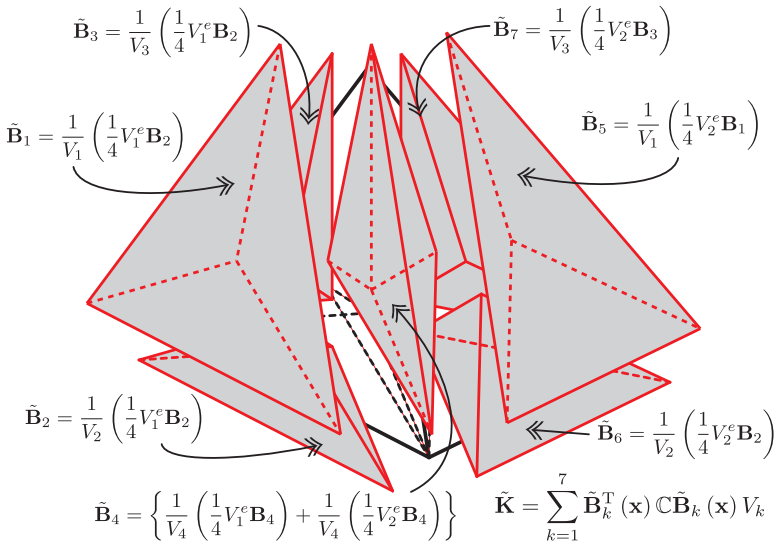

Figure 3.9: Construction of the stiffness matrix in FS-FEM: Two T4 elements have seven faces and the smoothed strain-displacement matrices are built in each smoothing domain

where V_k is the volume of the smoothing domains, N_p^e is the number of elements associated with target face k, V_p^e is the volume of the element sharing target face and $\mathbf{B}_p^e$ is the T4 strain-displacement matrix in the FEM. The smoothed stiffness

matrix of FS-FEM is built as shown in Fig. 3.9

$$\tilde{\mathbf{K}} = \sum_{k=1}^{N_f} \tilde{\mathbf{B}}_k^{\mathrm{T}} \mathbb{C} \tilde{\mathbf{B}}_k V_k \tag{3.8}$$

where N_f is the number of faces, $\tilde{\mathbf{B}}_k$ is the smoothed strain-displacement matrix, $\mathbb{C}$ is the elasticity tensor and V_k is the volume of smoothing domain.

3.3 Smoothed finite element method in linear elasticity

Now that the key concepts behind the evaluation of the stiffness matrix in S-FEM have been given, the construction of S-FEM is approached more primally. The basics of S-FEM is presented in the context of small strain elasticity. The infinitesimal strain tensor $\varepsilon_{ij}^{\mathrm{h}}$ for linear elasticity is given as

$$\varepsilon_{ij}^{\mathrm{h}} = \frac{1}{2}\left(\frac{\partial u_i^{\mathrm{h}}}{\partial X_j} + \frac{\partial u_j^{\mathrm{h}}}{\partial X_i}\right) \tag{3.9}$$

where $\mathbf{u}$ is the displacement field and $\mathbf{X}$ is the initial (or material) configuration, which for small deformation coincides with the current configuration.

The infinitesimal strain tensor is *smoothed* over the smoothing domain Ω_k^s by computing the weighted average of $\varepsilon_{ij}^{\mathrm{h}}$ as

$$\forall \mathbf{x} \in \Omega_k^s, \quad \tilde{\boldsymbol{\varepsilon}}^{\mathrm{h}}(\mathbf{x}_k) = \int_{\Omega_k^s} \boldsymbol{\varepsilon}^{\mathrm{h}}(\mathbf{x})\, \Phi(\mathbf{x})\, \mathrm{d}\Omega \tag{3.10}$$

where a point $\mathbf{x}_k$ (shown in Fig. 3.10) is located in a smoothing domain Ω_k^s. Properties of the weight function Φ are

$$\int_{\Omega_k^s} \Phi(\mathbf{x})\, \mathrm{d}\Omega = 1, \quad \Phi > 0 \tag{3.11}$$

$$\Phi(\mathbf{x}) = \begin{cases} 1/A_k & \mathbf{x} \in \Omega_k^s \\ 0 & \mathbf{x} \notin \Omega_k^s \end{cases} \tag{3.12}$$

where A_k is the area of smoothing domain Ω_k^s. Applying the divergence theorem,

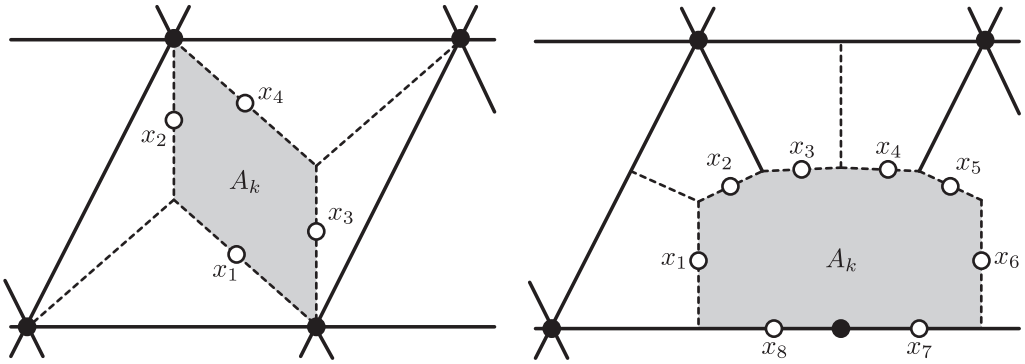

(a) ES-FEM (b) NS-FEM

Figure 3.10: Description of the smoothing domains and integration points $\mathbf{x}_k$: the considered smoothing domain is denoted by shade and dashed line, black-filled circles are nodes and white-filled circles are integration points $\mathbf{x}_k$

the smoothed strain can be obtained as follows

$$\tilde{\boldsymbol{\varepsilon}}^{\mathrm{h}}(\mathbf{x}_k) = \frac{1}{A_k}\int_{\Omega_k^s} \boldsymbol{\varepsilon}(\mathbf{x})\,\mathrm{d}\Omega = \frac{1}{A_k}\int_{\Gamma_k^s} \mathbf{n}(\mathbf{x})\,\mathbf{u}^{\mathrm{h}}(\mathbf{x})\,\mathrm{d}\Gamma \tag{3.13}$$

where Γ_k^s is the boundary of the smoothing domain Ω_k^s and $\mathbf{n}(\mathbf{x})$ is the outward normal on boundary Γ_k^s. For 2D the outward normal vector matrix is

$$\mathbf{n}(\mathbf{x}) = \begin{bmatrix} n_1 & 0 \\ 0 & n_2 \\ n_2 & n_1 \end{bmatrix} \tag{3.14}$$

The discrete trial and test functions are, in the FEM, using Lagrange shape

functions Ψ_I at the node I of a simplex mesh[1]

$$\mathbf{u}^{\mathrm{h}}(\mathbf{x}) = \sum_{I=1}^{N} u_I \Psi_I(\mathbf{x}), \quad \mathbf{v}^{\mathrm{h}}(\mathbf{x}) = \sum_{J=1}^{N} v_J \Psi_J(\mathbf{x}) \tag{3.15}$$

If the strain in each sub-domain is constant (as for T3 or T4), the smoothed strain is written

$$\tilde{\boldsymbol{\varepsilon}}^{\mathrm{h}}(\mathbf{x}_k) = \frac{1}{A_k} \sum_{q=1}^{N_{SD}} A_{k,q} \boldsymbol{\varepsilon}(\mathbf{x})_q \tag{3.16}$$

where $\boldsymbol{\varepsilon}(\mathbf{x})$ is the constant compatible strain of the qth sub-domain of smoothing domain Ω_k^s, $A_{k,q}$ is the smoothing domain area of the qth sub-domain and N_{SD} is the number of sub-domains of smoothing domain Ω_k^s. Fig. 3.11 illustrates

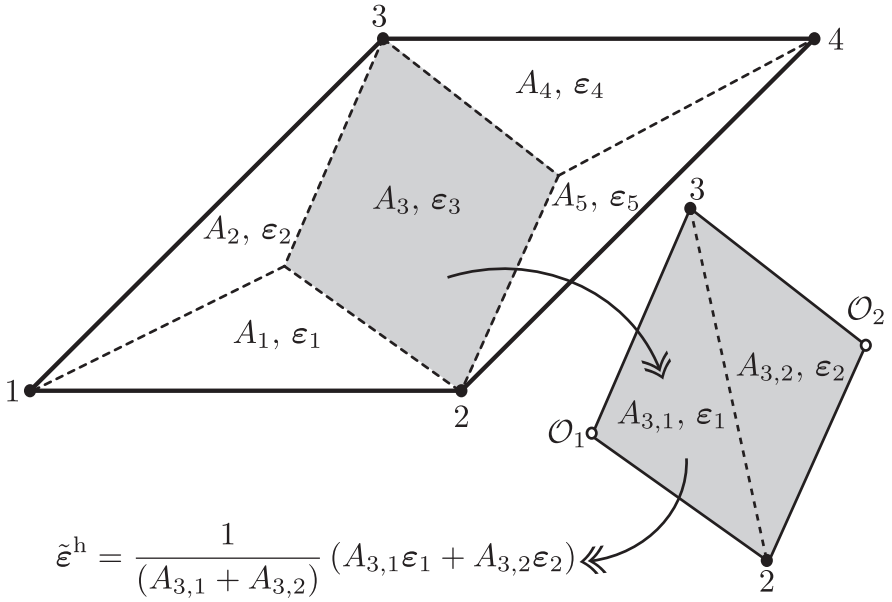

Figure 3.11: Construction of the smoothed strain in ES-FEM

Eq. (3.16) in the edge-wise smoothing approach. Note that when target edge k is chosen to an inner edge in the problem domain, the smoothing domain is assembled by two sub-domains in ES-FEM. In this case thus $N_{SD} = 2$, while when target edge k is the boundary edge, then $N_{SD} = 1$.

[1] In this work we consider only linear shape functions, as linear elements are the most suitable for strain smoothing according to [24, 25].

The smoothed strain-displacement matrix. The smoothed strain Eq. (3.13) can be re-written in terms of the nodal displacements as follows

$$\tilde{\boldsymbol{\varepsilon}}\left(\mathbf{x}_k\right) = \sum_{I \in G_k} \tilde{\mathbf{B}}_I\left(\mathbf{x}\right) \mathbf{u}_I^{\mathrm{h}} \tag{3.17}$$

where G_k is a set of nodes shown in Figs. 3.1 and 3.4. From the smoothed strain, the smoothed strain-displacement matrix for 2D is obtained to evaluate the smoothed stiffness matrix given as

$$\tilde{\mathbf{B}}_I\left(\mathbf{x}\right) = \frac{1}{A_k} \int_{\Gamma_k^s} \mathbf{n}\left(\mathbf{x}\right) \Psi_I \mathrm{d}\Gamma = \begin{bmatrix} \tilde{B}_{I1} & 0 \\ 0 & \tilde{B}_{I2} \\ \tilde{B}_{I2} & \tilde{B}_{I1} \end{bmatrix} \tag{3.18}$$

where $\tilde{B}_{Ii}$ can be obtained as

$$\tilde{B}_{Ii} = \frac{1}{A_k} \int_{\Gamma_k^s} \psi_I\left(\mathbf{x}\right) n_i\left(\mathbf{x}\right) \mathrm{d}\Gamma \tag{3.19}$$

where Ψ_I is the shape functions. Note that Eqs. (3.18) and (3.19) are visualized in Figs. 3.2 and 3.5.

From the definition of the smoothed strain field Eq. (3.10), the relation between the smoothed strain-displacement $\tilde{\mathbf{B}}_I\left(\mathbf{x}\right)$ and a standard compatible strain-displacement $\mathbf{B}_I\left(\mathbf{x}\right)$ in FEM is

$$\tilde{\mathbf{B}}_I = \frac{1}{A_k} \int_{\Omega_k^s} \mathbf{B}_I\left(\mathbf{x}\right) \mathrm{d}\Omega \tag{3.20}$$

Smoothed stiffness matrix. The standard discretised algebraic system equations for S-FEM is given as

$$\tilde{\mathbf{K}}\mathbf{u}^{\mathrm{h}} = \mathbf{b} \tag{3.21}$$

where the smoothed stiffness matrix $\tilde{\mathbf{K}}$ is defined as

$$\begin{aligned}\tilde{\mathbf{K}} &= \int_{\Omega} \tilde{\mathbf{B}}^{\mathrm{T}}(\mathbf{x})\, \mathbb{C} \tilde{\mathbf{B}}(\mathbf{x})\, \mathrm{d}\Omega \\ &= \sum_{k=1}^{N_e} \int_{\Omega_k^s} \tilde{\mathbf{B}}^{\mathrm{T}}(\mathbf{x})\, \mathbb{C} \tilde{\mathbf{B}}(\mathbf{x})\, \mathrm{d}\Omega \\ &= \sum_{k=1}^{N_e} \tilde{\mathbf{B}}^{\mathrm{T}}(\mathbf{x})\, \mathbb{C} \tilde{\mathbf{B}}(\mathbf{x})\, A_k\end{aligned} \tag{3.22}$$

where N_e is, in particular, the number of edges in ES-FEM[2], $\mathbb{C}$ is the elasticity tensor and the area of smoothing domains is $A_k = \int_{\Omega_k^s} \mathrm{d}\Omega$. The S-FEM stiffness matrix (in Eq. (3.22)) is computed over smoothing domains, not over the element as in FEM, and this procedure does not require the numerical integration scheme which is only required to compute the smoothed strain-displacement matrix $\tilde{\mathbf{B}}$. Note that the external force vector in S-FEM can be obtained exactly as in FEM, since only gradients are only smoothed.

3.4 Summary

Different types of S-FEM models were detailed, cell-based S-FEM (CS-FEM), edge-based S-FEM (ES-FEM) and node-based S-FEM (NS-FEM) for 2D and face-based S-FEM (FS-FEM) for 3D. Their properties were explained in section 3.2.

[2]In NS-FEM, the notation N_e becomes N_n as the number of nodes. Similarly, N_f, the number of faces, is used in FS-FEM.

4 Smoothed finite element method in finite elasticity

Soft materials used in engineering applications traditionally include tyres and rubber. With advances in tissue engineering this list expands to include cell agglomerates and hydrogels. These materials can undergo immense elastic strains. Standard methods are still usable to reproduce such deformation. Enhanced approaches discussed in Chapter 1 can be good alternatives, but those numerical methods still have weaknesses: intrusiveness of implementations, complexity of formulations, requirement of higher-order spaces. The smoothed finite element method (S-FEM) has shown to be an equally worthy alternative which uses lower-order simplex meshes (triangles and tetrahedra). Moreover the approach is easy to implement within the existing codes and can avoid large extent volumetric locking and sensitivity to mesh distortion. Superior stress accuracy is also observed for certain classes of S-FEM and in particular parallelisation of the node-based S-FEM is simple. However current work mainly has concentrated on quasi-incompressible media [101, 104, 107, 108, 113, 114].

In this Chapter, the S-FEM approximation is introduced for finite elasticity. Bubble stabilisation is also proposed to further improve the method's behaviour in an incompressible setting. Section 4.1 recalls finite element approximation as applied to finite elasticity. The main contribution in this Chapter is given in

section 4.2. Firstly the strain smoothing approximation for non-linear elasticity is introduced. Then, to solve Galerkin weak form, the smoothed deformation gradient, the smoothed tangent stiffness matrix, the internal force and the fourth-order elasticity tensor are built on each smoothing domain. Finally the global smoothed system of equations is solved using Newton-Raphson iterative method. Benchmark tests for incompressibility and mesh distortion are given in section 4.3.

4.1 Finite element approximation in finite elasticity

The solution of the non-linear equilibrium equations is achieved by Newton-Raphson method in this Chapter. This process generally involves a *linearisation* procedure. The developments in 2D are presented to simplify the notations, but the approach is identical in 3D.

The Galerkin weak form. The strong form of equilibrium equation in partial differential form is

$$\frac{\partial \sigma_{ij}}{\partial x_j} + b_i = 0 \quad \in \Omega \tag{4.1}$$

where σ_{ij} is the stress and b_i is the external force. From Eq. (4.1), the principle of virtual work for finite elasticity is written as the Galerkin weak form [79, 97, 120]

$$\int_\Omega \frac{\partial \mathcal{W}}{\partial \mathbf{F}} (\mathbf{X}, \mathbf{F}(\mathbf{u})) : \nabla \mathbf{v} d\Omega = \int_\Omega \mathbf{f} \cdot \mathbf{v} d\Omega + \int_{\Gamma_N} \mathbf{g} \cdot \mathbf{v} d\Gamma \tag{4.2}$$

where $\mathbf{v}$ is the set of admissible test functions.

The strain energy density function $\mathcal{W}$ for a compressible neo-Hookean material

[15] is

$$\mathcal{W} = \frac{1}{2}\lambda \left(\ln J\right)^2 - \mu \ln J + \frac{1}{2}\mu \left(\mathrm{tr}\mathbf{C} - 3\right) \tag{4.3}$$

where Lamé's first parameter λ is $\lambda = \kappa - \frac{2}{3}\mu$[1], and the shear modulus $\mu > 0$ and the bulk modulus $\kappa > 0$ are material parameters.

The energy functional and its directional derivatives. From Eq. (4.2) the energy functional ($\mathcal{R}\left(\mathbf{u}\right)$) is given as

$$\mathcal{R}\left(\mathbf{u}\right) = \int_\Omega \frac{\partial \mathcal{W}}{\partial F_{ij}}\left(\mathbf{X}, \mathbf{F}\left(\mathbf{u}\right)\right) \frac{\partial v_i}{\partial X_j} \mathrm{d}\Omega - \int_\Omega f_i v_i \mathrm{d}\Omega - \int_{\Gamma_N} g_i v_i \mathrm{d}\Gamma \tag{4.4}$$

and its directional derivatives ($D\mathcal{R}\left(\mathbf{u}\right) \cdot \mathbf{u}$) are

$$D\mathcal{R}\left(\mathbf{u}\right) \cdot \mathbf{u} = \int_\Omega \frac{\partial^2 \mathcal{W}}{\partial F_{ij} \partial F_{kl}}\left(\mathbf{X}, \mathbf{F}\left(\mathbf{u}\right)\right) \frac{\partial r_k}{\partial X_l} \frac{\partial v_i}{\partial X_j} \mathrm{d}\Omega \tag{4.5}$$

where $i, j, k, l \in \{1, 2, 3\}$ for three dimensional problems and the deformation gradient $\mathbf{F}$ is

$$\mathbf{F} = \left(\frac{\partial \mathbf{x}}{\partial \mathbf{X}}\right)^{\mathrm{T}} \quad \text{or} \quad F_{ij} = \frac{\partial x_i}{\partial X_j} \tag{4.6}$$

where $\mathbf{x}$ is the current configuration $\mathbf{x} = \mathbf{X} + \mathbf{u}$ and $\mathbf{X}$ is the initial configuration. The right Cauchy-Green tensor and the Jacobian can be obtained as $\mathbf{C} = \mathbf{F}^{\mathrm{T}}\mathbf{F}$ and $J = \det \mathbf{F}$, respectively.

Newton-Raphson method. To find an approximate solution to the non-linear set of equations Eq. (4.4), Eq. (4.2) in the displacement field $\mathbf{u}$, the Newton-Raphson method is employed. At iteration iter + 1, knowing the displacement

[1] Lamé's first parameter λ is defined as $\lambda = \kappa - \frac{1}{2}\mu$ in two dimensional (2D) and $\lambda = \kappa - \frac{2}{3}\mu$ in three dimensional (3D) analyses. In this thesis, the strain energy function for hyperelastic material in 3D form is generally considered.

$\mathbf{u}_{\text{iter}}$ from iteration *iter*, find $\mathbf{r}_{\text{iter}}$ that satisfies

$$D\mathcal{R}\left(\mathbf{u}_{\text{iter}}\right)\cdot\mathbf{r}_{\text{iter}}=-\mathcal{R}\left(\mathbf{u}_{\text{iter}}\right) \tag{4.7}$$

The energy functional Eq. (4.4) and its directional derivatives Eq. (4.5) can be re-written

$$\mathcal{R}\left(\mathbf{u}\right)=\int_{\Omega}2\frac{\partial\mathcal{W}}{\partial C_{ij}}F_{ki}\frac{\partial v_k}{\partial X_j}\mathrm{d}\Omega-\int_{\Omega}f_i v_i\mathrm{d}\Omega-\int_{\Gamma_N}g_i v_i\mathrm{d}\Gamma \tag{4.8}$$

$$D\mathcal{R}\left(\mathbf{u}\right)\cdot\mathbf{r}=\int_{\Omega}\left\{\frac{\partial^2\mathcal{W}}{\partial C_{ij}\partial C_{kl}}F_{pi}\frac{\partial v_p}{\partial X_j}F_{sk}\frac{\partial r_s}{\partial X_l}+2\frac{\partial\mathcal{W}}{\partial C_{ij}}\frac{\partial r_k}{\partial X_i}\frac{\partial v_k}{\partial X_j}\right\}\mathrm{d}\Omega \tag{4.9}$$

where $i,j,k,l,p,s\in\{1,2\}$ for 2D and $i,j,k,l,p,s\in\{1,2,3\}$ for 3D.

Tangent stiffness matrix and load vector. The resulting linear algebraic system of equations for the numerical approximation of Eq. (4.7) is assembled into matrix form at each iteration:

$$\begin{bmatrix}K_{11} & K_{12}\\ K_{21} & K_{22}\end{bmatrix}\begin{bmatrix}r_1\\ r_2\end{bmatrix}=\begin{bmatrix}b_1\\ b_2\end{bmatrix} \tag{4.10}$$

By taking $v=\sum_I N_I v_I$, in Eq. (4.9) (where $\mathbf{N}$ is the shape functions), the stiffness matrix $\mathbf{K}$ is obtained with following components

$$K_{11}=\int_{\Omega}\left[4\frac{\partial^2\mathcal{W}}{\partial C_{ij}\partial C_{kl}}\left(\delta_{1i}+\frac{\partial u_1}{\partial X_i}\right)\frac{\partial N_1}{\partial X_j}\left(\delta_{1k}+\frac{\partial u_1}{\partial X_k}\right)\frac{\partial N_1}{\partial X_l}+2\frac{\partial\mathcal{W}}{\partial C_{ij}}\frac{\partial N_1}{\partial X_i}\frac{\partial N_1}{\partial X_j}\right]\mathrm{d}\Omega$$

$$K_{12}=\int_{\Omega}\left[4\frac{\partial^2\mathcal{W}}{\partial C_{ij}\partial C_{kl}}\left(\delta_{1i}+\frac{\partial u_1}{\partial X_i}\right)\frac{\partial N_1}{\partial X_i}\left(\delta_{2k}+\frac{\partial u_2}{\partial X_k}\right)\frac{\partial N_2}{\partial X_l}\right]\mathrm{d}\Omega$$

$$K_{21}=K_{12}$$

$$K_{22}=\int_{\Omega}\left[4\frac{\partial^2\mathcal{W}}{\partial C_{ij}\partial C_{kl}}\left(\delta_{2i}+\frac{\partial u_2}{\partial X_i}\right)\frac{\partial N_2}{\partial X_j}\left(\delta_{2k}+\frac{\partial u_2}{\partial X_k}\right)\frac{\partial N_2}{\partial X_l}+2\frac{\partial\mathcal{W}}{\partial C_{ij}}\frac{\partial N_2}{\partial X_i}\frac{\partial N_2}{\partial X_j}\right]\mathrm{d}\Omega$$

(4.11)

and the components of the load vector are

$$\begin{aligned} b_1 &= -\int_\Omega \left[2\frac{\partial \mathcal{W}}{\partial C_{ij}}\left(\delta_{1i}+\frac{\partial u_1}{\partial X_i}\right)\frac{\partial N_1}{\partial X_j}\right]\mathrm{d}\Omega + \int_\Omega f_1 N_1 \mathrm{d}\Omega + \int_{\Gamma_N} g_1 N_1 \mathrm{d}\Gamma \\ b_2 &= -\int_\Omega \left[2\frac{\partial \mathcal{W}}{\partial C_{ij}}\left(\delta_{2i}+\frac{\partial u_2}{\partial X_i}\right)\frac{\partial N_2}{\partial X_j}\right]\mathrm{d}\Omega + \int_\Omega f_2 N_2 \mathrm{d}\Omega + \int_{\Gamma_N} g_2 N_2 \mathrm{d}\Gamma \end{aligned} \tag{4.12}$$

Then the tangent stiffness matrix $\mathbf{K}^{\mathrm{tan}} = \mathbf{K}^{\mathrm{mat}} + \mathbf{K}^{\mathrm{geo}}$ can be re-written using Eq. (4.11)

$$\begin{aligned} \mathbf{K}^{\mathrm{mat}} &= \int_\Omega \mathbf{B}_0^{\mathrm{T}} \mathbb{C} \mathbf{B}_0 \mathrm{d}\Omega \\ \mathbf{K}^{\mathrm{geo}} &= \int_\Omega \mathcal{B}^{\mathrm{T}} \mathbf{S} \mathcal{B} \mathrm{d}\Omega \end{aligned} \tag{4.13}$$

and by Eq. (4.12) the load vector $\mathbf{b}$ is

$$\mathbf{b} = \int_\Omega \mathbf{B}_0 \left\{\mathbf{S}\right\} \mathrm{d}\Omega \tag{4.14}$$

where the second Piola-Kirchhoff (PK2) stress matrix $\mathbf{S}$ is

$$\mathbf{S} = \begin{bmatrix} S_{11} & S_{12} & 0 & 0 \\ S_{12} & S_{22} & 0 & 0 \\ 0 & 0 & S_{11} & S_{12} \\ 0 & 0 & S_{12} & S_{22} \end{bmatrix} \tag{4.15}$$

and

$$\left\{\mathbf{S}\right\} = \begin{Bmatrix} S_{11} \\ S_{22} \\ S_{12} \end{Bmatrix} \tag{4.16}$$

where the fourth-order elasticity tensors $\mathbb{C}$ are

$$\mathbb{C} = \begin{bmatrix} \mathbb{C}_{11} & \mathbb{C}_{12} & 0 \\ \mathbb{C}_{12} & \mathbb{C}_{22} & 0 \\ 0 & 0 & \mathbb{C}_{66} \end{bmatrix} \tag{4.17}$$

Strain-displacement matrix. The strain-displacement matrices $\mathbf{B}_0$ and $\mathcal{B}$ for 2D can be expressed respectively as

$$\mathbf{B}_0 = \begin{bmatrix} \dfrac{\partial N_I}{\partial X_1}\left(\dfrac{\partial u_1}{\partial X_1}+1\right) & \dfrac{\partial N_I}{\partial X_1}\left(\dfrac{\partial u_2}{\partial X_1}\right) \\ \dfrac{\partial N_I}{\partial X_2}\left(\dfrac{\partial u_1}{\partial X_2}\right) & \dfrac{\partial N_I}{\partial X_2}\left(\dfrac{\partial u_2}{\partial X_2}+1\right) \\ \dfrac{\partial N_I}{\partial X_2}\left(\dfrac{\partial u_1}{\partial X_1}+1\right)+\dfrac{\partial N_I}{\partial X_1}\left(\dfrac{\partial u_1}{\partial X_2}\right) & \dfrac{\partial N_I}{\partial X_1}\left(\dfrac{\partial u_2}{\partial X_2}+1\right)+\dfrac{\partial N_I}{\partial X_2}\left(\dfrac{\partial u_2}{\partial X_1}\right) \end{bmatrix}$$

$$\mathcal{B} = \begin{bmatrix} \dfrac{\partial N_I}{\partial X_1} & 0 \\ \dfrac{\partial N_I}{\partial X_2} & 0 \\ 0 & \dfrac{\partial N_I}{\partial X_1} \\ 0 & \dfrac{\partial N_I}{\partial X_2} \end{bmatrix} \tag{4.18}$$

The global system of equations. The global system of equations (Eq. (4.7)) can be written as

$$\mathbf{K}_{\text{iter}}\mathbf{r}_{\text{iter}} = \mathbf{b}_{\text{iter}} \tag{4.19}$$

and

$$\mathbf{u}_{\text{iter}+1} = \mathbf{u}_{\text{iter}} + \mathbf{r}_{\text{iter}} \tag{4.20}$$

4.2 Strain smoothing finite element approximation in finite elasticity

In this section, the smoothed finite element approximation in finite elasticity is proposed. Since the deformation gradient $\mathbf{F}$ requires to solve the Galerkin weak form, the smoothed deformation gradient $\tilde{\mathbf{F}}$ is given and thus the smoothed right-Cauchy strain tensor $\tilde{\mathbf{C}}$ is computed. Using Newton-Raphson iteration, the smoothed global system of equation is solved.

The smoothed Galerkin weak form. The strong form of the equilibrium equation is (see also Eq. (4.1) and Fig. 4.1)

$$\begin{aligned} &\nabla\boldsymbol{\sigma} + \mathbf{b} = 0 \quad \text{in } \Omega \\ &\boldsymbol{\sigma}\mathbf{n} = \bar{\mathbf{t}} \qquad \text{on } \Gamma_\sigma \\ &\mathbf{u} = \bar{\mathbf{u}} \qquad \text{on } \Gamma_u \end{aligned} \tag{4.21}$$

where $\boldsymbol{\sigma}$ is the internal stress, $\mathbf{b}$ is the external force.

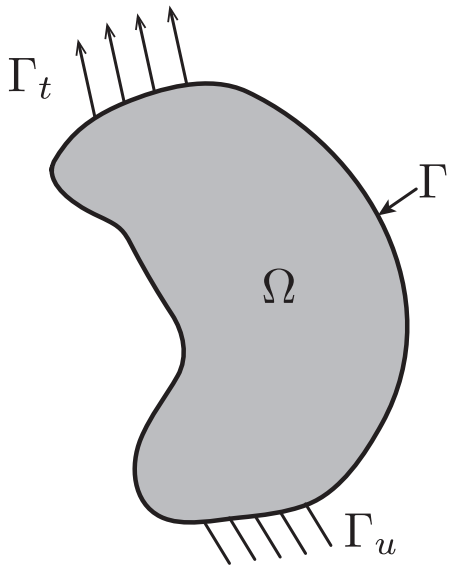

Figure 4.1: 2D homogeneous body: Ω is the body domain, Γ is the boundary, Γ_t is the external force and Γ_u is the boundary conditions

The smoothed deformation gradient $\tilde{\mathbf{F}}$ is defined as (see Fig. 4.2 and Appendix B)

$$\begin{aligned}\tilde{F}_{ij} &= \frac{1}{A_k}\int_{\Omega_k}\left(\frac{\partial u_i^h}{\partial X_j}+\delta_{ij}\right)\Phi\left(\mathbf{x}\right)\mathrm{d}\Omega \\ &= \frac{1}{A_k}\int_{\Omega_k}\left(\frac{\partial u_i^h}{\partial X_j}\right)\Phi\left(\mathbf{x}\right)\mathrm{d}\Omega+\delta_{ij} \\ &= \frac{1}{A_k}\int_{\Omega_k}\sum_{I\in G_k}\left(\frac{\partial N_I}{\partial X_j}u_{iI}\right)\Phi\left(\mathbf{x}\right)\mathrm{d}\Omega+\delta_{ij}\end{aligned} \tag{4.22}$$

where Φ needs to satisfy the following properties (Fig. 4.3)

$$\Phi=\begin{cases}\dfrac{1}{A_k} & \mathbf{x}\in\Omega_k \\ 0 & \text{otherwise}\end{cases}$$

The Galerkin weak form (Eq. (4.2)) can be written for S-FEM

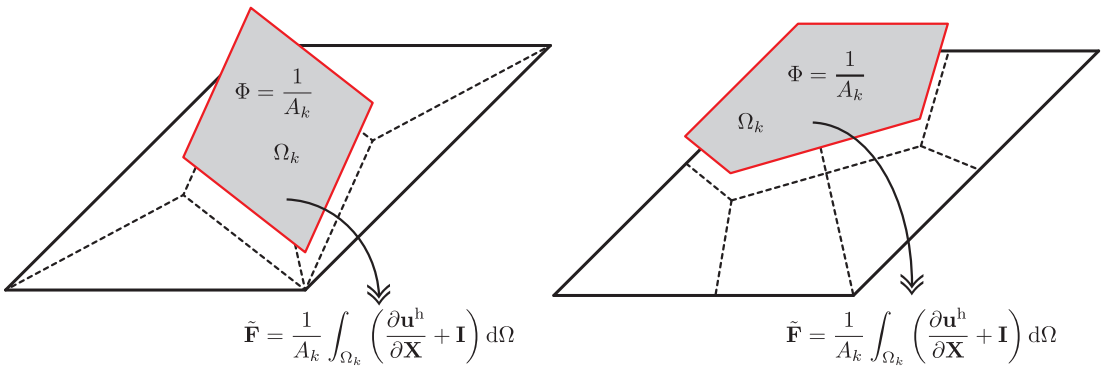

(a) ES-FEM (b) NS-FEM

Figure 4.2: Construction of the smoothed deformation gradient over the smoothing domains

$$\int_\Omega \frac{\partial \mathcal{W}}{\partial \tilde{\mathbf{F}}}\left(\mathbf{X},\tilde{\mathbf{F}}\left(\mathbf{u}\right)\right):\nabla\mathbf{v}\mathrm{d}\Omega=\int_\Omega \mathbf{f}\cdot\mathbf{v}\mathrm{d}\Omega+\int_{\Gamma_N}\mathbf{g}\cdot\mathbf{v}\mathrm{d}\Gamma \tag{4.23}$$

Newton-Raphson method. In the same manner as FEM approximation in finite elasticity, the linearisation is done as in the FEM case (see section 4.1).

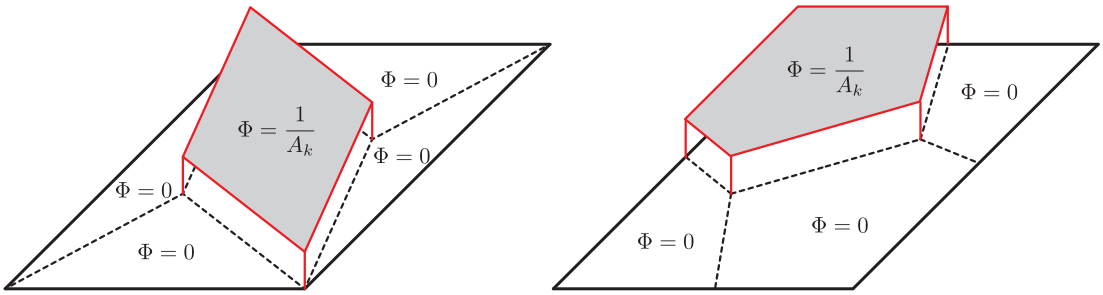

(a) ES-FEM (b) NS-FEM

Figure 4.3: The property of the weight function Φ: (a) ES-FEM and (b) NS-FEM. The weight function is constant (the inverse of the area of smoothing domain) and is zero elsewhere

The smoothed stiffness matrix and load vector. Hence, the matrix form of algebraic system in 2D is

$$\begin{bmatrix} \tilde{K}_{11} & \tilde{K}_{12} \\ \tilde{K}_{12} & \tilde{K}_{22} \end{bmatrix} \begin{bmatrix} r_1 \\ r_2 \end{bmatrix} = \begin{bmatrix} \tilde{b}_1 \\ \tilde{b}_2 \end{bmatrix} \tag{4.24}$$

The smoothed tangent stiffness matrix $\tilde{\mathbf{K}}^{\text{tan}} = \tilde{\mathbf{K}}^{\text{mat}} + \tilde{\mathbf{K}}^{\text{geo}}$ can be expressed by replacing the discretized gradients $\mathbf{B}$ and $\mathcal{B}$ by their smoothed counterparts:

$$\begin{aligned} \tilde{\mathbf{K}}^{\text{mat}} &= \int_{\Omega} \tilde{\mathbf{B}}_0^{\mathrm{T}} \tilde{\mathbb{C}} \tilde{\mathbf{B}}_0 \mathrm{d}\Omega = \sum_{k=1}^{N_e} \int_{\Omega_k^s} \tilde{\mathbf{B}}_0^{\mathrm{T}} \tilde{\mathbb{C}} \tilde{\mathbf{B}}_0 \mathrm{d}\Omega = \sum_{k=1}^{N_e} \tilde{\mathbf{B}}_0^{\mathrm{T}} \tilde{\mathbb{C}} \tilde{\mathbf{B}}_0 A_k \\ \tilde{\mathbf{K}}^{\text{geo}} &= \int_{\Omega} \tilde{\mathcal{B}}^{\mathrm{T}} \tilde{\mathbf{S}} \tilde{\mathcal{B}} \mathrm{d}\Omega = \sum_{k=1}^{N_e} \int_{\Omega_k^s} \tilde{\mathcal{B}}^{\mathrm{T}} \tilde{\mathbf{S}} \tilde{\mathcal{B}} \mathrm{d}\Omega = \sum_{k=1}^{N_e} \tilde{\mathcal{B}}^{\mathrm{T}} \tilde{\mathbf{S}} \tilde{\mathcal{B}} A_k \end{aligned} \tag{4.25}$$

where N_e is the number of edges for ES-FEM[2] and the stress matrix $\tilde{\mathbf{S}}$ for 2D is

$$\tilde{\mathbf{S}} = \begin{bmatrix} \tilde{S}_{11} & \tilde{S}_{12} & 0 & 0 \\ \tilde{S}_{12} & \tilde{S}_{22} & 0 & 0 \\ 0 & 0 & \tilde{S}_{11} & \tilde{S}_{12} \\ 0 & 0 & \tilde{S}_{12} & \tilde{S}_{22} \end{bmatrix} \tag{4.26}$$

[2]Note that in NS-FEM N_n which is a number of nodes can be used and N_f for FS-FEM is a number of faces.

The load vector $\tilde{\mathbf{b}}$ is

$$\tilde{\mathbf{b}} = \sum_{k=1}^{N_e} \tilde{\mathbf{B}}_0 \left\{\tilde{\mathbf{S}}\right\} A_k \tag{4.27}$$

where the stress vector $\left\{\tilde{\mathbf{S}}\right\}$ is given by

$$\left\{\tilde{\mathbf{S}}\right\} = \begin{Bmatrix} \tilde{S}_{11} \\ \tilde{S}_{22} \\ \tilde{S}_{12} \end{Bmatrix} \tag{4.28}$$

The stresses $\tilde{\mathbf{S}}$ are given by Eq. (A.9) in Appendix A

$$\tilde{\mathbf{S}} = \mu \left(\mathbf{I} - \tilde{\mathbf{C}}^{-1}\right) + \lambda \ln \tilde{J}\, \tilde{\mathbf{C}}^{-1} \tag{4.29}$$

and the elasticity tensors can be expressed by Eq. (A.18) in Appendix A

$$\tilde{\mathbb{C}}_{ijkl} = \lambda \left(\tilde{C}^{-1}_{ij} \tilde{C}^{-1}_{kl}\right) + \left(\mu - \lambda \ln \tilde{J}\right) \left[\tilde{C}^{-1}_{ik} \tilde{C}^{-1}_{jl} + \tilde{C}^{-1}_{il} \tilde{C}^{-1}_{jk}\right] \tag{4.30}$$

where the smoothed Jacobian $\tilde{J} = \det \tilde{\mathbf{F}}$.

The smoothed strain-displacement matrix. The smoothed strain-displacement matrices $\tilde{\mathbf{B}}_0$ and $\tilde{\mathcal{B}}$ for 2D and 3D are respectively given by

$$\begin{aligned} \tilde{\mathbf{B}}_0(\mathbf{x}) &= \begin{bmatrix} \tilde{\mathbf{B}}_{I1}\tilde{F}_{11} & \tilde{\mathbf{B}}_{I1}\tilde{F}_{21} \\ \tilde{\mathbf{B}}_{I2}\tilde{F}_{12} & \tilde{\mathbf{B}}_{I2}\tilde{F}_{22} \\ \tilde{\mathbf{B}}_{I2}\tilde{F}_{11} + \tilde{\mathbf{B}}_{I1}\tilde{F}_{12} & \tilde{\mathbf{B}}_{I1}\tilde{F}_{22} + \tilde{\mathbf{B}}_{I2}\tilde{F}_{21} \end{bmatrix}(\mathbf{x}) \\ \tilde{\mathcal{B}}(\mathbf{x}) &= \begin{bmatrix} \tilde{\mathbf{B}}_{I1} & 0 \\ \tilde{\mathbf{B}}_{I2} & 0 \\ 0 & \tilde{\mathbf{B}}_{I1} \\ 0 & \tilde{\mathbf{B}}_{I2} \end{bmatrix}(\mathbf{x}) \end{aligned} \tag{4.31}$$

and

$$\tilde{\mathbf{B}}_0(\mathbf{x}) = \begin{bmatrix} \tilde{\mathbf{B}}_{I1}\tilde{F}_{11} & \tilde{\mathbf{B}}_{I1}\tilde{F}_{21} & \tilde{\mathbf{B}}_{I1}\tilde{F}_{31} \\ \tilde{\mathbf{B}}_{I2}\tilde{F}_{12} & \tilde{\mathbf{B}}_{I2}\tilde{F}_{22} & \tilde{\mathbf{B}}_{I2}\tilde{F}_{32} \\ \tilde{\mathbf{B}}_{I3}\tilde{F}_{13} & \tilde{\mathbf{B}}_{I3}\tilde{F}_{23} & \tilde{\mathbf{B}}_{I3}\tilde{F}_{33} \\ \tilde{\mathbf{B}}_{I2}\tilde{F}_{11} + \tilde{\mathbf{B}}_{I1}\tilde{F}_{12} & \tilde{\mathbf{B}}_{I2}\tilde{F}_{21} + \tilde{\mathbf{B}}_{I1}\tilde{F}_{22} & \tilde{\mathbf{B}}_{I2}\tilde{F}_{31} + \tilde{\mathbf{B}}_{I1}\tilde{F}_{32} \\ \tilde{\mathbf{B}}_{I3}\tilde{F}_{12} + \tilde{\mathbf{B}}_{I2}\tilde{F}_{13} & \tilde{\mathbf{B}}_{I3}\tilde{F}_{22} + \tilde{\mathbf{B}}_{I2}\tilde{F}_{23} & \tilde{\mathbf{B}}_{I3}\tilde{F}_{32} + \tilde{\mathbf{B}}_{I2}\tilde{F}_{33} \\ \tilde{\mathbf{B}}_{I3}\tilde{F}_{11} + \tilde{\mathbf{B}}_{I1}\tilde{F}_{13} & \tilde{\mathbf{B}}_{I3}\tilde{F}_{21} + \tilde{\mathbf{B}}_{I1}\tilde{F}_{23} & \tilde{\mathbf{B}}_{I3}\tilde{F}_{31} + \tilde{\mathbf{B}}_{I1}\tilde{F}_{33} \end{bmatrix}(\mathbf{x})$$

$$\tilde{\mathcal{B}}(\mathbf{x}) = \begin{bmatrix} \tilde{\mathbf{B}}_{I1} & 0 & 0 \\ \tilde{\mathbf{B}}_{I2} & 0 & 0 \\ \tilde{\mathbf{B}}_{I3} & 0 & 0 \\ 0 & \tilde{\mathbf{B}}_{I1} & 0 \\ 0 & \tilde{\mathbf{B}}_{I2} & 0 \\ 0 & \tilde{\mathbf{B}}_{I3} & 0 \\ 0 & 0 & \tilde{\mathbf{B}}_{I1} \\ 0 & 0 & \tilde{\mathbf{B}}_{I2} \\ 0 & 0 & \tilde{\mathbf{B}}_{I3} \end{bmatrix}(\mathbf{x}) \tag{4.32}$$

where the smoothed strain-displacement matrix $\tilde{\mathbf{B}}_I(\mathbf{x})$ is given in Eq. (3.19) in Chapter 3 (see also Figs. 3.3, 3.6, 3.9 and 3.10).

The smoothed global system of equations. The smoothed global system of equations Eq. (4.7) at each Newton-Raphson iteration can be written as

$$\tilde{\mathbf{K}}_{\text{iter}}\mathbf{r}_{\text{iter}} = \tilde{\mathbf{b}}_{\text{iter}} \tag{4.33}$$

and the updated displacement $\mathbf{u}$ obtained by the Newton-Raphson method is

$$\mathbf{u}_{\text{iter}+1} = \mathbf{u}_{\text{iter}} + \mathbf{r}_{\text{iter}} \tag{4.34}$$

4.3 Numerical results

In this section, numerical examples are presented in order to demonstrate the performance of the methods discussed so far in finite elasticity. For the implementation, the first derivative of strain energy density with respect to the right Cauchy-Green deformation tensor $\mathbf{C}$, which represents the stress, and the second derivatives of strain density of neo-Hookean model with respect to the right Cauchy-Green deformation tensor, which expresses the elasticity tensors $\mathbb{C}$, are needed. Those will be defined in section 4.3.1.

Simple shear deformation with Dirichlet boundary conditions (BCs) and Neumann BCs will be analysed in section 4.3.2. In following sections 4.3.3 and 4.3.4, the uniform extension with lateral contraction with Dirichlet and Neumann BCs, "Not-so-simple" shear deformation with Dirichlet BCs and simple torsion of a solid cylinder with Dirichlet BCs will be investigated, respectively. The examples are taken from References [60, 97, 120, 123] and have some analytical solutions.

In addition, near-incompressibility and mesh distortion sensitivity are studied in sections 4.3.5 and 4.3.6. For quasi-incompressibility, Cook's membrane is used with bulk moduli $\kappa = 100$, $1,000$ and $10,000$, which Poisson's ratio is close to 0.5. The bending of a rectangle is solved with highly distorted meshes. Since an analytical solution for Cook's membrane does not exist, a numerical solution using DOLFIN [90, 91], using the MINI element with a very fine mesh, is used as a reference solution. The rectangle bending example is introduced in Reference [123] and has an analytical solution.

These numerical examples are chosen as benchmarks with following parameters for Newton-Raphson iteration: tolerance is 10^{-9}, the number of load step is $50 \sim 100$ and the number of iteration to convergence is about $4 \sim 6$, including quadratic convergence of the Newton-Raphson algorithm.

Code details and implementation. All following numerical results for FEM and S-FEM are obtained by MATLAB codes[3]. In 2D, 3-noded triangular elements for FEM and 3-noded triangular and 4-noded bubble-enriched triangular elements for edge-based and node-based S-FEM are used, respectively. For 3D, FEM with 4-noded simplex tetrahedral element and FS-FEM with 4-noded tetrahedral and 5-noded tetrahedral elements with the bubble functions are used.

For pseudo-analytical results, python scripts of the MINI element[4] are used in DOLFIN finite element software with very fine meshes (GDof $= 816,080,000$). For the MINI element, 4-noded triangular and 5-noded tetrahedral elements for 2D and 3D problems are used, respectively. Python scripts used in this thesis are based on website[5] and Reference [6] (also a example script is provided in Appendix E).

Computational time. All numerical examples are simulated on the Intel CPU desktop (Inter Core i5 3.33 GHz and 8.00 GB RAM) operated by Ubuntu[6]. Note that GPU and parallelism are not considered in this thesis.

For Cook's membrane problem in section 5.3.1, when bulk modulus $\kappa = 10^7$, the number of elements 100×100 and the number of load step 100 are used, actual simulation time is almost 1 day for FEM and around $2 \sim 3$ days for S-FEM on MATLAB.

[3]MATLAB codes for FEM and S-FEM used for numerical experiments can be found on computationalmechanicsos on SourceForge (https://sourceforge.net/projects/computationalmechanaicsos/)

[4]The MINI element is a model for the Stokes problem. The velocity and the pressure are approximated at the internal degrees of freedom in each element [2].

[5]FEniCS project (http://fenicsproject.org/documentation/dolfin/dev/python/demo/pde/hyperelasticity/python/documentation.html).

[6]A Debian-based Linux operating system (http://www.ubuntu.com/).

4.3.1 Neo-Hookean model

For all numerical tests in this work the neo-Hookean model will be used. This model is the simplest hyperelastic model and is isotropic. The stored energy function of neo-Hookean material given in Reference [15] is

$$\mathcal{W}(\mathbf{C}) = \frac{1}{2}(\ln J)^2 - \mu_0 \ln J + \frac{1}{2}\mu_0 (\mathrm{tr}\mathbf{C} - 3) \tag{4.35}$$

where λ_0 and μ_0 are Lamé's first parameter and Lamé's second parameter (or often called shear modulus) respectively and the Jacobian $J = \det \mathbf{F}$. The invariants of tensors I_1, I_2 and I_3 are shown in Eq. (2.3) and their derivatives are given in Table 4.1.

Table 4.1: The derivatives of the principal invariants of the right Cauchy-Green tensor with respect to itself (also see A.5∼A.8 in Appendix A)

The derivatives of principal invariants of the right Cauchy-Green tensor	
$\dfrac{\partial I_1}{\partial \mathbf{C}} = \mathbf{I}$	$\dfrac{\partial I_1}{\partial C_{ij}} = \delta_{ij}$
$\dfrac{\partial I_2}{\partial \mathbf{C}} = I_1\mathbf{I} - \mathbf{C}^{\mathrm{T}}$	$\dfrac{\partial I_2}{\partial C_{ij}} = C_{kk}\delta_{ij} - C_{ji}$
$\dfrac{\partial I_3}{\partial \mathbf{C}} = I_3\mathbf{C}^{-\mathrm{T}}$	$\dfrac{\partial I_3}{\partial C_{ij}} = I_3 C^{-1}_{ji}$

Expressing the first derivative of the stored energy with respect to the right Cauchy-Green tensor $\mathbf{C}$, the second Piola-Kirchhoff stress tensor (PK2 or $\mathbf{S}$) of a neo-Hookean material can be obtained by the chain rule using the principal

invariants and its derivatives are given in Eq. (2.3) and Table 4.1

$$\begin{aligned}\mathbf{S} = \frac{\partial \mathcal{W}}{\partial \mathbf{C}} &= \frac{\partial \mathcal{W}}{\partial I_1}\frac{\partial I_1}{\partial \mathbf{C}} + \frac{\partial \mathcal{W}}{\partial I_2}\frac{\partial I_2}{\partial \mathbf{C}} + \frac{\partial \mathcal{W}}{\partial I_3}\frac{\partial I_3}{\partial \mathbf{C}} \\ &= \frac{\partial \mathcal{W}}{\partial I_1}\mathbf{I} + \frac{\partial \mathcal{W}}{\partial I_2}\left(I_1\mathbf{I} - \mathbf{C}\right)\frac{\partial \mathcal{W}}{\partial I_3} I_3 \mathbf{C}^{-1}\end{aligned} \tag{4.36}$$

where the right Cauchy-Green deformation tensor $\mathbf{C}$ is defined by the deformation gradient $\mathbf{F}$ as

$$\mathbf{C} = \mathbf{F}^{\mathrm{T}}\mathbf{F} \tag{4.37}$$

The elasticity tensors are determined as the second derivatives of stored energy function with respect to the right Cauchy-Green deformation, are given as (see Appendix A and References [15, 21])

$$\mathbb{C}_{ijkl} = \lambda C^{-1}_{ij} C^{-1}_{kl} + \mu\left(C^{-1}_{ik} C^{-1}_{jl} + C^{-1}_{il} C^{-1}_{kj}\right) \tag{4.38}$$

where $\lambda = \lambda_0$ and $\mu = \mu_0 - \lambda \ln J$.

4.3.2 Simple shear deformation

This example is one of the most popular benchmark tests because of the existence of analytical solutions in finite elasticity. Two boundary conditions cases are considered; (1) Dirichlet BCs and (2) mixed Dirichlet and Neumann boundary conditions. Fig. 4.4 shows the geometry of this problem.

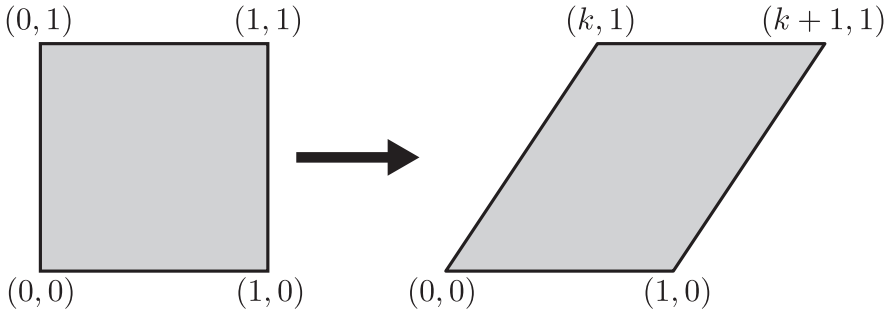

Figure 4.4: Simple shear deformation of a unit square

The deformation gradient for the simple shear deformation takes following form:

$$\mathbf{F} = \begin{bmatrix} 1 & k & 0 \\ 0 & 1 & 0 \\ 0 & 0 & 1 \end{bmatrix} \tag{4.39}$$

where $k > 0$.

For the simple shear deformation problem, the shear and bulk moduli $\mu = 0.6$ and $\kappa = 100$ are used, respectively. When a higher value of κ is used, the material is more incompressible. The number of three-node triangular (T3) elements in the $x-$ and $y-$directions are 4×4, 8×8, 16×16 and 32×32. The analytical solution can be written

$$\mathcal{W} = \frac{\mu}{2} k^2 \tag{4.40}$$

The analytical solution can be calculated by Eq. (4.40) with given material parameters, deformation $k = 1$, shear modulus $\mu = 0.6$ and bulk modulus $\kappa = 100$, and therefore the strain energy $\mathcal{W} = 0.3$ (see in Appendices C.1 and D.1).

Fig. 4.5 represents the strain energy convergence for the simple shear with Dirichlet and mixed Dirichlet and Neumann boundary conditions. The x- and y-axes represent the logarithm of the total number of degrees of freedom. For

this problem, it is clearly seen that the analytical solution $\mathcal{W} = 0.3$ is reproduced to machine precision regardless of the mesh size. All methods provide the exact results down to machine precision.

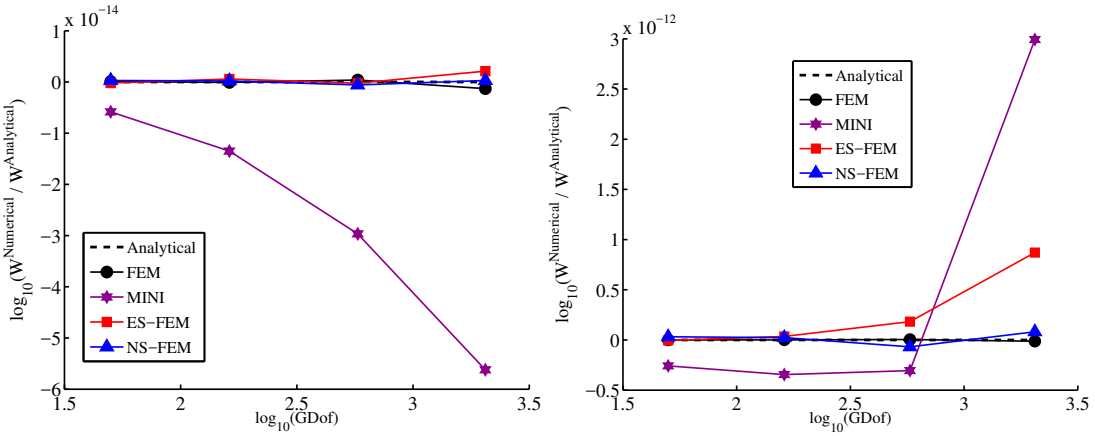

(a) Dirichlet BCs (b) mixed Dirichlet and Neumann BCs

Figure 4.5: Strain energy convergence for the simple shear deformation (FEM, ES-FEM, NS-FEM and the MINI): (a) Dirichlet BCs and (b) mixed Dirichlet and Neumann BCs

The detailed values of the relative error in strain energy for the simple shear are provided in Tables 4.2 and 4.3 for various meshes (4×4, 8×8, 16×16 and 32×32). Such relative error is computed by

$$\mathcal{W}^{\text{error}} = \frac{\mathcal{W}^{\text{Numerical}} - \mathcal{W}^{\text{Analytical}}}{\mathcal{W}^{\text{Analytical}}} \times 100$$

The value of the relative error is denoted by the percentage. From Table 4.2 and 4.3, the value provided by the strain smoothing formulations are exact within machine precision.

Table 4.2: Strain energy relative error for the simple shear deformation with Dirichlet boundary conditions (FEM, ES-FEM, NS-FEM and the MINI ($\times 10^{-11}\%$))

Num. of elements	FEM	ES-FEM	NS-FEM	MINI
4×4	0.0019	-0.0037	0.0056	-0.1351
8×8	-0.0019	0.0148	0.0037	-0.3109
16×16	0.0093	-0.0056	-0.0130	-0.6828
32×32	-0.0296	0.0500	0.0056	-1.2952

Strain energy relative error is given by: $\left(\frac{W^{\text{Numerical}} - W^{\text{Analytical}}}{W^{\text{Analytical}}}\right) \times 100\%$.

Table 4.3: Strain energy relative error for simple shear deformation with mixed Dirichlet and Neumann boundary conditions (FEM, ES-FEM, NS-FEM and the MINI ($\times 10^{-11}\%$))

Num. of elements	FEM	ES-FEM	NS-FEM	MINI
4×4	0.0000	-0.0111	0.0722	-0.5958
8×8	0.0019	0.0814	0.0537	-0.7938
16×16	0.0093	0.4200	-0.1591	-0.7031
32×32	-0.0296	2.0040	0.1869	6.8926

Strain energy relative error is given by: $\left(\frac{W^{\text{Numerical}} - W^{\text{Analytical}}}{W^{\text{Analytical}}}\right) \times 100\%$.

4.3.3 Uniform extension with lateral contraction

The next benchmark test is uniform extension with lateral contraction with Dirichlet and mixed Dirichlet and Neumann boundary conditions. The geometry of this problem is a unit square and shear modulus $\mu = 0.6$ and bulk modulus $\kappa = 100$ are used. Used sizes of T3 meshes are 4×4, 8×8, 16×16 and 32×32.

The deformation gradient and the strain energy are given respectively (details are

given in Appendices C.2 and D.2):

$$\mathbf{F} = \begin{bmatrix} \lambda_1 & 0 & 0 \\ 0 & \lambda_2 & 0 \\ 0 & 0 & \lambda_3 \end{bmatrix} \tag{4.41}$$

and

$$\mathcal{W} = \frac{\mu}{2}\left(\lambda_1^2 + \frac{1}{\lambda_1^2} - 2\right) \tag{4.42}$$

The strain energy convergence of FEM, ES-FEM and NS-FEM are shown in Fig. 4.6. Since the test has the analytical solution, numerical solutions of given methods are close to the analytical solution, $\mathcal{W} \approx 0.02359$, with either coarse or finer meshes. Furthermore, like simple shear deformation problems, a fraction is within machine precision with portion 10^{-14}.

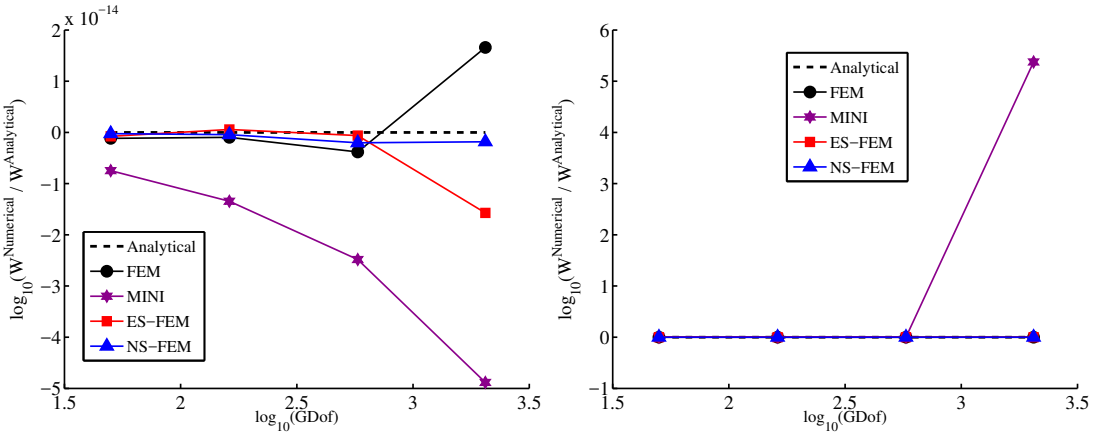

(a) Dirichlet BCs (b) mixed Dirichlet and Neumann BCs

Figure 4.6: Strain energy convergence for the uniform extension with lateral contraction (FEM, ES-FEM, NS-FEM and the MINI): (a) Dirichlet BCs and (b) mixed Dirichlet and Neumann BCs

Tables 4.4 and 4.5 provide the values of the relative error in strain energy. The errors provided by S-FEM are under machine precision with the coarse to fine

meshes.

Table 4.4: Strain energy relative error for the uniform extension with lateral contraction with Dirichlet boundary conditions (FEM, ES-FEM, NS-FEM and the MINI ($\times 10^{-11}\%$))

Num. of elements	FEM	ES-FEM	NS-FEM	MINI
4×4	-0.0265	-0.0176	-0.0059	-0.1721
8×8	-0.0221	0.0132	-0.0103	-0.3103
16×16	-0.0882	-0.0147	-0.0471	-0.5720
32×32	0.3809	-0.3618	-0.0426	-1.1250

Strain energy relative error is given by: $\left(\frac{W^{\text{Numerical}} - W^{\text{Analytical}}}{W^{\text{Analytical}}}\right) \times 100\%$.

Table 4.5: Strain energy relative error for the uniform extension with lateral contraction with mixed Dirichlet and Neumann boundary conditions (FEM, ES-FEM, NS-FEM and the MINI ($\times 10^{-11}\%$))

Num. of elements	FEM	ES-FEM	NS-FEM	MINI
4×4	-0.0882	-0.0868	-0.0838	0.0294
8×8	-0.0985	-0.0765	-0.0897	0.2073
16×16	-0.1176	-0.1412	-0.1088	0.5662
32×32	-0.0338	-0.4132	-0.1000	1.4205

Strain energy relative error is given by: $\left(\frac{W^{\text{Numerical}} - W^{\text{Analytical}}}{W^{\text{Analytical}}}\right) \times 100\%$.

4.3.4 "Not-so-simple" shear deformation

In this section, a non-homogeneous deformation example denoted "Not-so-simple" shear deformation is examined. Fig. 4.7 illustrates the initial and current configurations of the problem. The geometry is $(0, 2) \times (0, 2)$. The following T3 meshes

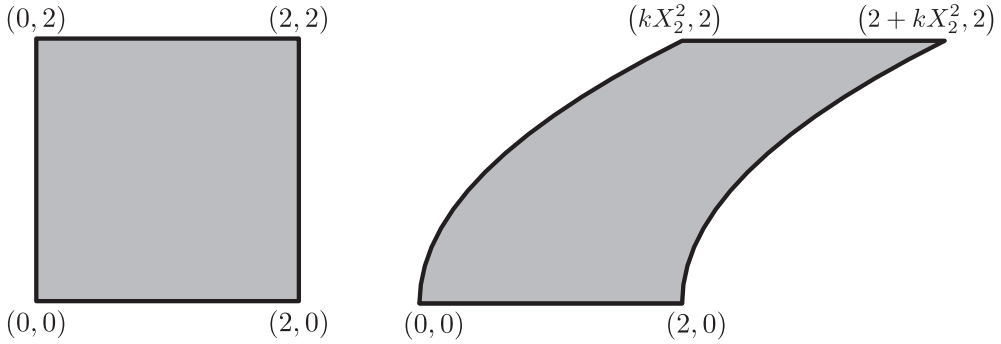

Figure 4.7: "Not-so-simple" shear deformation: the geometry and deformations

are used in the numerical examples: 4×4, 8×8, 16×16 and 32×32.

Current configuration of this problem is

$$x_1 = X_1 + kX_2^2, \quad x_2 = X_2, \quad x_3 = X_3 \tag{4.43}$$

and this can be expressed in the form of deformation gradient:

$$\mathbf{F} = \begin{bmatrix} 1 & 2kX_2 & 0 \\ 0 & 1 & 0 \\ 0 & 0 & 1 \end{bmatrix} \tag{4.44}$$

where $k > 0$ (Appendices C.3 and D.3).

The strain energy convergence for the "Not-so-simple" problem is illustrated in Fig. 4.8. In this problem, interestingly, the standard FEM shows faster convergence than ES-FEM and NS-FEM while the MINI element performs very well. The relative error in strain energy of the FEM, the MINI, ES-FEM and NS-FEM are provided in Table 4.6. The MINI element is more accurate than S-FEM, however errors for ES-FEM and NS-FEM are globally small about -0.35% and -0.4%, respectively.

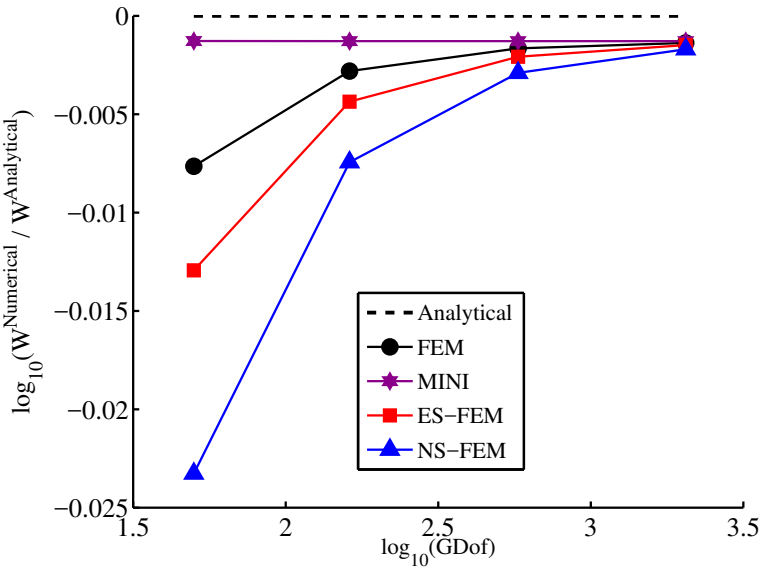

Figure 4.8: Convergence in strain energy for "Not-so-simple" shear deformation with Dirichlet boundary conditions (FEM, ES-FEM, NS-FEM and the MINI)

Table 4.6: Strain energy relative error for the "Not-so-simple" shear deformation with Dirichlet boundary conditions (FEM, ES-FEM, NS-FEM and the MINI)

Num. of elements	FEM	ES-FEM	NS-FEM	MINI
4×4	-1.7452	-2.9355	-5.2169	-0.2945
8×8	-0.6442	-1.0001	-1.6983	-0.2953
16×16	-0.3799	-0.4774	-0.6662	-0.2955
32×32	-0.3162	-0.3419	-0.3902	-0.2956

Strain energy relative error is given by: $\left(\frac{W^{\text{Numerical}} - W^{\text{Analytical}}}{W^{\text{Analytical}}}\right) \times 100\%$.

4.3.5 Near-incompressibility

It has been demonstrated that S-FEM effectively alleviates locking issues in linear elasticity. The finite deformation case is studied here. To do so, near-incompressibility problems with different bulk moduli κ are tested in this section. With different bulk moduli $\kappa = 10^2$, 10^3 and 10^4 which Poisson's ratio is close to 0.5 ($\nu \to 0.5$), the model becomes nearly-incompressible. The geometry of the problem, Cook's membrane which is a popular structure in engineering, is illustrated in Fig. 4.9.

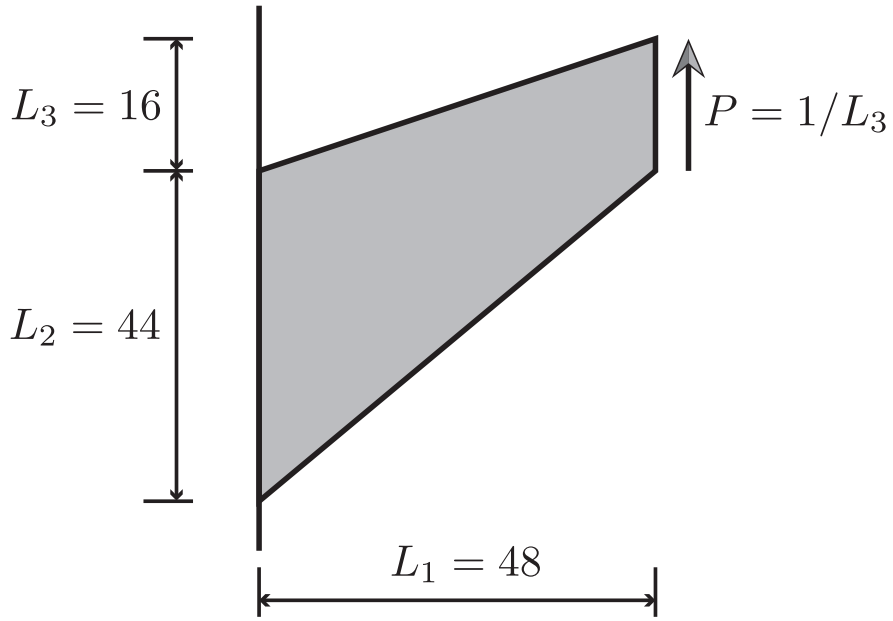

Figure 4.9: The geometry of Cook's membrane with bending load.

Fig. 4.10 shows the convergence of the strain energy for the standard FEM, the MINI element, ES-FEM and NS-FEM with T3 elements. The numbers of elements along each side are 4×4, 8×8, 10×10, 16×16, 20×20, 32×32, 40×40 and 100×100. Because an analytical solution is not available for this problem, a reference solution using a mixed finite element method on a highly-refined mesh with the DOLFIN finite element software is calculated numerically [90, 91]. A non-locking FEM, the MINI element using the DOLIFIN in this work, is compared to

strain smoothing. In Fig. 4.10, the x- and y-directions represent the logarithm of the total number of degrees of freedom and the logarithm of the ratio between the numerical and analytical solution, respectively. The black dashed-line represents the reference solution computed by DOLFIN.

Although the MINI element provides better accuracy than S-FEM, edge-based and node-based S-FEM are relatively accurate and reliable for both compressible and quasi-incompressible problems (see Fig. 4.10). When the Poisson's ratio is close to 0.5, the convergence of the ES-FEM becomes slower. The NS-FEM provides here an upper bound solution.

When Poisson's ratio is close to 0.5 ($\nu \rightarrow 0.5$), the MINI element avoids locking. However it is clearly shown that S-FEM models handle excellently near-incompressibility as shown in Tables 4.7, 4.8 and 4.9. Particularly results provided by NS-FEM are much more accurate than FEM and even ES-FEM. Relative error is given by

$$\left(\frac{W^{\text{Numerical}} - W^{\text{Reference}}}{W^{\text{Reference}}} \right) \times 100\% \tag{4.45}$$

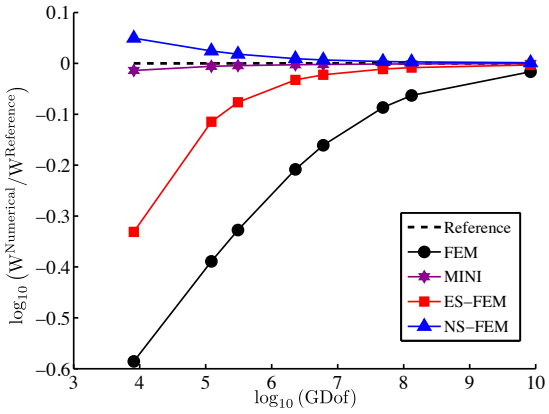

(a) Strain energies with bulk modulus $\kappa = 10^2$

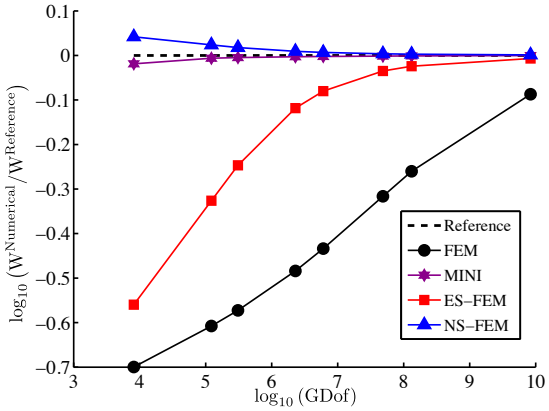

(b) Strain energies with bulk modulus $\kappa = 10^3$

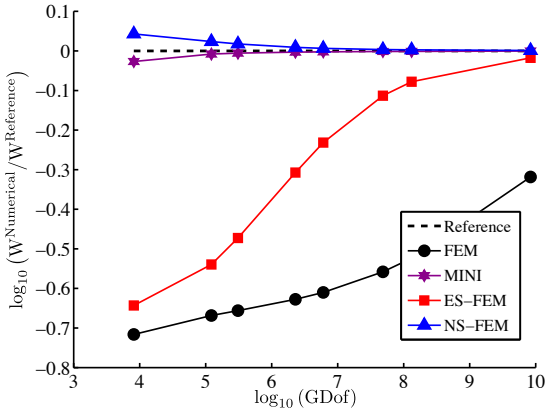

(c) Strain energies with bulk modulus $\kappa = 10^4$

Figure 4.10: Strain energy convergence for the Cook membrane with bulk moduli $\kappa = 10^2$, $\kappa = 10^3$ and $\kappa = 10^4$: $\mathrm{W}^{\mathrm{Numerical}}$ is the numerical solution of the standard FEM, the MINI element and S-FEM models, and $\mathrm{W}^{\mathrm{Reference}}$ is the solution of the DOLFIN finite element software

Table 4.7: Strain energy relative error for Cook's membrane (the standard FEM, ES-FEM, NS-FEM and the MINI element) with bulk modulus $\kappa = 10^2$

Num. of elements	FEM	ES-FEM	NS-FEM	MINI
4×4	-44.3239	-28.1828	5.0776	-1.3837
8×8	-32.2319	-10.8392	2.4749	-0.5685
10×10	-27.9243	-7.3515	1.8224	-0.4450
16×16	-18.8038	-3.2010	0.9324	-0.2731
20×20	-14.8639	-2.2123	0.6809	-0.2177
32×32	-8.3037	-1.1087	0.3672	-0.1338
40×40	-6.1115	-0.8299	0.2826	-0.1049
100×100	-1.6339	-0.3016	0.1279	-0.0282

Strain energy relative error is given by: $\left(\frac{W^{\text{Numerical}} - W^{\text{Reference}}}{W_{\text{Reference}}}\right) \times 100\%$.

Table 4.8: Strain energy relative error for Cook's membrane (the standard FEM, ES-FEM, NS-FEM and the MINI element) with bulk modulus $\kappa = 10^3$

Num. of elements	FEM	ES-FEM	NS-FEM	MINI
4×4	-50.3251	-42.8593	4.2691	-1.8554
8×8	-45.5338	-27.8347	2.4078	-0.6243
10×10	-40.5950	-21.8614	1.7890	-0.4761
16×16	-38.3660	-11.1631	0.9216	-0.2856
20×20	-35.1881	-7.7029	0.6743	-0.2268
32×32	-27.1125	-3.4408	0.3649	-0.1392
40×40	-22.9043	-2.3912	0.2813	-0.1092
100×100	-8.3459	-0.6855	0.1289	-0.0299

Strain energy relative error is given by: $\left(\frac{W^{\text{Numerical}} - W^{\text{Reference}}}{W^{\text{Reference}}}\right) \times 100\%$.

Table 4.9: Strain energy relative error for Cook's membrane (the standard FEM, ES-FEM, NS-FEM and the MINI element) with bulk modulus $\kappa = 10^4$

Num. of elements	FEM	ES-FEM	NS-FEM	MINI
4×4	-51.1435	-47.4285	4.3948	-2.6696
8×8	-48.7502	-41.6966	2.3891	-0.8229
10×10	-48.1096	-37.6685	1.7776	-0.5938
16×16	-46.6042	-26.4562	0.9102	-0.3359
20×20	-45.6693	-20.6668	0.6647	-0.2676
32×32	-42.7694	-10.6931	0.3593	-0.1737
40×40	-40.7629	-7.4866	0.2769	-0.1429
100×100	-27.2710	-1.1743	0.1269	-0.0631

Strain energy relative error is given by: $\left(\frac{W^{\text{Numerical}} - W^{\text{Reference}}}{W^{\text{Reference}}}\right) \times 100\%$.

4.3.6 Mesh distortion sensitivity

In this section, mesh distortion sensitivity problems in large deformations are examined. For this test, artificially distorted meshes which are given by [25] are used

$$\begin{aligned} x' &= x + r_c\, \alpha_{\text{distorted}}\, \Delta x \\ y' &= y + r_c\, \alpha_{\text{distorted}}\, \Delta y \end{aligned} \tag{4.46}$$

where r_c is a random number between -1.0 and 1.0, $\alpha_{\text{distorted}}$ is the magnitude of the distortion and Δx, Δy are initial regular element size in the x- and y-directions. The higher $\alpha_{\text{distorted}}$ the more distorted the mesh.

The geometry of the example is given in Section 2.2.6 and 5.2.4 in Reference [123] (see also Fig. 4.11). Consider a rectangular block in the reference Cartesian coordinates (X, Y, Z) defined by

$$X = (A_1, A_2)\,, \quad Y = (-B, B)\,, \quad Z = (0, 0) \tag{4.47}$$

where $(A_1, A_2, B > 0)$.

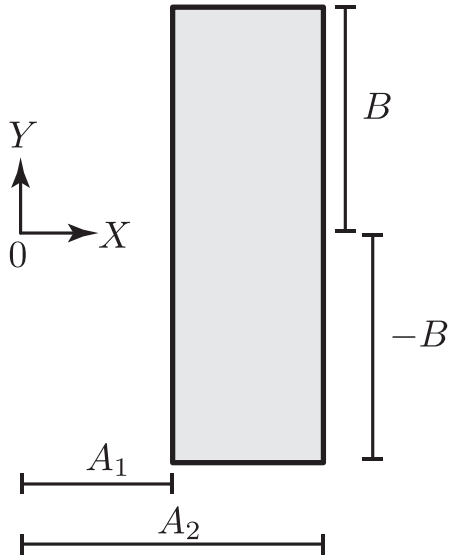

Figure 4.11: The geometry of the bending example.

The corresponding unit vectors for cylindrical coordinates (r, θ, z) are

$$\mathbf{e}_r = \begin{bmatrix} \cos\theta \\ \sin\theta \\ 0 \end{bmatrix}, \quad \mathbf{e}_\theta = \begin{bmatrix} -\sin\theta \\ \cos\theta \\ 0 \end{bmatrix}, \quad \mathbf{e}_z = \begin{bmatrix} 0 \\ 0 \\ 0 \end{bmatrix} \tag{4.48}$$

The deformation in cylindrical coordinates is

$$r = f(X) = \sqrt{2\alpha X}, \quad \theta = g(Y) = \frac{1}{\alpha} Y, \quad z = Z \tag{4.49}$$

For implementation, cylindrical coordinates are needed in Cartesian coordinates

$$\begin{aligned} x &= r\cos\theta = \sqrt{2\alpha X}\cos\frac{Y}{\alpha} \\ y &= r\sin\theta = \sqrt{2\alpha X}\sin\frac{Y}{\alpha} \\ z &= 0 \end{aligned} \tag{4.50}$$

where (x, y, z) are the current Cartesian coordinates and (X, Y, Z) are the initial

Cartesian coordinates.

Dirichlet boundary conditions. Dirichlet BCs are imposed as follows

- Bottom edge ($Y = -B$): $u_{1(x)} = \sqrt{2\alpha X}\cos\dfrac{-B}{\alpha} - X$
  $u_{2(y)} = \sqrt{2\alpha X}\sin\dfrac{-B}{\alpha} + B$
- Top edge ($Y = B$): $u_{1(x)} = \sqrt{2\alpha X}\cos\dfrac{Y}{\alpha} - X$
  $u_{2(y)} = \sqrt{2\alpha X}\sin\dfrac{Y}{\alpha} - B$
- Left-hand edge ($x = A_1$): $u_{1(x)} = \sqrt{2\alpha A_1}\cos\dfrac{Y}{\alpha} - A_1$
  $u_{2(y)} = \sqrt{2\alpha A_1}\sin\dfrac{Y}{\alpha} - Y$
- Right-hand edge ($x = A_2$): $u_{1(x)} = \sqrt{2\alpha A_2}\cos\dfrac{Y}{\alpha} - A_2$
  $u_{2(y)} = \sqrt{2\alpha A_2}\sin\dfrac{Y}{\alpha} - Y$

The deformation gradient $\mathbf{F}$ for this problem is

$$\mathbf{F} = \begin{bmatrix} f'(X) & 0 & 0 \\ 0 & f(X)\,g'(Y) & 0 \\ 0 & 0 & 1 \end{bmatrix} \tag{4.51}$$

where $f(X), g(Y), f'(X)$ and $g'(Y)$ are

$$f(X) = \sqrt{2\alpha X}, \quad f'(X) = \frac{\sqrt{2\alpha}}{2\sqrt{X}}, \quad g(Y) = \frac{1}{\alpha}Y, \quad g'(Y) = \frac{1}{\alpha} \tag{4.52}$$

The strain energy density of the neo-Hookean model is

$$\mathcal{W} = \frac{1}{2}\mu(I_1 - 3) + \frac{1}{2}\lambda(\ln J)^2 - \mu \ln J = \frac{1}{2}\mu(I_1 - 3) \tag{4.53}$$

where the Jacobian $J = \sqrt{I_3} = 1$ and $I_1 = (f'(X))^2 + \{f(X)\,g'(Y)\}^2 + 1$.

Hence, the exact strain energy can be computed as (see Appendix D.4)

$$W = \int_2^3 \int_{-2}^2 \left\{ \mu \frac{(0.9 - 2X)^2}{3.6X} \right\} \mathrm{d}V \tag{4.54}$$

and finally strain energy is $W = \int_2^3 \int_{-2}^2 \mathcal{W} \mathrm{d}Y \mathrm{d}X \approx 4.485618$ with following parameters: (1) for Dirichlet BCs: $\alpha = 0.9$, $A_1 = 2$, $A_2 = 3$ and $B = 2$, (2) mesh distortion: the distortion factors $\alpha_{\text{distorted}} = 0.1$, 0.2, 0.3, 0.4 and 0.45, (3) material parameters: shear modulus $\mu = 0.6$ and bulk modulus $\kappa = 1.95$ ($E \approx 1.6326$, $\nu \approx 0.3605$).

Figs. 4.12 and 4.13 show the initial and current configurations of the bending block with different distortion factors. When the distortion factor $\alpha_{\text{distorted}}$ is close to 0.5, given meshes become severely distorted. In this test, only Dirichlet boundary conditions are imposed which means that applied external forces vanish and no body force acts on the domain. Following Figs. 4.14 and 4.15 illustrate the strain energy convergence for regular and distorted meshes obtained by the classical FEM and edge-wise and node-wise smoothed FEM. The x-direction and y-direction denote the logarithm of the total number of degrees of freedom and the logarithm of $W^{\text{Numerical}}/W^{\text{Analytical}}$, respectively. With regular meshes, FEM shows better performance than ES-FEM and NS-FEM, which is similar to the result of the "Not-so-simple" shear deformation with non-homogeneous Dirichlet boundary conditions problem; however, when meshes are highly distorted, S-FEM provides stable and accurate results as well as faster convergence than FEM. Interestingly ES-FEM is insensitive to heavily distorted meshes while NS-FEM avoids the locking issues (see previous section 4.3.3). Note that the black dashed-line is the analytical solution for the bending problem computed by Eq. (4.54). (see also Appendix D.4)

Detailed values of the relative error in strain energy are given in Tables 4.10, 4.11, 4.12, 4.13, 4.14 and 4.15. The relative errors of S-FEM are much less than those

of FEM: errors for ES-FEM are about -1.0% to -1.9% and those of NS-FEM are around -1.5% to -3.5% with finer (2×32 and 4×32 elements) and severely distorted meshes ($\alpha_{\text{distorted}} = 0.45$) whereas errors of FEM are approximately -0.7% to 260%. This indicates that S-FEM models, ES-FEM in particular, can effectively alleviate the mesh distortion sensitivity in large deformations.

4.4 Summary

In this chapter, the behaviour of two strain smoothing approaches was compared, edge- and node-based for nearly-incompressible (Poisson's ratio is up to 0.49997) finite elasticity, and examined the effect of mesh distortion on accuracy. The conclusions, for the selected finite elasticity problems which are solved as follows:

- Deformation gradient smoothing permits to reproduce homogeneous deformations to machine precision;
- All smoothed elements perform much better than standard linear finite elements, which suffer severely from volumetric locking;
- The gold-standard, MINI element, performs at least as well as smoothing approaches for non-distorted meshes;
- Node-based smoothing is the most appropriate smoothing technique against volumetric locking;
- Edge-based smoothing is superior to node-based smoothing when dealing with distorted meshes.

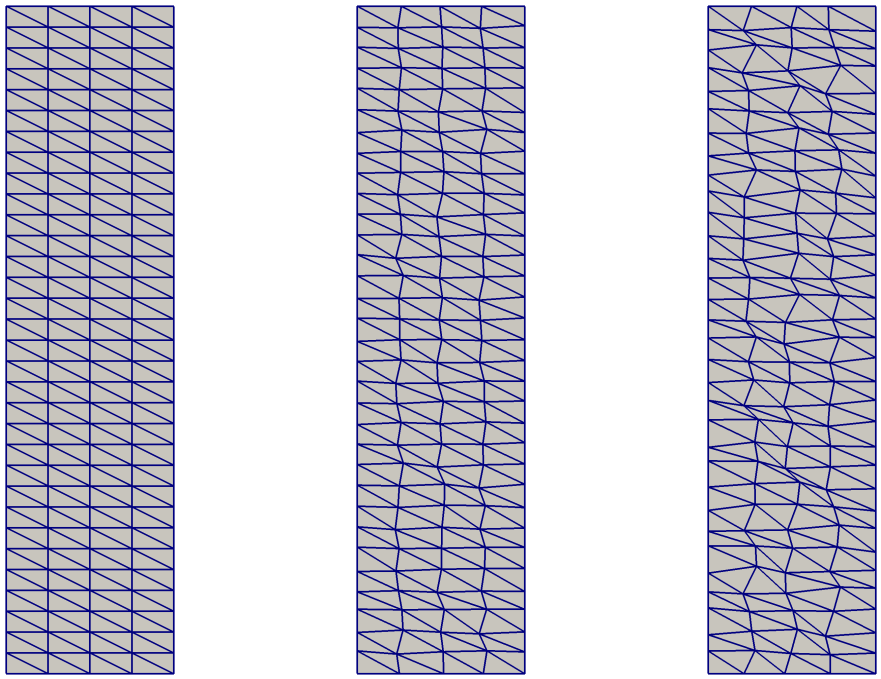

(a) Regular mesh (b) $\alpha_{\text{distorted}} = 0.1$ (c) $\alpha_{\text{distorted}} = 0.2$

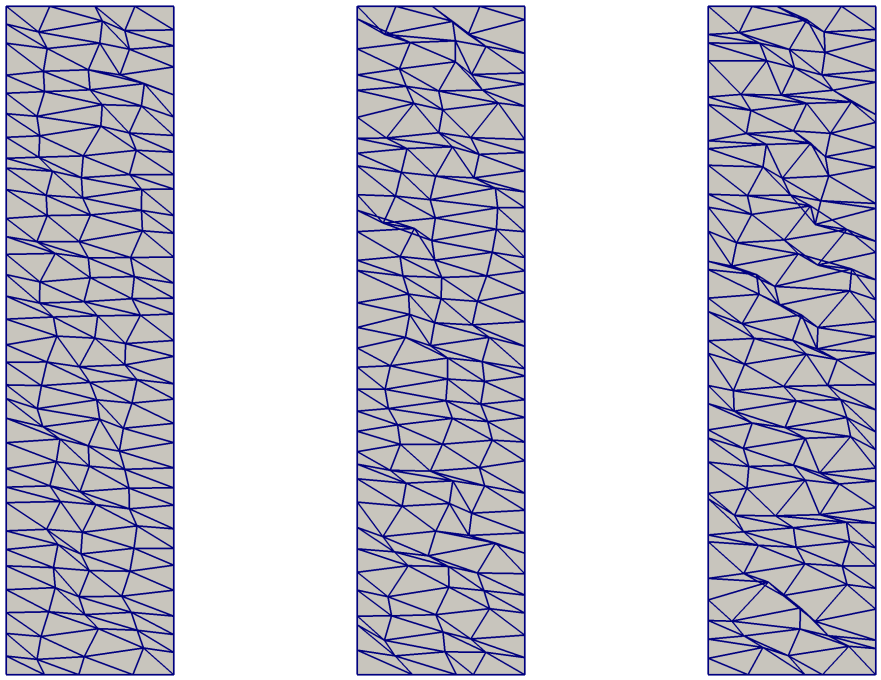

(d) $\alpha_{\text{distorted}} = 0.3$ (e) $\alpha_{\text{distorted}} = 0.4$ (f) $\alpha_{\text{distorted}} = 0.45$

Figure 4.12: Initial shapes of the rectangle (4×32 elements) with different distortion factors: (a) Regular mesh, (b) distorted mesh $\alpha_{\text{distorted}} = 0.1$, (c) distorted mesh $\alpha_{\text{distorted}} = 0.2$, (d) distorted mesh $\alpha_{\text{distorted}} = 0.3$, (e) distorted mesh $\alpha_{\text{distorted}} = 0.4$, (f) distorted mesh $\alpha_{\text{distorted}} = 0.45$

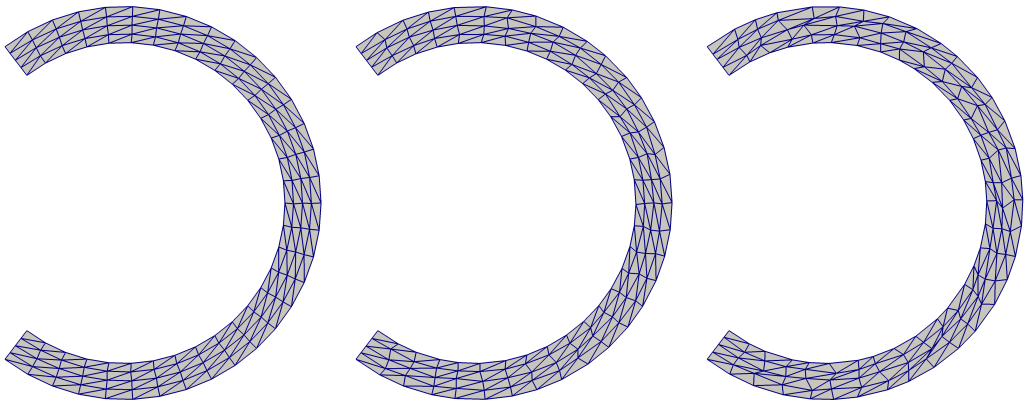

(a) Regular mesh (b) $\alpha_{\text{distorted}} = 0.1$ (c) $\alpha_{\text{distorted}} = 0.2$

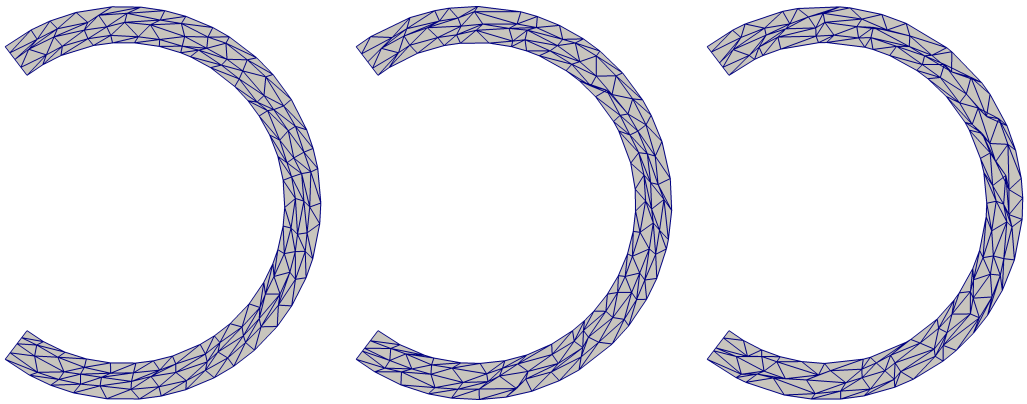

(d) $\alpha_{\text{distorted}} = 0.3$ (e) $\alpha_{\text{distorted}} = 0.4$ (f) $\alpha_{\text{distorted}} = 0.45$

Figure 4.13: Deformed shapes of the rectangle (4×32 elements) with different distortion factors: (a) Regular mesh, (b) distorted mesh $\alpha_{\text{distorted}} = 0.1$, (c) distorted mesh $\alpha_{\text{distorted}} = 0.2$, (d) distorted mesh $\alpha_{\text{distorted}} = 0.3$, (e) distorted mesh $\alpha_{\text{distorted}} = 0.4$, (f) distorted mesh $\alpha_{\text{distorted}} = 0.45$

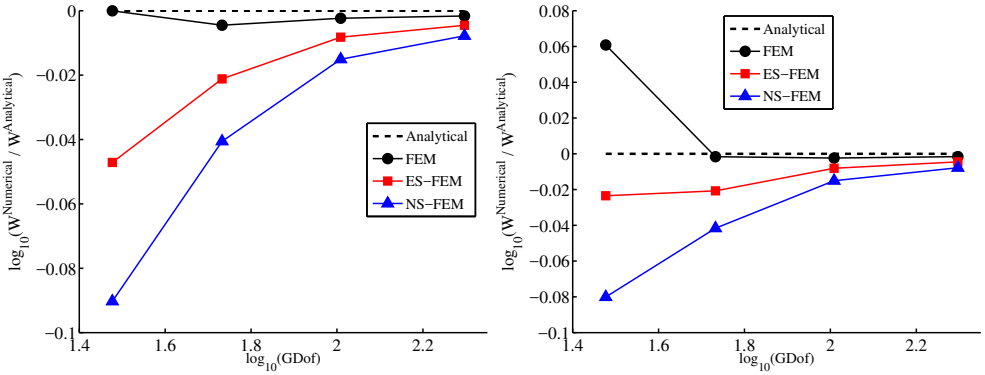

(a) Regular mesh

(b) $\alpha_{\text{distorted}} = 0.1$

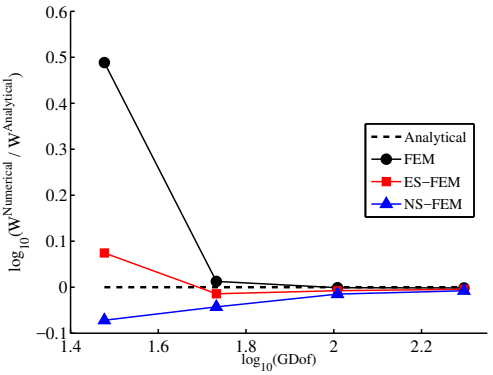

(c) $\alpha_{\text{distorted}} = 0.2$

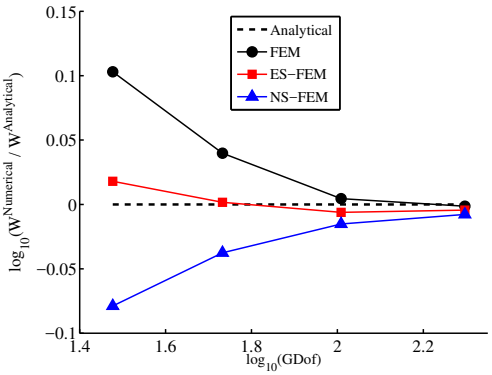

(d) $\alpha_{\text{distorted}} = 0.3$

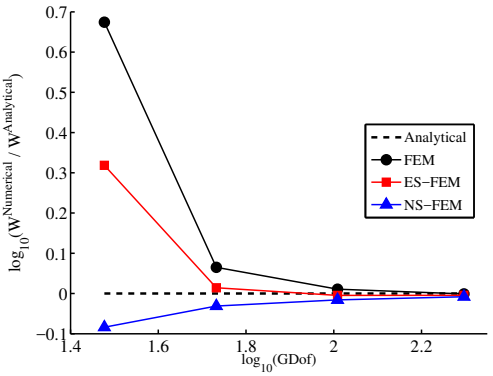

(e) $\alpha_{\text{distorted}} = 0.4$

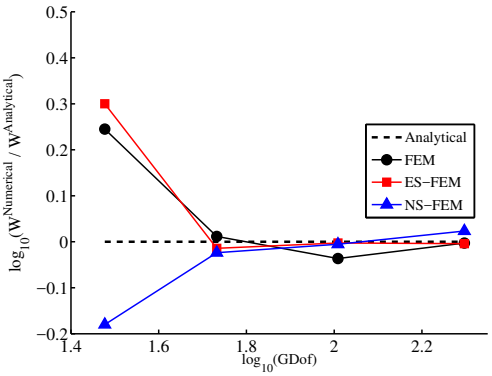

(f) $\alpha_{\text{distorted}} = 0.45$

Figure 4.14: The strain energy convergence for the bending problem with two elements in the x-direction (FEM, ES-FEM and NS-FEM): (a) Regular mesh, (b) $\alpha_{\text{distorted}} = 0.1$, (c) $\alpha_{\text{distorted}} = 0.2$, (d) $\alpha_{\text{distorted}} = 0.3$, (e) $\alpha_{\text{distorted}} = 0.4$, (f) $\alpha_{\text{distorted}} = 0.45$

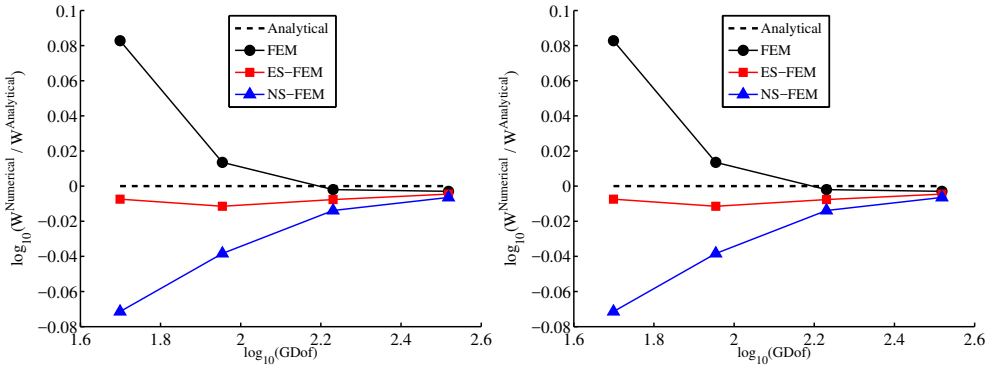

(a) Regular mesh (b) $\alpha_{\text{distorted}} = 0.1$

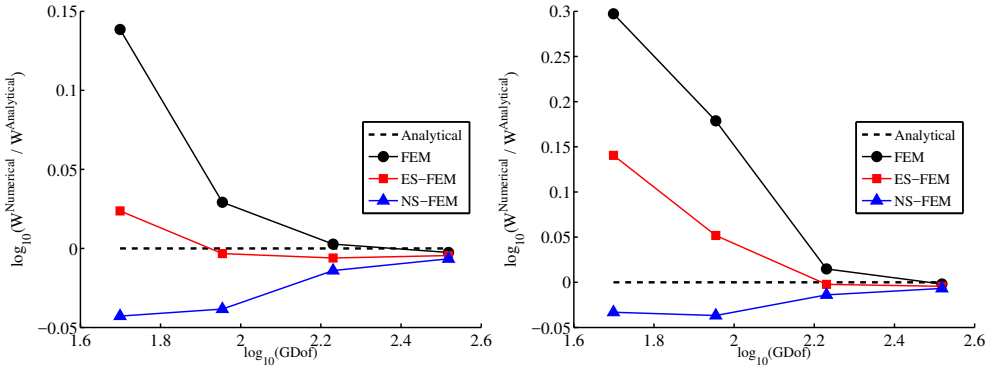

(c) $\alpha_{\text{distorted}} = 0.2$ (d) $\alpha_{\text{distorted}} = 0.3$

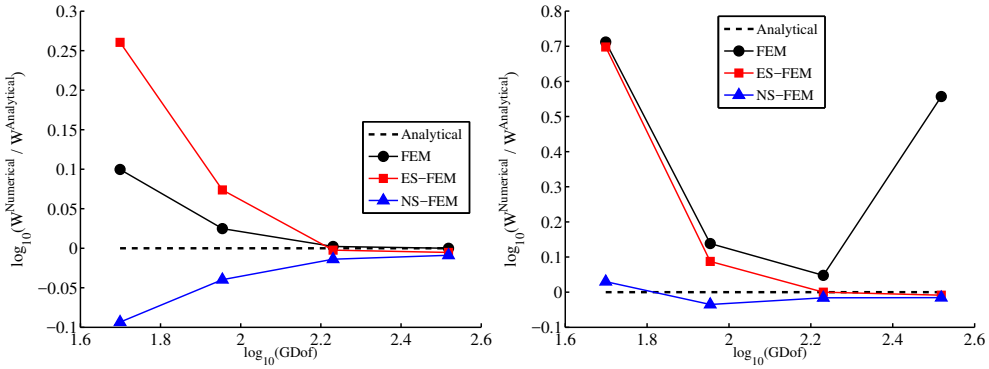

(e) $\alpha_{\text{distorted}} = 0.4$ (f) $\alpha_{\text{distorted}} = 0.45$

Figure 4.15: The strain energy convergence for the bending problem with four elements in the x-direction (FEM, ES-FEM and NS-FEM): (a) Regular mesh, (b) distorted mesh $\alpha_{\text{distorted}} = 0.1$, (c) distorted mesh $\alpha_{\text{distorted}} = 0.2$, (d) distorted mesh $\alpha_{\text{distorted}} = 0.3$, (e) distorted mesh $\alpha_{\text{distorted}} = 0.4$, (f) distorted mesh $\alpha_{\text{distorted}} = 0.45$

Table 4.10: Strain energy relative error for the rectangle bending example (FEM, ES-FEM and NS-FEM) with regular meshes

	Regular mesh		
	FEM	ES-FEM	NS-FEM
2×4	-0.0104	-10.2873	-18.7712
2×8	-1.0311	-4.7602	-8.9208
2×16	-0.5370	-1.8747	-3.4160
2×32	-0.3738	-1.0366	-1.7789
4×4	-0.3003	-10.4365	-17.4487
4×8	-1.3384	-4.8010	-8.6421
4×16	-0.8566	-1.8911	-3.1376
4×32	-0.6991	-1.0480	-1.4738

Strain energy relative error is given by:
$$\left(\frac{W^{\text{Numerical}} - W^{\text{Analytical}}}{W^{\text{Analytical}}}\right) \times 100\%.$$

Table 4.11: Strain energy relative error for the rectangle bending example (FEM, ES-FEM and NS-FEM) with distorted meshes ($\alpha_{\text{distorted}} = 0.1$)

	Distorted mesh $\alpha_{\text{distorted}} = 0.1$		
	FEM	ES-FEM	NS-FEM
2×4	15.0394	-5.2592	-16.8430
2×8	-0.3799	-4.6609	-9.1403
2×16	-0.5493	-1.8473	-3.4044
2×32	-0.3704	-1.0339	-1.7803
4×4	20.9957	-1.6956	-15.1659
4×8	3.1608	-2.6057	-8.4482
4×16	-0.4581	-1.7470	-3.1419
4×32	-0.6773	-1.0406	-1.4745

Strain energy relative error is given by:
$$\left(\frac{W^{\text{Numerical}} - W^{\text{Analytical}}}{W^{\text{Analytical}}}\right) \times 100\%.$$

Table 4.12: Strain energy relative error for the rectangle bending example (FEM, ES-FEM and NS-FEM) with regular meshes ($\alpha_{\text{distorted}} = 0.2$)

	Distorted mesh $\alpha_{\text{distorted}} = 0.2$		
	FEM	ES-FEM	NS-FEM
2×4	207.8773	18.6808	-15.2692
2×8	2.9302	-3.2316	-9.3727
2×16	-0.2530	-1.7188	-3.4011
2×32	-0.3814	-1.0355	-1.7894
4×4	37.5691	5.6167	-9.3829
4×8	6.9526	-0.7515	-8.4558
4×16	0.6311	-1.3835	-3.1703
4×32	-0.5890	-1.0317	-1.4972

Strain energy relative error is given by:
$$\left(\frac{W^{\text{Numerical}} - W^{\text{Analytical}}}{W^{\text{Analytical}}}\right) \times 100\%.$$

Table 4.13: Strain energy relative error for the rectangle bending example (FEM, ES-FEM and NS-FEM) with regular meshes ($\alpha_{\text{distorted}} = 0.3$)

	Distorted mesh $\alpha_{\text{distorted}} = 0.3$		
	FEM	ES-FEM	NS-FEM
2×4	26.7563	4.2299	-16.6087
2×8	9.5888	0.3820	-8.2951
2×16	1.0435	-1.4042	-3.4437
2×32	-0.3210	-1.0064	-1.7800
4×4	98.2786	38.2155	-7.3456
4×8	50.9083	12.6831	-8.1246
4×16	3.4588	-0.5151	-3.1546
4×32	-0.4390	-1.0076	-1.5394

Strain energy relative error is given by:
$$\left(\frac{W_{\text{Numerical}} - W_{\text{Analytical}}}{W_{\text{Analytical}}}\right) \times 100\%.$$

Table 4.14: Strain energy relative error for the rectangle bending example (FEM, ES-FEM and NS-FEM) with regular meshes ($\alpha_{\text{distorted}} = 0.4$)

	Distorted mesh $\alpha_{\text{distorted}} = 0.4$		
	FEM	ES-FEM	NS-FEM
2×4	372.4084	108.2842	-17.5341
2×8	16.1777	3.3278	-6.9028
2×16	2.5121	-1.0810	-3.5667
2×32	-0.2491	-1.0212	-1.8358
4×4	25.7889	82.1832	-19.3577
4×8	5.8777	18.5201	-8.7415
4×16	0.5084	-0.5468	-3.1434
4×32	-100.00	-1.2111	-2.0218

Strain energy relative error is given by:
$$\left(\frac{W^{\text{Numerical}} - W^{\text{Analytical}}}{W^{\text{Analytical}}}\right) \times 100\%.$$

Table 4.15: Strain energy relative error for the rectangle bending example (FEM, ES-FEM and NS-FEM) with regular meshes ($\alpha_{\text{distorted}} = 0.45$)

	Distorted mesh $\alpha_{\text{distorted}} = 0.45$		
	FEM	ES-FEM	NS-FEM
2×4	75.7918	99.6165	-33.9235
2×8	2.7048	-3.1995	-5.3375
2×16	-8.0411	-0.6074	-1.2245
2×32	-0.6437	-0.9329	5.5170
4×4	415.3821	398.7013	7.1348
4×8	37.5263	22.3123	-7.7612
4×16	11.6704	-0.0267	-3.6126
4×32	260.4544	-1.9604	-3.5447

Strain energy relative error is given by:
$$\left(\frac{W^{\text{Numerical}} - W^{\text{Analytical}}}{W^{\text{Analytical}}}\right) \times 100\%.$$

5 Smoothed finite element method enriched with bubble functions

Since S-FEM was introduced by Liu et al. [82], different S-FEM (CS-FEM, ES-FEM, NS-FEM and FS-FEM) have been developed and used in a variety of fields. Particularly ES-FEM is a popular S-FEM model because of its interesting features: 1) ES-FEM is insensitive to severely-distorted meshes, 2) the stiffness matrix of ES-FEM is softer than FEM (overcomes the overestimation of stiffness), 3) it produces more accurate solutions and faster convergence rate and 4) it is easy to implement into existing FEM codes. ES-FEM does not overcome locking so that an improved ES-FEM was introduced [86]: the domain-based selective ES/NS-FEM. Recently domain-based smoothing was studied by Jiang et al. [67, 68]. The domain-based S-FEM showed the alleviation of locking; however, discretized equations required an additional treatment for each of the edge-based, node-based and face-based approaches.

However Nguyen-Xuan and Liu [115] reported that neither the domain-based selective ES/NS-FEM nor NS-FEM fully prevent locking. They introduced the mixed displacement-pressure formulation in the framework of edge-based strain smoothing using cubic bubble functions: so-called bES-FEM. The mathematical properties of the proposed methods, bES-FEM in 2D and bFS-FEM in 3D, were

provided by Ong et al. [126, 127][1]. Furthermore, bES-FEM was successfully extended to the variational multi-scale approach [156].

In order to develop non-locking, gradient strain smoothing that is insensitive to mesh distortion, this Chapter introduces the bubble-enhanced edge-based (2D) and face-based (3D) strain smoothing approach for incompressible large deformations. A transformation of "Cubic" bubble functions and mathematical formulations for the proposed strain smoothing approach are presented in section 5.1. Following this, the smoothed mixed formulation for linear elasticity is given in section 5.2.

5.1 "Cubic" bubble functions

The bubble function supplements an additional displacement field at a node placed at the centroid of a triangle T. The MINI elements for Navier-Stoke equations have the velocity fields and piecewise linear functions are used for the pressure. This element is very effective for mixed formulation where both displacements and pressure are unknowns [2, 28]. In contrast to the MINI element, ES-FEM constructs a displacement-based formulation, ES-FEM with a bubble function has only a linear displacement field as unknown which has value one at the centroid of triangle T and the pressure vanishes at the edges of triangle T. As shown in Fig. 5.1, an interior node is located at the geometric center with an additional displacement field associated with the cubic bubble.

[1]Detail of Reference [127] is: T.H. Ong et al., Inf-suf stable bES-FEM method for nearly incompressible elasticity,2013:URL http://arxiv.org/pdf/1305.0466.pdf

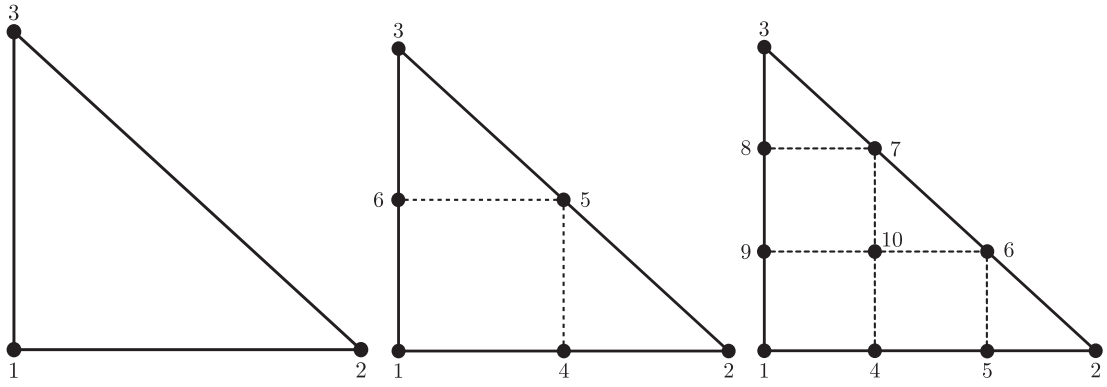

(a) Linear 3-noded element (b) Quadratic 6-noded element (c) Cubic 10-noded element

Figure 5.1: Lagrange triangular elements: (a) linear Lagrange element, (b) quadratic Lagrange element and (c) cubic Lagrange element

In this work the cubic bubble function introduced in Reference [59] is used. Since the first three basis functions are not zero at the centroid $(1/3, 1/3)$, a basis function $\tilde{\Psi}(\xi,\eta) = \left[\begin{array}{cccc} 1-\xi-\eta & \xi & \eta & 27\xi\eta(1-\xi-\eta) \end{array}\right]^{\mathrm{T}}$ is necessarily required to transform the form of $\Psi(\xi,\eta)$ given as

$$\begin{aligned} \Psi(\xi,\eta)^{\mathrm{T}} &= \tilde{\Psi}(\xi,\eta)^{\mathrm{T}} B_S^{-1} \\ &= \left[\begin{array}{cccc} 1-\xi-\eta & \xi & \eta & 27\xi\eta(1-\xi-\eta) \end{array}\right] \left[\begin{array}{cccc} 1 & 0 & 0 & 0 \\ 0 & 1 & 0 & 0 \\ 0 & 0 & 1 & 0 \\ -\frac{1}{3} & -\frac{1}{3} & -\frac{1}{3} & 1 \end{array}\right] \end{aligned} \tag{5.1}$$

and therefore the basis functions are

$$\Psi(\xi,\eta) = \left[\begin{array}{c} (1-\xi-\eta) - 9\xi\eta(1-\xi-\eta) \\ \xi - 9\xi\eta(1-\xi-\eta) \\ \eta - 9\xi\eta(1-\xi-\eta) \\ 27\xi\eta(1-\xi-\eta) \end{array}\right] \tag{5.2}$$

Fig. 5.2 represents the basis functions and the cubic bubble function located at the centroid of a right 45° three-node triangular element. The bubble function

has the following properties

$$\begin{cases} \Psi_b > 0 & \text{in } \Omega_e \\ \Psi_b = 0 & \text{on } \Gamma_e \\ \Psi_b = 1 & \text{at internal nodes} \end{cases} \tag{5.3}$$

Hence the assumed displacement $\mathbf{u}^{\mathrm{h}}$ on Ω_e can be expressed as in Reference [115]

$$\mathbf{u}^{\mathrm{h}}(\mathbf{x})\big|_{\Omega_e} = \sum_{i=1}^{3} \begin{bmatrix} \Psi_i(\mathbf{x}) & 0 \\ 0 & \Psi_i(\mathbf{x}) \end{bmatrix} \mathbf{d}_i + \begin{bmatrix} \Psi_b(\mathbf{x}) & 0 \\ 0 & \Psi_b(\mathbf{x}) \end{bmatrix} \mathbf{d}_b \tag{5.4}$$

where Ψ_i, $i = \{1, 2, 3\}$ are the basis functions, Ψ_b is the cubic bubble function, $\mathbf{d}_i = [u_i, v_i]^{\mathrm{T}}$ are unknown displacements at each node and $\mathbf{d}_b = [u_b, v_b]^{\mathrm{T}}$ are the unknown displacements at the centroid of triangle T.

5.2 Smoothed mixed finite element approximation in linear elasticity

A 2D linear elastic solid problem in a domain Ω in $\mathbb{R}^2$ with a Lipschitz boundary $\Gamma = \partial\Omega$ is considered. From governing equation (Eq. (2.7)), the mixed formulation introducing pressure p as an additional variable is given by

$$\begin{aligned} -\mathrm{div}\,\boldsymbol{\sigma} &= \mathbf{f} \quad \text{in}\,\Omega \\ \mathrm{div}\,\mathbf{u} - \frac{p}{\lambda} &= 0 \quad \text{in}\,\Omega \end{aligned} \tag{5.5}$$

Note that the mixed displacement-pressure form (Eq. (5.5)) equivalently leads to the penalised Stoke equation. Defining a displacement field $\mathbf{u} \in V = [\mathbb{H}^1(\Omega)]^2$ and a pressure $p \in L_0^2(\Omega) = \{q \in L^2(\Omega), \int_\Omega q \mathrm{d}\Omega = 0\}$, the mixed variational formulation consists $\mathbf{u} \in \mathbf{v}$ and $p \in L^2(\Omega)$ such that for all $\mathbf{v} \in V_0$ and all

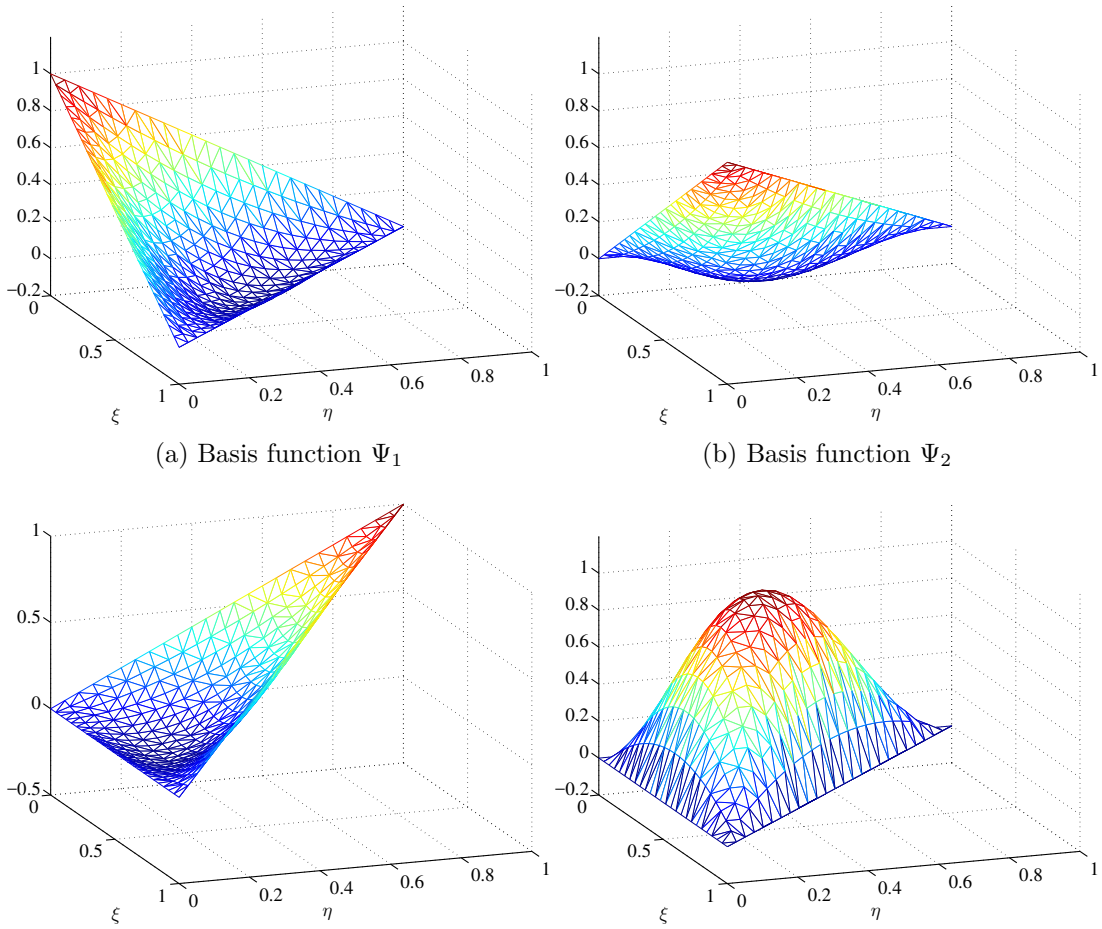

(a) Basis function Ψ_1

(b) Basis function Ψ_2

(c) Basis function Ψ_3

(d) Cubic bubble function Ψ_b

Figure 5.2: Renewed basis functions and the cubic bubble function associated the centroid of a right 45° three-node triangular (T3) element

$q \in L_0^2(\Omega)$

$$\begin{aligned} a(\mathbf{u},\mathbf{v}) + b(\mathbf{v},p) &= (\mathbf{f},\mathbf{v}) \\ b(\mathbf{u},q) - \frac{1}{\lambda} c(p,q) &= 0 \end{aligned} \tag{5.6}$$

where pressure p is required to be square-integrable (L^2-function) defining a space $L_0^2(\Omega)$ to be the subspace of L^2-function with the zero.

The bilinear forms of Eq. (5.6) can be expressed as:

$$\begin{aligned} a(\mathbf{u},\mathbf{v}) &= 2\mu \int_\Omega \boldsymbol{\varepsilon}^{\mathrm{T}}(\mathbf{v})\,\mathbb{C}\boldsymbol{\varepsilon}(\mathbf{u})\,\mathrm{d}\Omega \\ b(\mathbf{v},p) &= \int_\Omega p\nabla\mathbf{v}\mathrm{d}\Omega \\ c(p,q) &= \int_\Omega pq\mathrm{d}\Omega \\ (\mathbf{f},\mathbf{v}) &= \int_\Omega \mathbf{v}^{\mathrm{T}}\mathbf{f}\mathrm{d}\Omega \end{aligned} \tag{5.7}$$

Similarly, the mixed variational problem in the framework of S-FEM can be written. Finding $\mathbf{u}^{\mathrm{h}} \in V^{\mathrm{h}} = \left[\mathbb{H}^1(\Omega)\right]^2$ and $p^{\mathrm{h}} \in L_0^2(\Omega) = \left\{\tilde{q}^{\mathrm{h}} \in L^2(\Omega), \int_\Omega \tilde{q}^{\mathrm{h}}\mathrm{d}\Omega = 0\right\}$ such that for all $\mathbf{v}^{\mathrm{h}} \in V_0^{\mathrm{h}}$ and $q^{\mathrm{h}} \in L_0^2(\Omega)$

$$\begin{aligned} \tilde{a}\left(\mathbf{u}^{\mathrm{h}},\mathbf{v}^{\mathrm{h}}\right) + \tilde{b}\left(\mathbf{v}^{\mathrm{h}},p^{\mathrm{h}}\right) &= \left(\mathbf{f},\mathbf{v}^{\mathrm{h}}\right) \\ \tilde{b}\left(\mathbf{u}^{\mathrm{h}},q^{\mathrm{h}}\right) - \frac{1}{\lambda}\tilde{c}\left(p^{\mathrm{h}},q^{\mathrm{h}}\right) &= 0 \end{aligned} \tag{5.8}$$

where the following definitions are made:

$$\begin{aligned} \tilde{a}\left(\mathbf{u}^{\mathrm{h}},\mathbf{v}^{\mathrm{h}}\right) &= 2\mu \int_\Omega \tilde{\boldsymbol{\varepsilon}}^{\mathrm{T}}\left(\mathbf{v}^{\mathrm{h}}\right)\mathbb{C}\tilde{\boldsymbol{\varepsilon}}(\mathbf{u})^{\mathrm{h}}\,\mathrm{d}\Omega \\ \tilde{b}\left(\mathbf{v}^{\mathrm{h}},p^{\mathrm{h}}\right) &= \int_\Omega p^{\mathrm{h}}\tilde{\nabla}\mathbf{v}^{\mathrm{h}}\mathrm{d}\Omega \\ \tilde{c}\left(p^{\mathrm{h}},q^{\mathrm{h}}\right) &= \int_\Omega p^{\mathrm{h}},q^{\mathrm{h}}\mathrm{d}\Omega \\ \left(\mathbf{f},\mathbf{v}^{\mathrm{h}}\right) &= \int_\Omega \left(\mathbf{v}^{\mathrm{h}}\right)^{\mathrm{T}}\mathbf{f}\mathrm{d}\Omega \end{aligned} \tag{5.9}$$

Finally the matrix form of the linear system for the enhanced S-FEM in linear elasticity can be defined as

$$\begin{bmatrix} \tilde{\mathbf{A}} & \tilde{\mathbf{B}}^{\mathrm{T}} \\ \tilde{\mathbf{B}} & -\frac{1}{\lambda}\tilde{\mathbf{C}} \end{bmatrix} \begin{bmatrix} \mathbf{u}^{\mathrm{h}} \\ p^{\mathrm{h}} \end{bmatrix} = \begin{bmatrix} \mathbf{f}^{\mathrm{h}} \\ 0 \end{bmatrix} \tag{5.10}$$

where matrices $\tilde{\mathbf{A}}$, $\tilde{\mathbf{B}}$ and $\tilde{\mathbf{C}}$ are associated with the smoothed bilinear forms (Eq. (5.10)) that are $\tilde{a}(\cdot,\cdot)$, $\tilde{b}(\cdot,\cdot)$ and $\tilde{c}(\cdot,\cdot)$ and $\mathbf{f}^{\mathrm{h}}$ are associated with the linear operator $(\mathbf{f},\cdot)$ in Eq. (5.10).

5.3 Numerical Results

Cook's membrane test for incompressibility with bulk moduli $\kappa = 10^5$, 10^6 and 10^7 is firstly considered. Second the (near-)incompressible problems of a plate with a circular hole inclusion at the center is considered. In this test, bulk modulus $\kappa = 10^7$, Poisson's ratio $\nu \approx 0.49999997$, is used for the conventional FEM, the MINI element using DOLFIN finite element software, ES-FEM, NS-FEM and the bubble-enriched ES-FEM. DOLFIN finite element software is used as a reference solution. Then a sharp V-notched square and punching problem with bulk modulus $\kappa = 10^5$, Poisson's ratio $\nu \approx 0.499997$ are considered. As a reference solution, the numerical solution of DOLFIN finite element software with a very fine mesh of DOFs, 34379, is used for those three examples.

For sensitivity to the distorted meshes in compressibility, a punching problem is firstly considered for the FEM, the MINI element, ES-FEM, NS-FEM and bES-FEM with bulk modulus $\kappa = 1.95$ ($\nu \approx 0.3605$) with regular and distorted meshes $\alpha_{\text{distorted}} = 0.1$ and 0.3. Simple torsion of a rectangular block is tested.

This problem is expressed in sections 2.2.6 and 5.2.4 of Reference [123]. Cylindrical coordinates and non-homogeneous Dirichlet boundary conditions are provided. A bending of a rectangular block is examined subsequently with heavily distorted meshes. Dirichlet boundary conditions are imposed in this test and these are introduced in section 4.3.6.

Lastly problems for the mesh distortion sensitivity in the incompressible limit are examined. A bevelled cantilever beam is tested with Poisson's ratio $\nu \approx 0.49999997$. Mesh distortion factors $\alpha_{\text{distorted}} = 0.1, 0.3$ are used for the classical FEM, the locking-free MINI element and S-FEM. DOLFIN with fine meshes is also used as the reference solution.

5.3.1 Incompressibility

Cook's membrane. In this example, the geometry of Cook's membrane and parameters are exactly the same as in section 4.3.5. However the bulk modulus used in this test is much larger: bulk moduli $\kappa = 10^5$, 10^6 and 10^7 are equivalent to Poisson's ratios $\nu \approx 0.499997$, $\nu \approx 0.4999997$ and $\nu \approx 0.49999997$. The number of elements in this section is 4×4, 8×8, 10×10, 16×16, 20×20, 32×32, 40×40 and 100×100 along on each side. DOLFIN [90, 91] based on a mixed finite element formulation on highly refined meshes (GDof $= 816,080,000$) is used as a reference solution.

The strain energy convergence for each technique is shown in Fig. 5.3. The x- and y-directions represent the logarithm of the total number of degrees of freedoms and the logarithm of the ratio of the numerical strain energy obtained the MINI element, standard T3 FEM and the smoothed FEM to the reference strain energy. As shown in Fig. 5.3, NS-FEM performs better than ES-FEM and FEM for large bulk moduli. However the bubble-enhanced ES-FEM produces much more accurate results and faster convergence rates than the NS-FEM. It is seen that the bubble function within ES-FEM effectively improves the quality of lower-order simplex T3 element in quasi-incompressible limit and avoids locking.

Relative errors in the strain energy for FEM, the MINI element, ES-FEM, NS-FEM and the bubble-enriched ES-FEM are given in Tables 5.1, 5.2 and 5.3. The relative errors of FEM and ES-FEM are around 50% with fine meshes, whereas the MINI, NS-FEM and bES-FEM are significantly more accurate. While the MINI element provides reliable results, a notable improvement of the bES-FEM is that its relative errors, around -0.05% for bulk moduli $\kappa = 10^5$, 10^6 and 10^7 with fine meshes which is about half those of NS-FEM, which are 0.13% with fine meshes. In other words, bubble enriched ES-FEM is much more accurate and provides faster convergence for nearly incompressible problems.

Fig. 5.4 shows the logarithm of L2 norm in displacements for this problem. L2 norm is computed by

$$\|\mathbf{e}\|_{\mathrm{u}} = \left(\int \left(\mathbf{u}^{*} - \mathbf{u}^{\mathrm{h}} \right)' \left(\mathbf{u}^{*} - \mathbf{u}^{\mathrm{h}} \right) \mathrm{d}\Omega \right)^{\frac{1}{2}} \tag{5.11}$$

where $\mathbf{u}^{*}$ is the reference solution and $\mathbf{u}^{\mathrm{h}}$ is the numerical solution.

Table 5.1: Strain energy relative error for Cook's membrane (FEM, ES-FEM, NS-FEM, bES-FEM and the MINI element) with bulk modulus $\kappa = 10^5$

Num. of elements	FEM	ES-FEM	NS-FEM	bES-FEM	MINI
4×4	-51.2287	-45.3871	4.5275	-2.3552	-2.4588
8×8	-49.1551	-45.6788	2.3876	-0.8061	-0.8439
10×10	-48.7447	-44.9870	1.7765	-0.6295	-0.6172
16×16	-48.1180	-40.6140	0.9097	-0.3952	-0.3333
20×20	-47.8706	-37.0928	0.6632	-0.3191	-0.2531
32×32	-47.2637	-27.7231	0.3576	-0.2010	-0.1452
40×40	-46.8459	-23.0906	0.2753	-0.1595	-0.1119
100×100	-42.7784	-21.8067	0.1256	-0.0506	-0.0302

Strain energy relative error is given by: $\left(\dfrac{W^{\mathrm{Numerical}} - W^{\mathrm{Reference}}}{W^{\mathrm{Reference}}} \right) \times 100\%$.

Table 5.2: Strain energy relative error for Cook's membrane (FEM, ES-FEM, NS-FEM, bES-FEM and the MINI element) with bulk modulus $\kappa = 10^6$

Num. of elements	FEM	ES-FEM	NS-FEM	bES-FEM	MINI
4×4	-51.2285	-48.1102	4.5461	-2.3552	-2.3686
8×8	-49.1968	-47.7943	2.4001	-0.8061	-0.8033
10×10	-48.8111	-47.6096	1.7771	-0.6295	-0.5904
16×16	-48.2921	-46.4490	0.9113	-0.3952	-0.3261
20×20	-48.1398	-44.9314	0.6649	-0.3191	-0.2505
32×32	-47.9235	-38.1638	0.3594	-0.2010	-0.1459
40×40	-47.8376	-33.4308	0.2771	-0.1595	-0.1126
100×100	-47.1735	-12.8090	0.1267	-0.0506	-0.0302

Strain energy relative error is given by: $\left(\frac{W^{\text{Numerical}} - W^{\text{Reference}}}{W^{\text{Reference}}}\right) \times 100\%$.

Table 5.3: Strain energy relative error for Cook's membrane (FEM, ES-FEM, NS-FEM, bES-FEM and the MINI element) with bulk modulus $\kappa = 10^7$

Num. of elements	FEM	ES-FEM	NS-FEM	bES-FEM	MINI
4×4	-51.2381	-48.1194	4.5757	-2.3552	-2.3582
8×8	-49.2009	-47.8888	2.3908	-0.8061	-0.7968
10×10	-48.8186	-47.8235	1.7787	-0.6295	-0.5852
16×16	-48.3098	-47.6483	0.9130	-0.3952	-0.3229
20×20	-48.1684	-47.4416	0.6661	-0.3191	-0.2482
32×32	-47.9952	-45.8184	0.3593	-0.2010	-0.1447
40×40	-47.9486	-43.7801	0.2770	-0.1595	-0.1118
100×100	-47.8181	-25.1310	0.1267	-0.0506	-0.0301

Strain energy relative error is given by: $\left(\frac{W^{\text{Numerical}} - W^{\text{Reference}}}{W^{\text{Reference}}}\right) \times 100\%$.

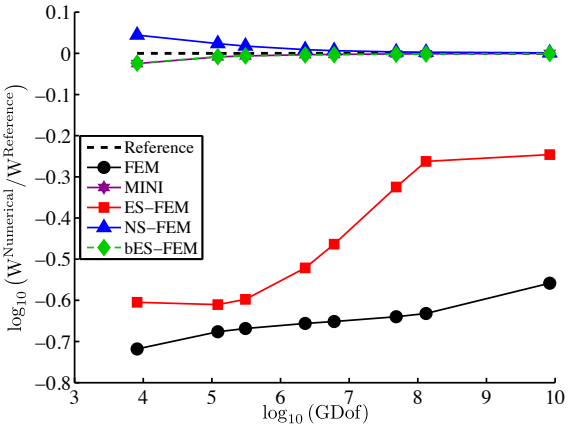

(a) Bulk modulus $\kappa = 10^5$

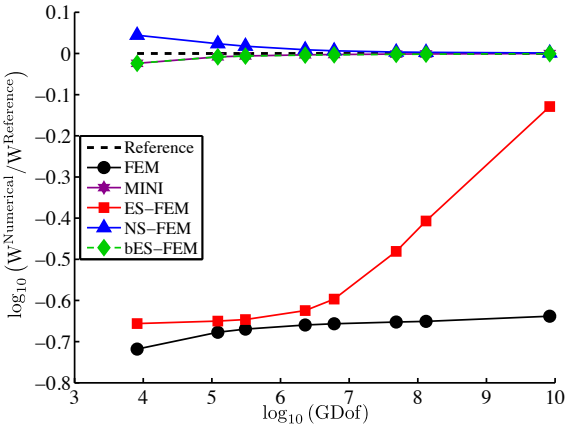

(b) Bulk modulus $\kappa = 10^6$

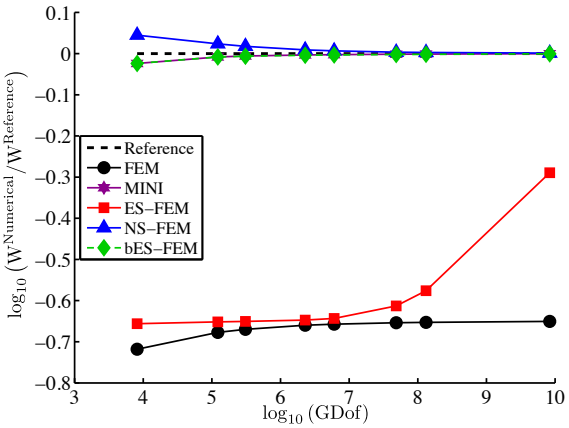

(c) Bulk modulus $\kappa = 10^7$

Figure 5.3: Strain energy convergence for Cook's membrane with bulk moduli $\kappa = 10^5$, $\kappa = 10^6$ and $\kappa = 10^7$: $\mathrm{W}^{\mathrm{Numerical}}$ is the numerical solution of FEM, the MINI and S-FEM and $\mathrm{W}^{\mathrm{Reference}}$ is the DOLFIN solution

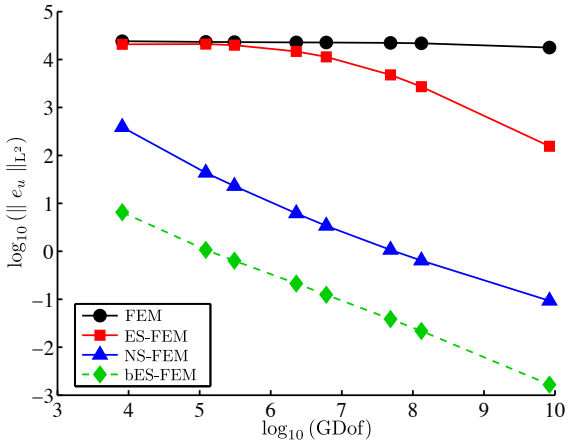

(a) Bulk modulus $\kappa = 10^5$

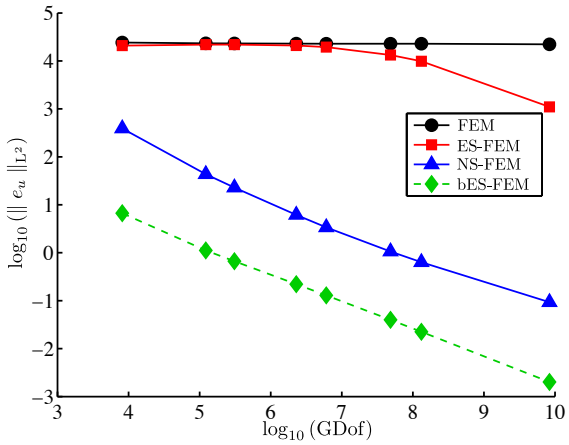

(b) Bulk modulus $\kappa = 10^6$

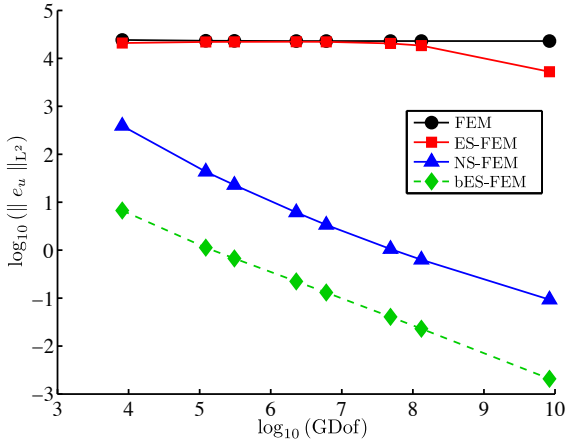

(c) Bulk modulus $\kappa = 10^7$

Figure 5.4: L2 norm in displacements for Cook's membrane with bulk moduli $\kappa = 10^5$, $\kappa = 10^6$ and $\kappa = 10^7$

Plate with a hole. A quasi-incompressible plate with a hole located at the centre for near-incompressibility is studied next. The geometry, boundary conditions and loading are shown in Fig. 5.5. Left-hand, right-hand and bottom edges are fixed (prescribed displacement boundary conditions are $u_i = 0.0$, $i \in 1, 2$) and the external forces ($P = -0.1$) act on the top edge. The radius of the inner circle is $R = 0.5$ and $L = 1.0$. Shear modulus $\mu = 0.6$ and bulk modulus $\kappa = 10^7$, so that Poisson's ratio is $\nu \approx 0.49999997$, are used for this test.

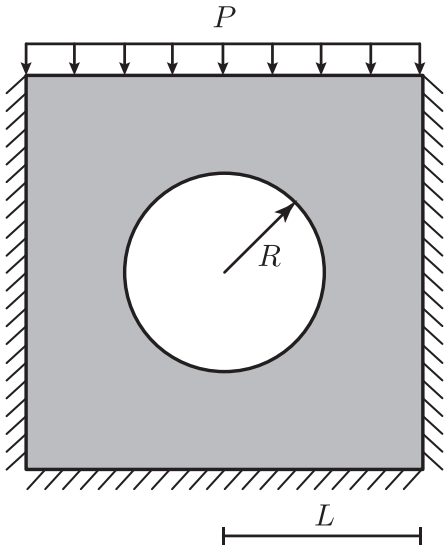

Figure 5.5: A plate with a circular inclusion: geometry, boundary conditions and external forces

Fig. 5.6 shows the deformed shapes with their displacements and Fig. 5.7 shows strains. It is seen that the NS-FEM and bubble-enhanced ES-FEM are immune to the locking problem in quasi-incompressible media.

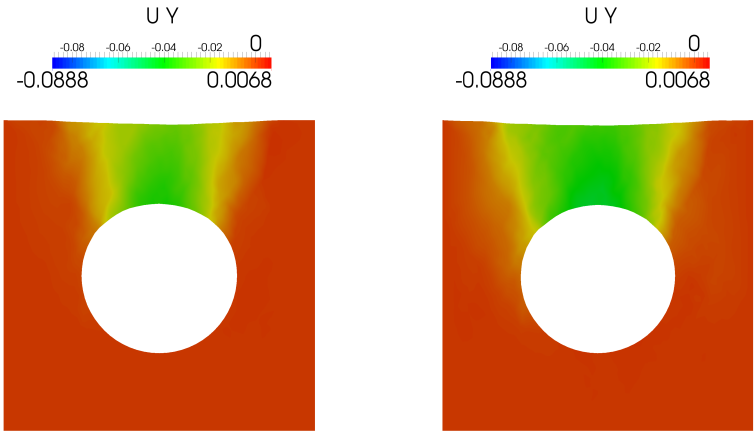

(a) the standard FEM

(b) ES-FEM

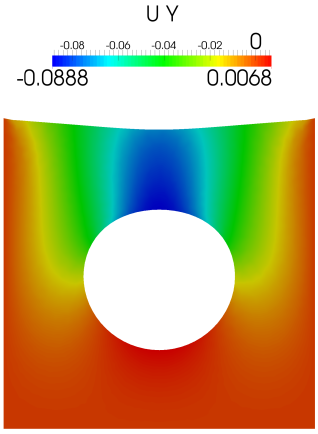

(c) NS-FEM

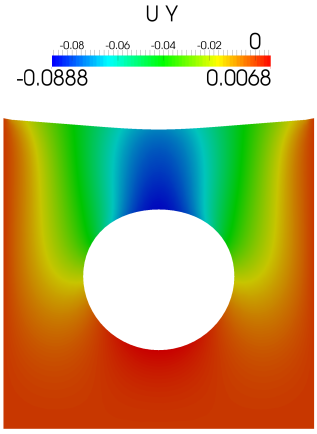

(d) bES-FEM

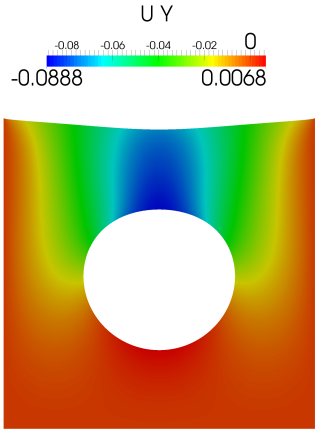

(e) MINI

Figure 5.6: Deformed shapes and displacements (u_y) of Plate with a hole: Bulk modulus $\kappa = 10^7$ and DOFs 3648

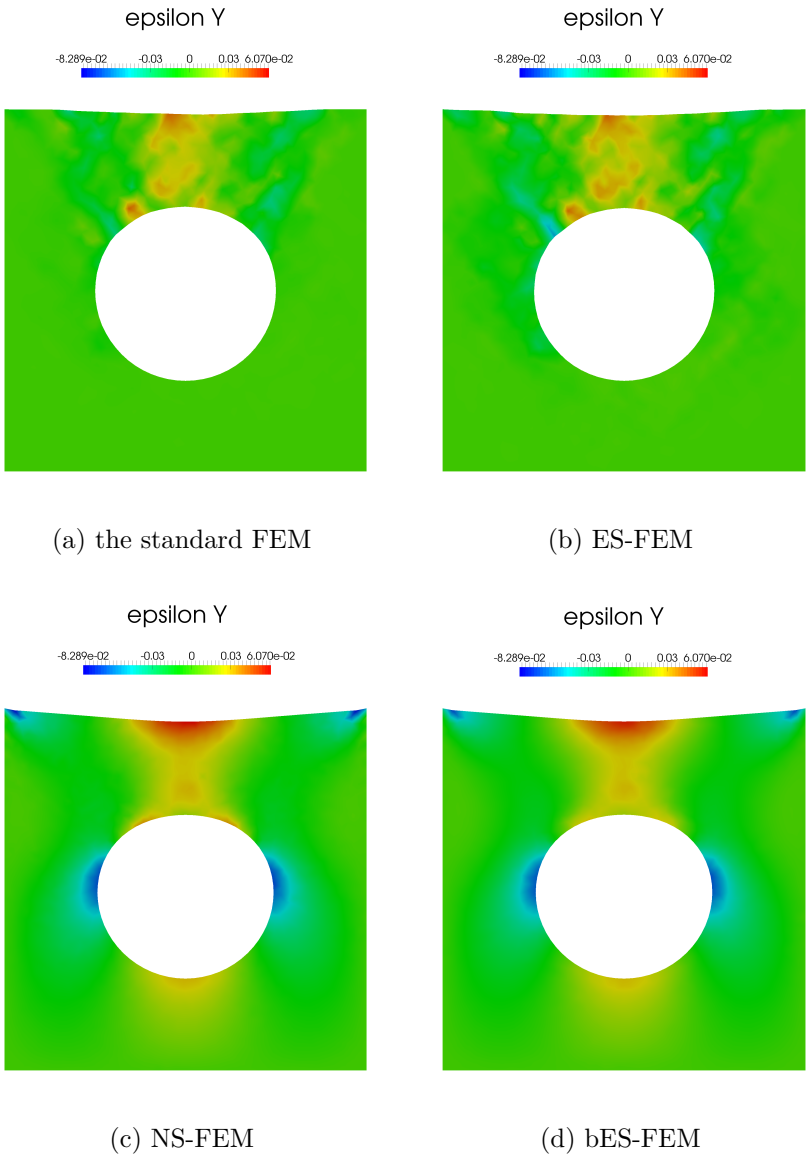

(a) the standard FEM (b) ES-FEM

(c) NS-FEM (d) bES-FEM

Figure 5.7: Green strains (ε_y) of Plate with a hole: Bulk modulus $\kappa = 10^7$ and DOFs 3648

Fig. 5.8 depicts the convergence of the strain energy. The x-direction denotes the logarithm of the total number of degrees of freedom, which DOFs are 28, 72, 968 and 3648, and y-direction corresponds to the logarithm of ratio of the numerical to the reference strain energy. Fig. 5.9 illustrates the logarithm of the relative

error in strain energy. Relative error of strain energy W^{error} is defined as

$$W^{\text{error}} = \left(\frac{W^{\text{Numerical}} - W^{\text{Reference}}}{W^{\text{Reference}}} \right) \times 100 \tag{5.12}$$

From Figs. 5.8 and 5.9, while NS-FEM effectively cure locking, the bubble-enhanced ES-FEM and the MINI element provide better accurate and faster convergence than FEM and ES-FEM.

ES-FEM provides slightly better accurate results than FEM, however it cannot fully avoid locking. On the other hand, NS-FEM, bES-FEM and the MINI element handles incompressible material efficiently as given in Table 5.4. The relative error for bES-FEM is almost 17% of that of the MINI element which is a notable improvement compare to Cook's membrane problem.

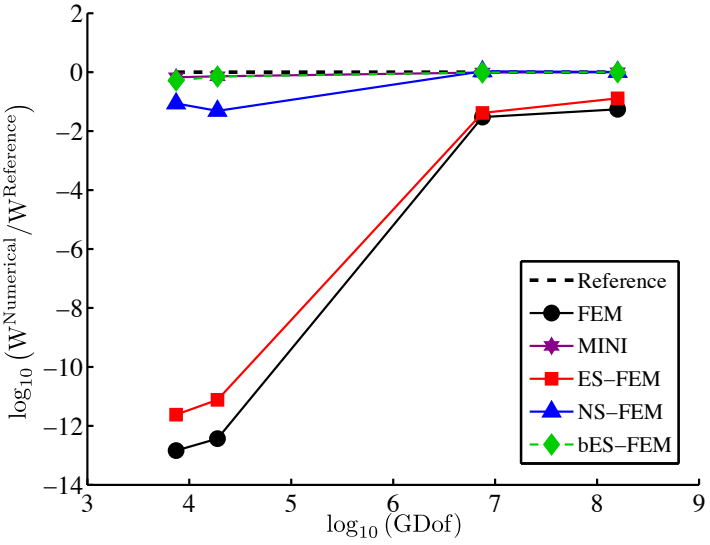

Figure 5.8: Convergence in strain energy for plate of FEM, the MINI element, ES-FEM, NS-FEM and bES-FEM: Reference solution is obtained by DOLFIN with very fine meshes of the MINI (DOFs: 682932)

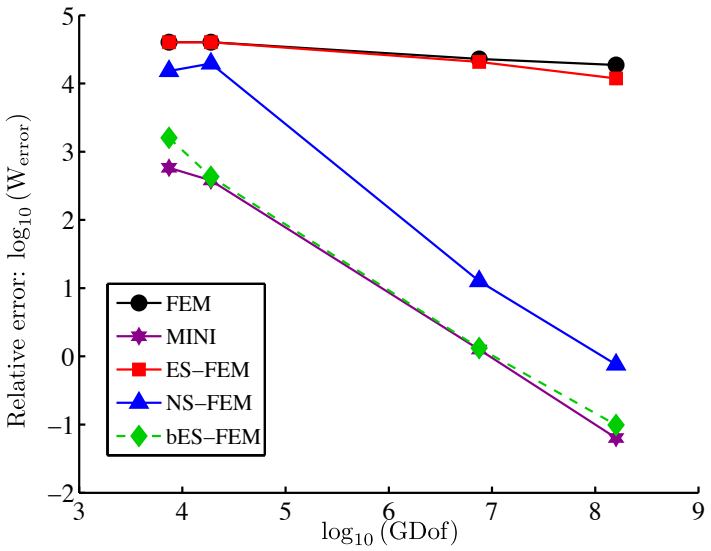

Figure 5.9: The logarithmic relative error in strain energy of FEM, the MINI, ES-FEM, NS-FEM and bES-FEM

Fig. 5.10 shows the L2 norm for this problem. The y-axis denotes the logarithm of L2 norm in displacements for the FEM, ES-FEM, NS-FEM and bES-FEM. The MINI element (DOFs: 682932) is used as the reference solution.

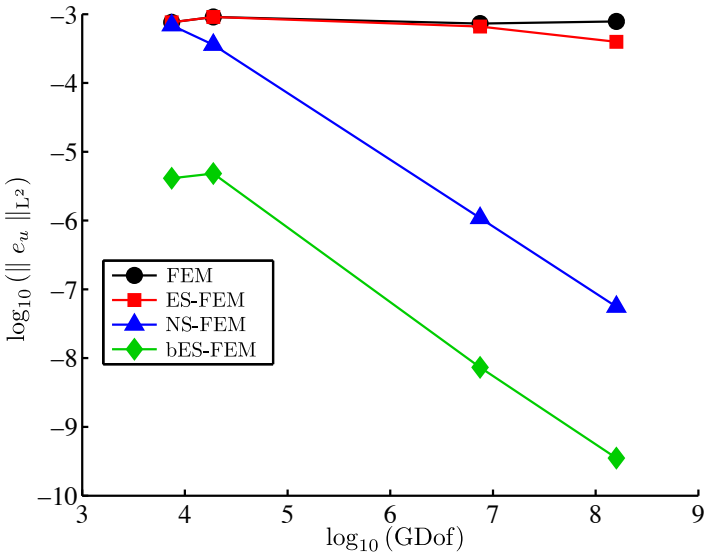

Figure 5.10: The logarithm of L2 norm in displacement for the plate (FEM, ES-FEM, NS-FEM and bES-FEM)

Table 5.4: Strain energy relative error for plate with hole (FEM, ES-FEM, NS-FEM, bES-FEM and the MINI element) with bulk modulus $\kappa = 10^7$

Num. of DOFs	FEM	ES-FEM	NS-FEM	bES-FEM	MINI
28	-99.9997	-99.9991	-65.4768	-24.6115	-15.8684
72	-99.9996	-99.9985	-73.1416	-13.9022	-13.1798
986	-78.2269	-74.9281	3.0111	-1.1299	-1.1054
3648	-71.5748	-58.8111	0.8862	-0.3655	-0.3023

Strain energy relative error is given by: $\left(\frac{W^{\text{Numerical}} - W^{\text{Reference}}}{W^{\text{Reference}}}\right) \times 100\%$.

Sharp V-notched specimen. A sharp V-notched specimen under tension is considered. The problem domain is given in Fig. 5.11. The square is clamped on the bottom edge, and a vertical stretch 0.05 is imposed on the top edge. The geometry is $A = 1$ and $B = 0.02$. The shear modulus $\mu = 0.6$ and $\kappa = 10^5$ (Poisson's ratio $\nu \approx 0.499997$). The total number of global degrees of freedom are DOFs = 28, 52, 66, 184 and 216.

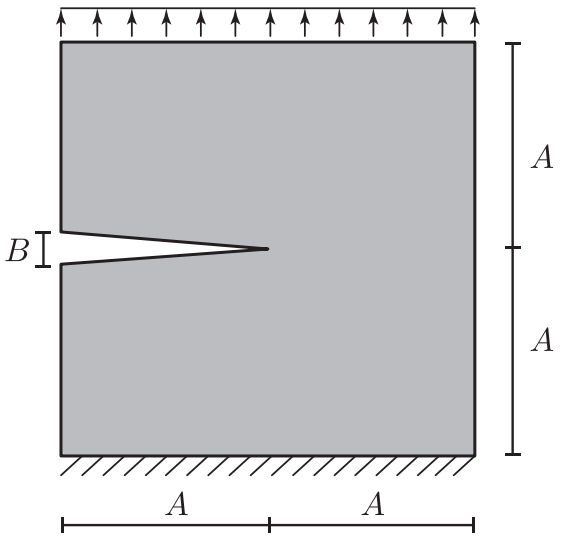

Figure 5.11: A square sharp V-notched specimen: geometry, boundary conditions and vertical stretches

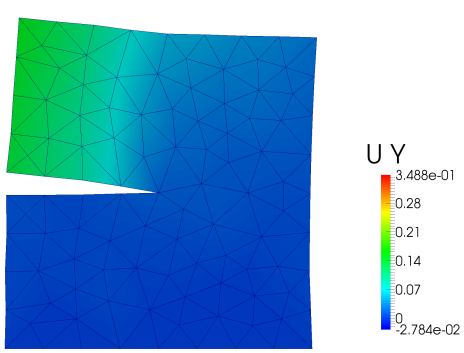

(a) FEM

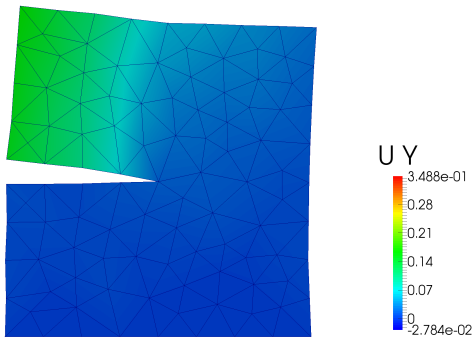

(b) ES-FEM

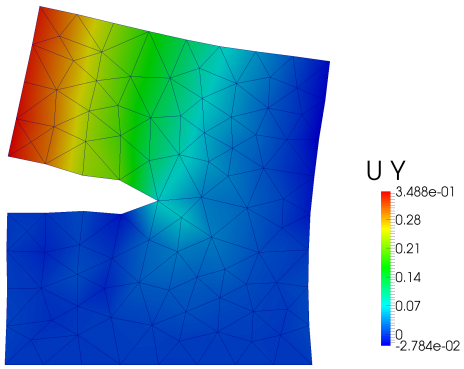

(c) NS-FEM

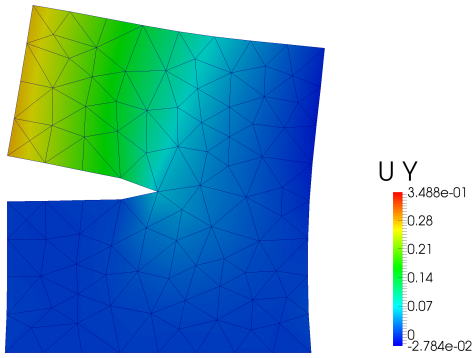

(d) bES-FEM

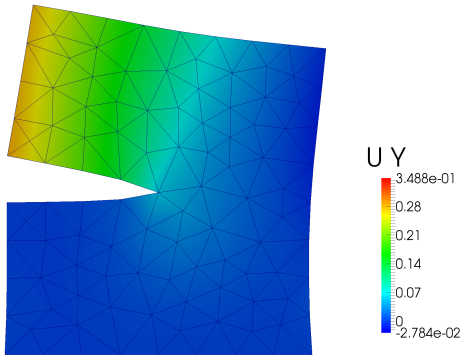

(e) MINI

Figure 5.12: Deformed shapes and displacements (u_y) of sharp V-notched square: Bulk modulus $\kappa = 10^5$ and the total number of degrees of freedoms is 216

The deformed shapes are given in Fig. 5.12. In this case, the current configuration of NS-FEM is more deformed than bES-FEM and the MINI, whereas displacements of bES-FEM are similar to those of the MINI element.

Fig. 5.13 illustrates the logarithm of L2 norm for this problem. The x- and y-axes denote the logarithm of the total number of degrees of freedom and the logarithm of L2 norm in displacements. The L2 norm is obtained as $\|\mathbf{e}\| = \left(\int \left(\mathbf{u}^* - \mathbf{u}^{\mathrm{h}}\right)' \left(\mathbf{u}^* - \mathbf{u}^{\mathrm{h}}\right) \mathrm{d}\Omega\right)^{\frac{1}{2}}$, where $\mathbf{u}^*$ is the reference solution and $\mathbf{u}^{\mathrm{h}}$ is the numerical solution.

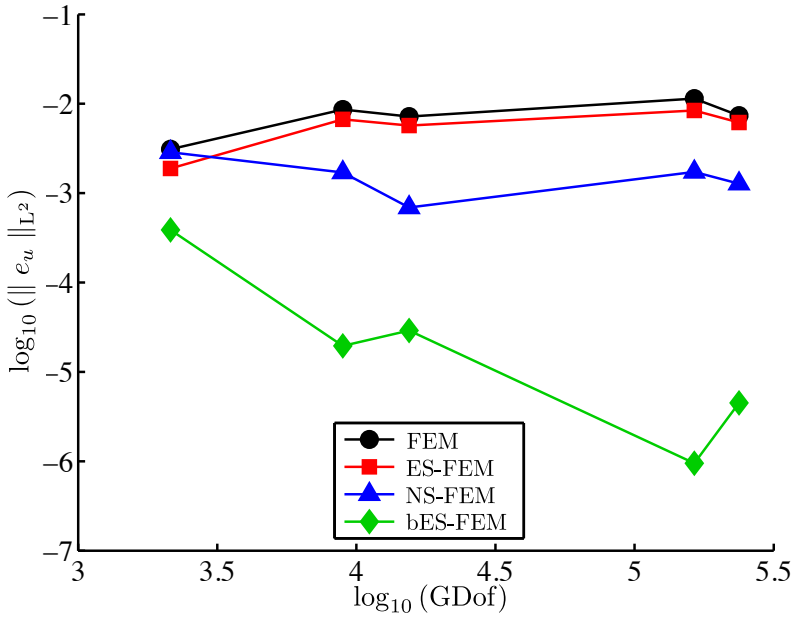

Figure 5.13: The logarithm of L2 norm in displacement for the square sharp V-notched specimen (FEM, ES-FEM, NS-FEM and bES-FEM)

The accuracy of the approach is indicated by Fig. 5.14. In Fig. 5.14 the solution using the MINI element in the DOLFIN finite element software is compared to the classical FEM, S-FEM and S-FEM enriched by bubbles. Similar to previous incompressible problems, the accuracy of edge-based strain smoothing is affected by the volumetric locking phenomenon. The MINI element in this test shows more accurate results than other numerical approaches; however bES-FEM also

provides accurate and stable results. One interesting point is the convergence of NS-FEM. The convergence curve of NS-FEM lies within the lower and upper bound solutions. This behaviour has been observed for linear elastic problems [82]. In linear elastic problems, NS-FEM and ES-FEM provide the upper and lower bound solution respectively, thereby the exact solution lies in between NS-FEM and ES-FEM. In this case, the exact solution may be placed in between NS-FEM and bES-FEM where the reference solution is located.

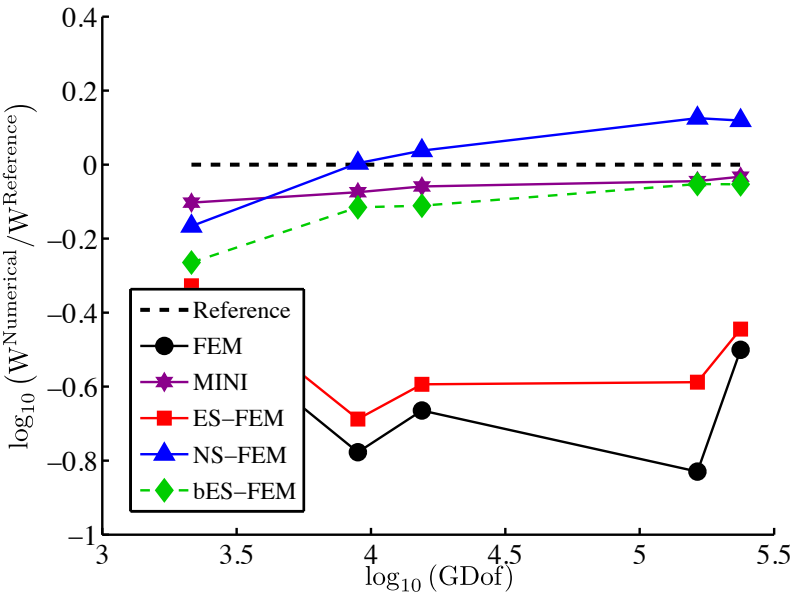

Figure 5.14: Strain energy convergence for the square sharp V-notched specimen: Poisson's ratio $\nu \approx 0.499997$

Table 5.5 provides detailed values of the relative error of strain energy for each discussed method. It is clearly shown that the MINI element is the most accurate result among the strain smoothing approaches. However, bES-FEM still provides relatively accurate and stable results with half accuracy of the MINI element. This percentage is the almost same as other incompressible problems studied in sections 5.3.1 and 5.3.2.

Table 5.5: Strain energy relative error for sharp V-notched square (FEM, ES-FEM, NS-FEM, bES-FEM and the MINI element) with bulk modulus $\kappa = 10^5$

Num. of GDof	FEM	ES-FEM	NS-FEM	bES-FEM	MINI
28	-33.7366	-27.9165	-15.3245	-23.2445	-9.7777
52	-54.0361	-49.7226	0.3910	-10.8873	-7.1832
66	-48.5564	-44.7730	3.8405	-10.4962	-5.7266
184	-56.3724	-44.4508	13.3948	-5.0999	-4.3576
216	-39.3833	-35.8755	12.6400	-5.1844	-3.2136

Strain energy relative error is given by: $\left(\frac{W^{\text{Numerical}} - W^{\text{Reference}}}{W^{\text{Reference}}}\right) \times 100\%$.

5.3.2 Mesh distortion sensitivity in compressibility

In this section, mesh distortion sensitivity in compressible material for the proposed method will be investigated. Firstly punch under pressure problem in 2D will be studied and then simple torsion and bending of a rectangular blocks in 3D are going to be discussed.

Punch under pressure. To tackle the performance of discussed S-FEM with distorted meshes in compressible limit, the punch problem is simulated. The geometry and discretisation are given in Fig. 5.15. Left, right and bottom edges are fully constrained and prescribed Dirichlet boundary conditions pressure $u_y = -0.25$ are imposed on the top edge as part punch pressure. Length $L = 1$ and bulk modulus $\kappa = 1.95$ ($\nu \approx 0.3605$) are used in this section. Three different types of meshes are used: 1) regular mesh $\alpha_{\text{distorted}} = 0.0$ and 2) artificially distorted meshes 0.1 and 0.3. As shown in Fig. 5.15, when the distortion factor α is increased, finite meshes are highly distorted.

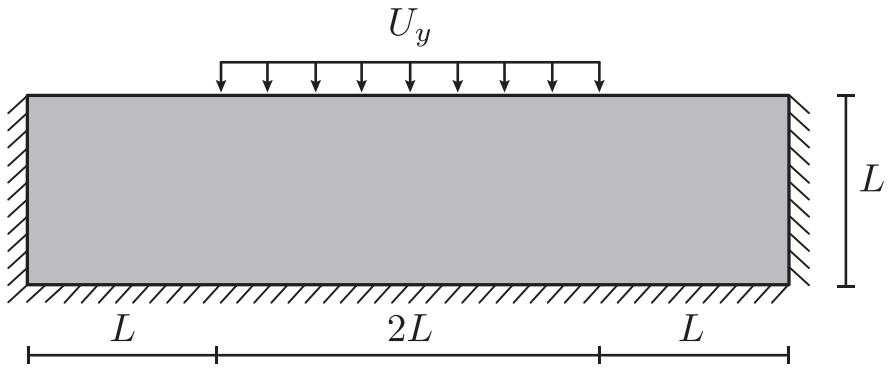

(a) Geometry, boundary conditions and prescribed pressure

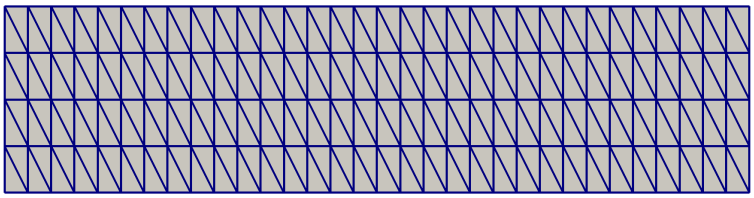

(b) Regular meshes

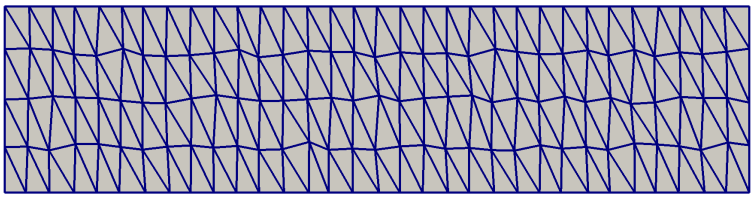

(c) Distorted Meshes: $\alpha_{\text{distorted}} = 0.1$

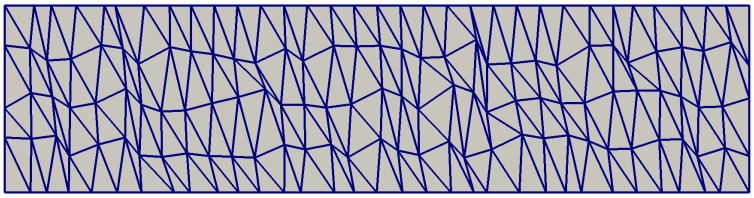

(d) Distorted Meshes: $\alpha_{\text{distorted}} = 0.3$

Figure 5.15: Punch problem under pressure: (a) geometry and Dirichlet boundary conditions, (b) discretiszation of regular T3 meshes, (c) discretisation of distorted T3 meshes ($\alpha_{\text{distorted}} = 0.1$) and (d) discretisation of distorted T3 meshes ($\alpha_{\text{distorted}} = 0.3$)

Fig. 5.16 shows the strain energy convergence for the punch problem with the numbers of elements 4×4, 8×4, 16×4 and 32×4. DOLFIN provides the numerical reference solution with a fine mesh (100×4).

It is well-known that ES-FEM is insensitive to the mesh distortion and more accurate than other numerical methods. The bubble-enhanced ES-FEM also shows its insensitivity to severely distorted meshes. Notable results given in Fig. 5.16 are that NS-FEM provides the worst accuracy rather than other strain smoothing approaches even FEM. It is clearly shown that NS-FEM shows its instability in mesh distortion problems as shown in Fig. 5.17. Also note that the MINI element provides the almost same convergence rate as FEM. In particular, when meshes are heavily distorted, the accuracy of FEM and the MINI element becomes similar.

The relative errors of strain energy for FEM, S-FEM, S-FEM enriched by the bubble and the MINI element can be found in Tables 5.6, 5.7 and 5.8. It can be seen that ES-FEM retains its accuracy and stability when whether or not meshes are distorted in this problem with around -0.8% of the error. Moreover bubble-enhanced strain smoothing is also seen to be insensitive to the distorted meshes in the compressible hyperelastic model where the relative error is almost half of the MINI element.

Note that since S-FEM shows better performance for distorted meshes, the MINI element is not suitable as the reference solution for this problem (see Tables 5.6, 5.7 and 5.8).

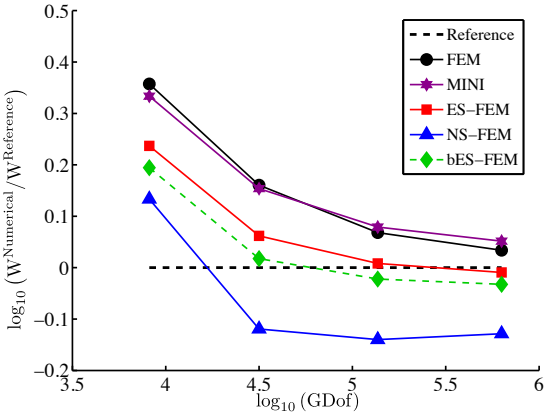

(a) Regular meshes

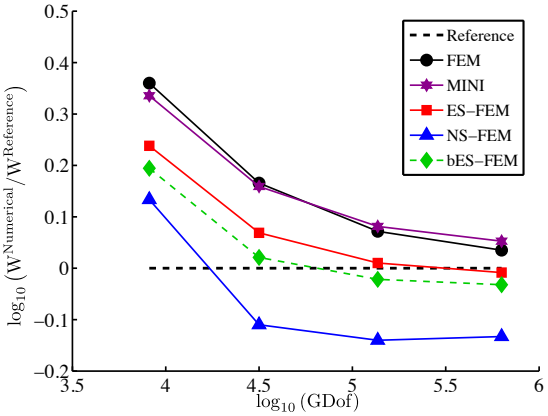

(b) Distorted Meshes $\alpha_{\text{distorted}} = 0.1$

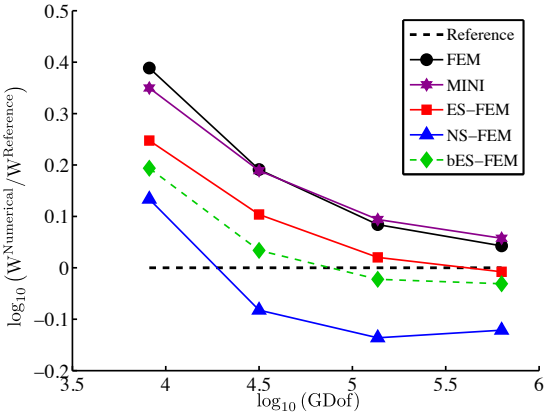

(c) Distorted Meshes $\alpha_{\text{distorted}} = 0.3$

Figure 5.16: Strain energy convergence for the Punch problem under pressure: (a) regular T3 meshes, (b) distorted T3 meshes ($\alpha_{\text{distorted}} = 0.1$) and (c) distorted T3 meshes ($\alpha_{\text{distorted}} = 0.3$)

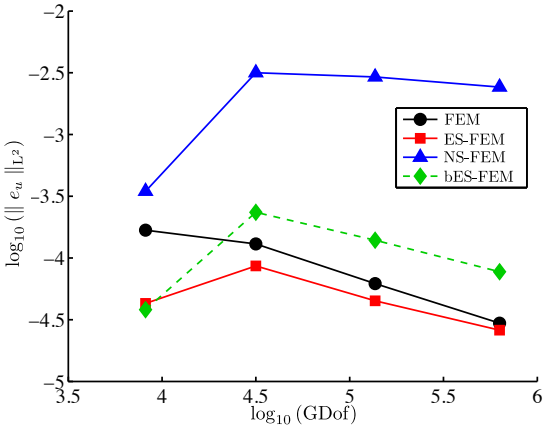

(a) Regular meshes

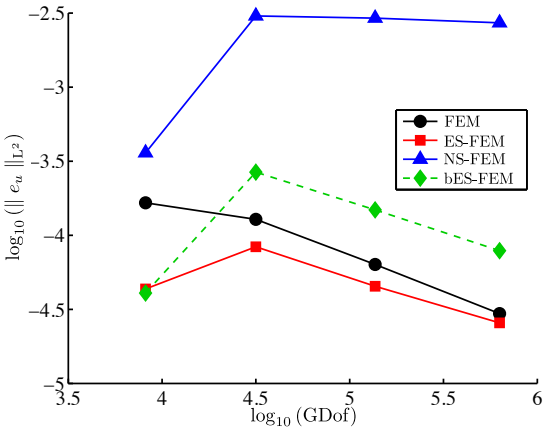

(b) Distorted Meshes: $\alpha_{\text{distorted}} = 0.1$

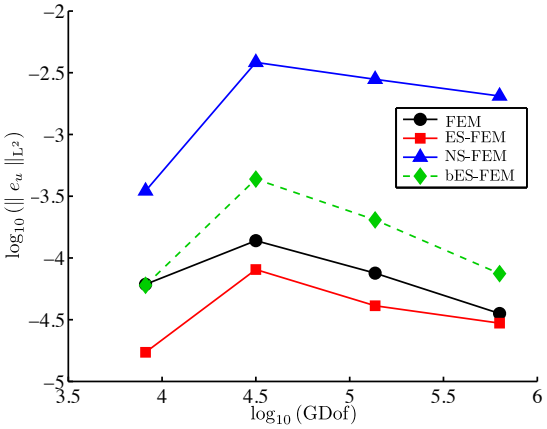

(c) Distorted Meshes: $\alpha_{\text{distorted}} = 0.3$

Figure 5.17: The logarithm of L2 norm for the Punch problem under pressure: (a) regular T3 meshes, (b) distorted T3 meshes ($\alpha_{\text{distorted}} = 0.1$) and (c) distorted T3 meshes ($\alpha_{\text{distorted}} = 0.3$)

Table 5.6: Strain energy relative error for Punching problem for FEM, ES-FEM, NS-FEM, bES-FEM and the MINI element with regular T3 meshes

Num. of elements	FEM	ES-FEM	NS-FEM	bES-FEM	MINI
4×4	42.9496	26.7358	14.2737	21.4592	39.5926
8×4	17.4018	6.3710	-11.2564	1.7797	16.6296
16×4	7.0569	0.8245	-13.0589	-2.1985	8.2183
32×4	3.4401	-0.9313	-12.0706	-3.2009	5.2887

Strain energy relative error is given by: $\left(\frac{W^{\text{Numerical}} - W^{\text{Reference}}}{W^{\text{Reference}}}\right) \times 100\%$.

Table 5.7: Strain energy relative error for Punching problem for FEM, ES-FEM, NS-FEM, bES-FEM and the MINI element with distorted T3 meshes ($\alpha_{\text{distorted}} = 0.1$)

Num. of elements	FEM	ES-FEM	NS-FEM	bES-FEM	MINI
4×4	43.3460	26.8851	14.2828	21.4695	39.8607
8×4	18.0323	7.1311	-10.4057	2.1292	17.2383
16×4	7.4388	1.0299	-13.0674	-2.1414	8.47630
32×4	3.5728	-0.8410	-12.4376	-3.1630	5.4043

Strain energy relative error is given by: $\left(\frac{W^{\text{Numerical}} - W^{\text{Reference}}}{W^{\text{Reference}}}\right) \times 100\%$.

Table 5.8: Strain energy relative error for Punching problem for FEM, ES-FEM, NS-FEM, bES-FEM and the MINI element with distorted T3 meshes ($\alpha_{\text{distorted}} = 0.3$)

Num. of elements	FEM	ES-FEM	NS-FEM	bES-FEM	MINI
4×4	47.5024	28.0809	14.2989	21.3682	41.8839
8×4	21.0752	10.9316	-7.9081	3.4391	20.8156
16×4	8.7765	2.0510	-12.7207	-2.2044	9.8479
32×4	4.3606	-0.7629	-11.4268	-3.0503	5.9217

Strain energy relative error is given by: $\left(\frac{W^{\text{Numerical}} - W^{\text{Reference}}}{W^{\text{Reference}}}\right) \times 100\%$.

Simple torsion of a rectangular block. For 3D mesh distortion sensitivity in the incompressible limit, simple torsion of a rectangular block (given in sections 2.2.6 and 5.2.4 of Reference [123]) is taken. Given cylindrical coordinates and Dirichlet boundary conditions are based on a solid cylinder; however, in this test, Dirichlet boundary conditions are imposed to the rectangular solid. Firstly, polar cylindrical coordinates are given by

$$0 \leq R \leq A, \quad 0 \leq \Theta \leq 2\pi, \quad 0 \leq Z \leq L \tag{5.13}$$

The corresponding unit vectors for current cylindrical coordinates (r, θ, z)

$$e_r = \begin{bmatrix} \cos\theta \\ \sin\theta \\ 0 \end{bmatrix}, \quad e_\theta = \begin{bmatrix} -\sin\theta \\ \cos\theta \\ 0 \end{bmatrix}, \quad e_z = \begin{bmatrix} 0 \\ 0 \\ 1 \end{bmatrix} \tag{5.14}$$

The deformation in cylindrical polar coordinates is

$$r = R, \quad \theta = \Theta + \tau Z, \quad z = Z \tag{5.15}$$

where τ is the twist per unit length. The geometry of the rectangular block in the Cartesian coordinates (X, Y, Z) is given in Fig. 5.18 with following parameters: $A = 0.5$, $B = 2$, $C = 0.5$ and the twist $\tau = \pi/4 = 90°$.

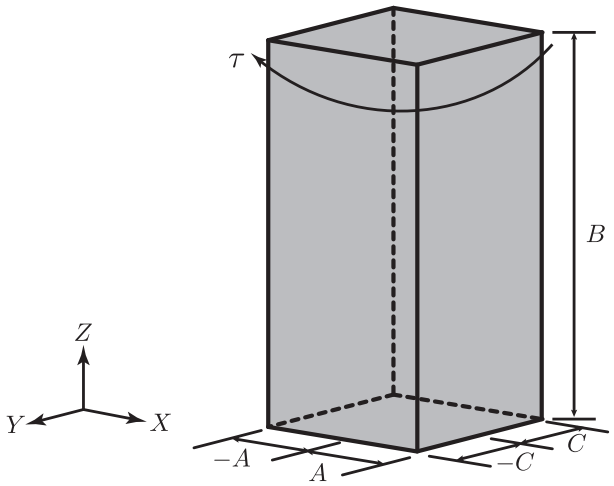

Figure 5.18: Simple torsion of a rectangular block: geometry in the Cartesian coordinates (X, Y, Z)

The deformation gradient $\mathbf{F}$ and right Cauchy-Green tensor are respectively

$$\begin{aligned} \mathbf{F} &= \begin{bmatrix} 1 & 0 & 0 \\ 0 & 1 & \tau R \\ 0 & 0 & 1 \end{bmatrix} \\ \mathbf{C} &= \begin{bmatrix} 1 & 0 & 0 \\ 0 & 1 & \tau R \\ 0 & \tau R & 1+\tau^2 R^2 \end{bmatrix} \end{aligned} \tag{5.16}$$

Given cylindrical coordinates can be formulated as follows

$$\begin{aligned} x &= r\cos\theta = R\cos(\theta+\tau Z) = R\left[\cos\theta\cos(\tau Z) - \sin\theta\sin(\tau Z)\right] \\ y &= r\sin\theta = R\sin(\theta+\tau Z) = R\left[\cos(\tau Z)\sin\theta + \cos\theta\sin(\tau Z)\right] \\ z &= Z \end{aligned} \tag{5.17}$$

where $R = \sqrt{X^2+Y^2}$ and $\tan\theta = \dfrac{Y}{X}$.

Therefore, Dirichlet boundary conditions for simple torsion, which are imposed on a rectangular block, can be represented as

- Bottom surface ($Z = 0$): $\left(u_{1(x)}, u_{2(y)}, u_{3(z)}\right) = (0, 0, 0)$

- Top surface ($Z = B$): $u_{1(x)} = X\cos(\tau L) - Y\sin(\tau L) - X$
  $u_{2(y)} = Y\cos(\tau L) + X\sin(\tau L) - Y$
  $u_{3(z)} = 0$

- Left surface ($X = -A$)): $u_{1(x)} = -A\cos(\tau Z) - Y\sin(\tau Z) + A$
  $u_{2(y)} = Y\cos(\tau Z) - A\sin(\tau Z) - Y$
  $u_{3(z)} = 0$

- Right surface ($X = A$)): $u_{1(x)} = A\cos(\tau Z) - Y\sin(\tau Z) - A$
  $u_{2(y)} = Y\cos(\tau Z) + A\sin(\tau Z) - Y$
  $u_{3(z)} = 0$

- Front surface ($Y = -C$)): $u_{1(x)} = X\cos(\tau L) + C\sin(\tau L) - X$
  $u_{2(y)} = -C\cos(\tau L) + X\sin(\tau L) + C$
  $u_{3(z)} = 0$

- Back surface ($Y = C$): $u_{1(x)} = X\cos(\tau L) - C\sin(\tau L) - X$
  $u_{2(y)} = C\cos(\tau L) + X\sin(\tau L) - C$
  $u_{3(z)} = 0$

Fig. 5.19 represents initial and current configurations for the rectangular block under simple torsion with regular and distorted meshes $\alpha_{\text{distorted}} = 0.1$ and 0.3. Lamé's parameters, shear modulus $\mu = 0.6$ and bulk modulus $\kappa = 1.95$, are used in this test and the numerical solution of DOLFIN with a fine mesh is provided as the reference solution. The number of elements is $4 \times 4 \times 4$, $4 \times 4 \times 8$, $4 \times 4 \times 16$ and $4 \times 4 \times 32$.

Fig. 5.20 depicts the logarithm of ratio of the numerical $W^{\text{Numerical}}$ to the reference solution $W^{\text{Analytical}}$ strain energy in the vertical axis and the logarithm of global degrees of freedom (GDof) in the horizontal axis. The MINI element with very fine meshes ($4 \times 4 \times 100$) is also used as the pseudo-exact solution for simple torsion of a rectangular block.

In 3D mesh distortion problems, ss shown in Fig. 5.20 with finer meshes, in case 3, the conventional FEM fails to converge, while S-FEM shows more accurate and stable results. The MINI element is shown stable results with regular and slightly distorted meshes ($\alpha_{\text{distorted}} = 0.1$). However a remarkable result is shown that the reference solution (the MINI element) fails to converge when highly distorted meshes are used.

While FEM and the MINI element do not converge for distorted meshes, gradient smoothing methods converged smoothly with either regular mesh or distorted meshes. FS-FEM shows its insensitivity to mesh distortion in 3D non-homogeneous Dirichlet boundary condition problem and ES-FEM is shown to be able to handle mesh distortion in 2D in section 5.3.2. Although bubble-enriched ES-FEM could not effectively handle mesh distortion problems, FS-FEM enriched by the bubbles shows significant performance with severely distorted meshes in 3D.

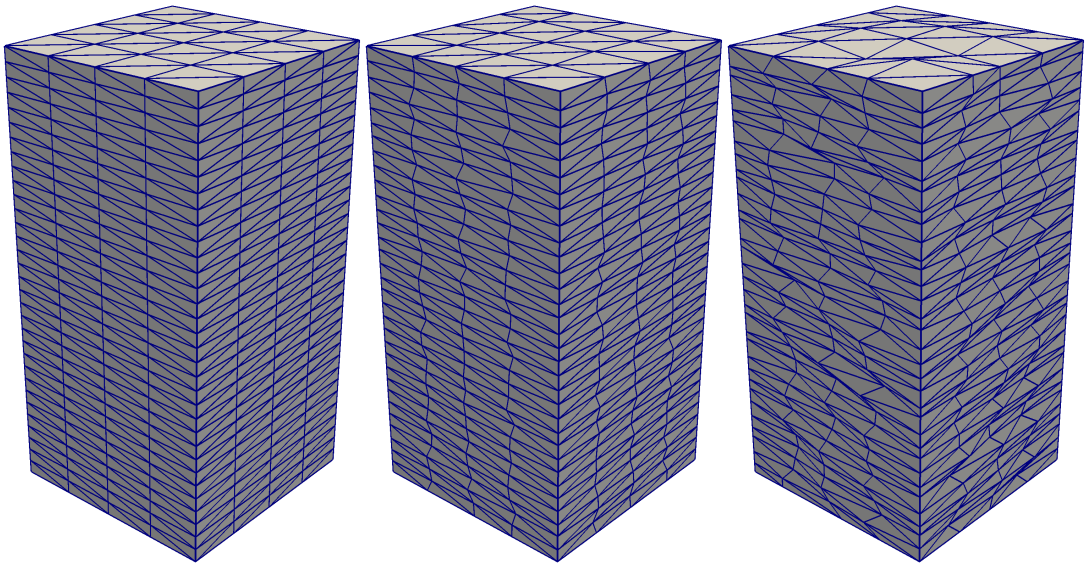

(a) Regular mesh (b) $\alpha_{\text{distorted}} = 0.1$ (c) $\alpha_{\text{distorted}} = 0.3$

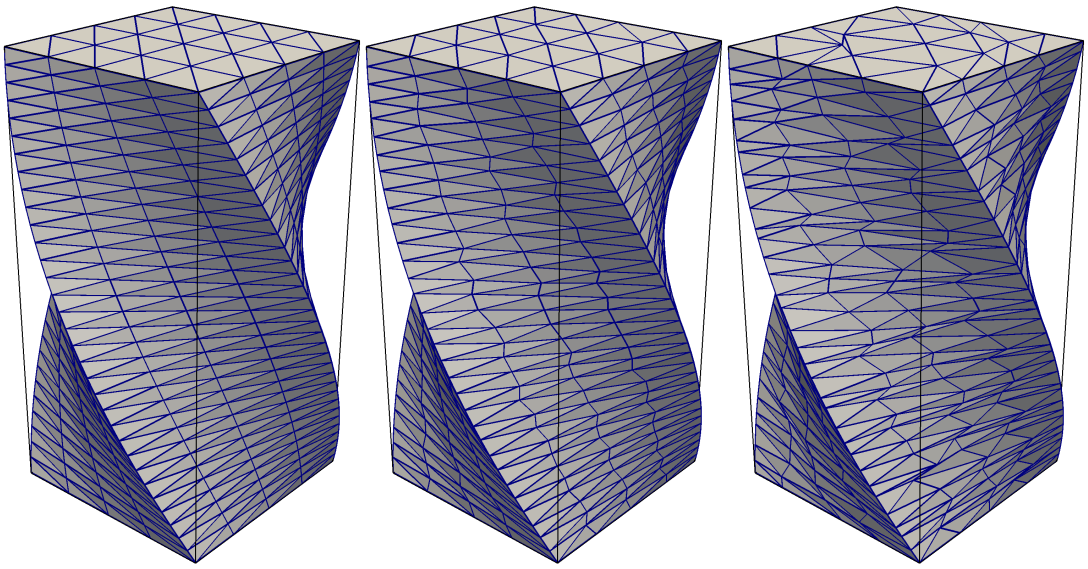

(d) Regular mesh (e) $\alpha_{\text{distorted}} = 0.1$ (f) $\alpha_{\text{distorted}} = 0.3$

Figure 5.19: Initial and deformed shapes for the simple torsion problem: (a,b,c) Initial configurations with regular, distorted meshes $\alpha_{\text{distorted}} = 0.1$ and 0.3 and (d,e,f) Current configurations with regular, distorted meshes $\alpha_{\text{distorted}} = 0.1$ and 0.3

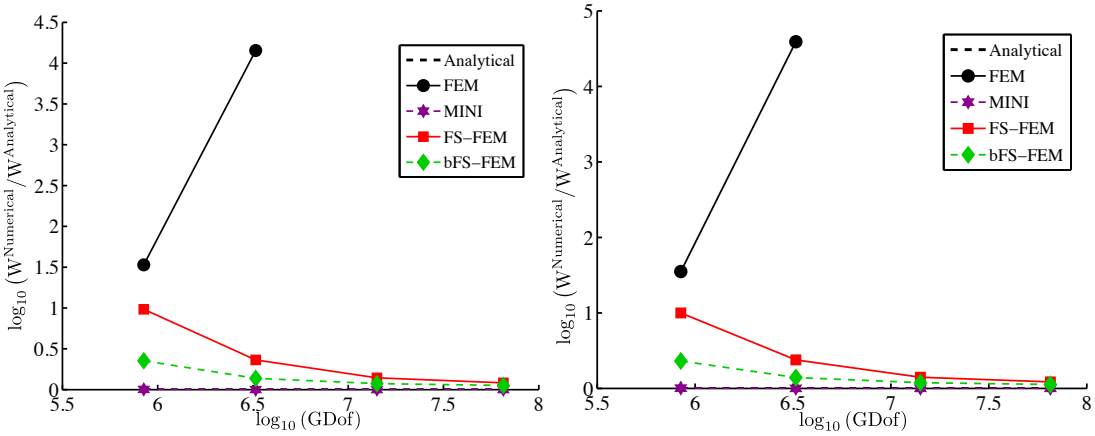

(a) Regular mesh

(b) Distorted mesh $\alpha_{\text{distorted}} = 0.1$

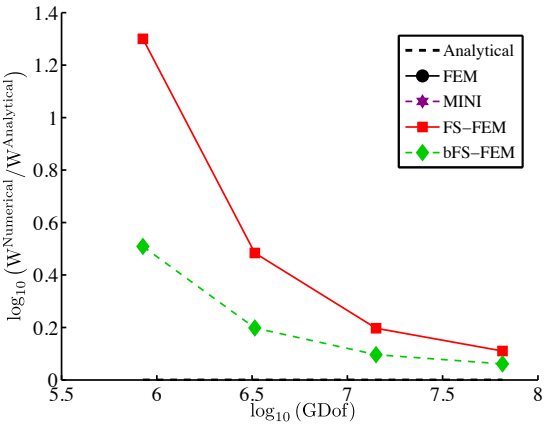

(c) Distorted mesh $\alpha_{\text{distorted}} = 0.3$

Figure 5.20: Convergence in strain energy for the simple torsion problem (FEM, FS-FEM and bFS-FEM): (a) regular mesh, (2) distorted mesh $\alpha_{\text{distorted}} = 0.1$ and (3) distorted mesh $\alpha_{\text{distorted}} = 0.3$

Bending of a rectangular block. Mesh distortion sensitivity problem in 3D is considered once more. The geometry of the problem and its boundary conditions are shown in Fig. 5.21 [123].

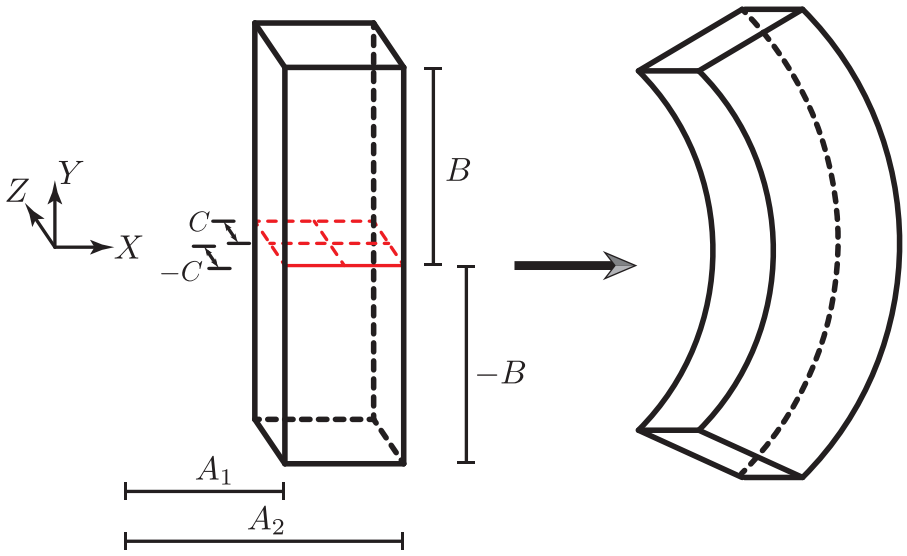

Figure 5.21: Bending of a rectangular block into a sector of a circular cylindrical tube: geometry and boundary conditions

The reference Cartesian coordinates (X, Y, Z) for the bending problem are

$$X = (A_1, A_2)\,, \quad Y = (-B, B)\,, \quad Z = (-C, C) \tag{5.18}$$

where $(A_1, A_2, B, C > 0)$. Cartesian coordinates are defined as

$$x = r\cos\theta = \sqrt{2\alpha X}\cos\frac{Y}{\alpha}, \quad y = r\sin\theta = \sqrt{2\alpha X}\sin\frac{Y}{\alpha}, \quad z = Z \tag{5.19}$$

and hence Dirichlet BCs on all surfaces can be expressed as

- Bottom surface ($Y = -B$): $u_{1(x)} = \sqrt{2\alpha X}\cos\dfrac{-B}{\alpha} - X$
  $u_{2(y)} = \sqrt{2\alpha X}\sin\dfrac{-B}{\alpha} + B$
  $u_{3(z)} = 0$

- Top surface ($Y = B$): $u_{1(x)} = \sqrt{2\alpha X}\cos\dfrac{B}{\alpha} - X$
  $u_{2(y)} = \sqrt{2\alpha X}\sin\dfrac{B}{\alpha} - B$
  $u_{3(z)} = 0$

- Front surface ($Z = -C$): $u_{1(x)} = \sqrt{2\alpha X}\cos\dfrac{Y}{\alpha} - X$
  $u_{2(y)} = \sqrt{2\alpha X}\sin\dfrac{Y}{\alpha} - Y$
  $u_{3(z)} = 0$

- Back surface ($Z = C$): $u_{1(x)} = \sqrt{2\alpha X}\cos\dfrac{Y}{\alpha} - X$
  $u_{2(y)} = \sqrt{2\alpha X}\sin\dfrac{Y}{\alpha} - Y$
  $u_{3(z)} = 0$

- Left-handed surface ($X = A_1$): $u_1 = \sqrt{2\alpha A_1}\cos\dfrac{Y}{\alpha} - A_1$
  $u_2 = \sqrt{2\alpha A_1}\sin\dfrac{Y}{\alpha} - Y$
  $u_3 = 0$

- Right-handed surface ($X = A_2$): $u_{1(x)} = \sqrt{2\alpha A_2}\cos\dfrac{Y}{\alpha} - A_2$
  $u_{2(y)} = \sqrt{2\alpha A_2}\sin\dfrac{Y}{\alpha} - Y$
  $u_{3(z)} = 0$

The analytical solution for this problem can be computed as in Appendix D.4

$$W = \int_2^3 \int_{-2}^2 \int_{-0.5}^{0.5} \left\{ \mu \frac{(\alpha - 2X)^2}{4\alpha X} \right\} \mathrm{d}Z\mathrm{d}Y\mathrm{d}X \approx 1.086 \tag{5.20}$$

with $\alpha = 2.0$, $A_1 = 2$, $A_2 = 3$, $B = 2$, $C = 0.5$, shear modulus $\mu = 0.6$ and bulk modulus $\kappa = 1.95$.

Fig. 5.22 illustrates the initial and deformed shapes of the problem with regular and highly distorted meshes with mesh distortion factors $\alpha_{\text{distorted}} = 0.1$, 0.3 and 0.4, and $4 \times 32 \times 4$ elements along x-, y- and z-axes.

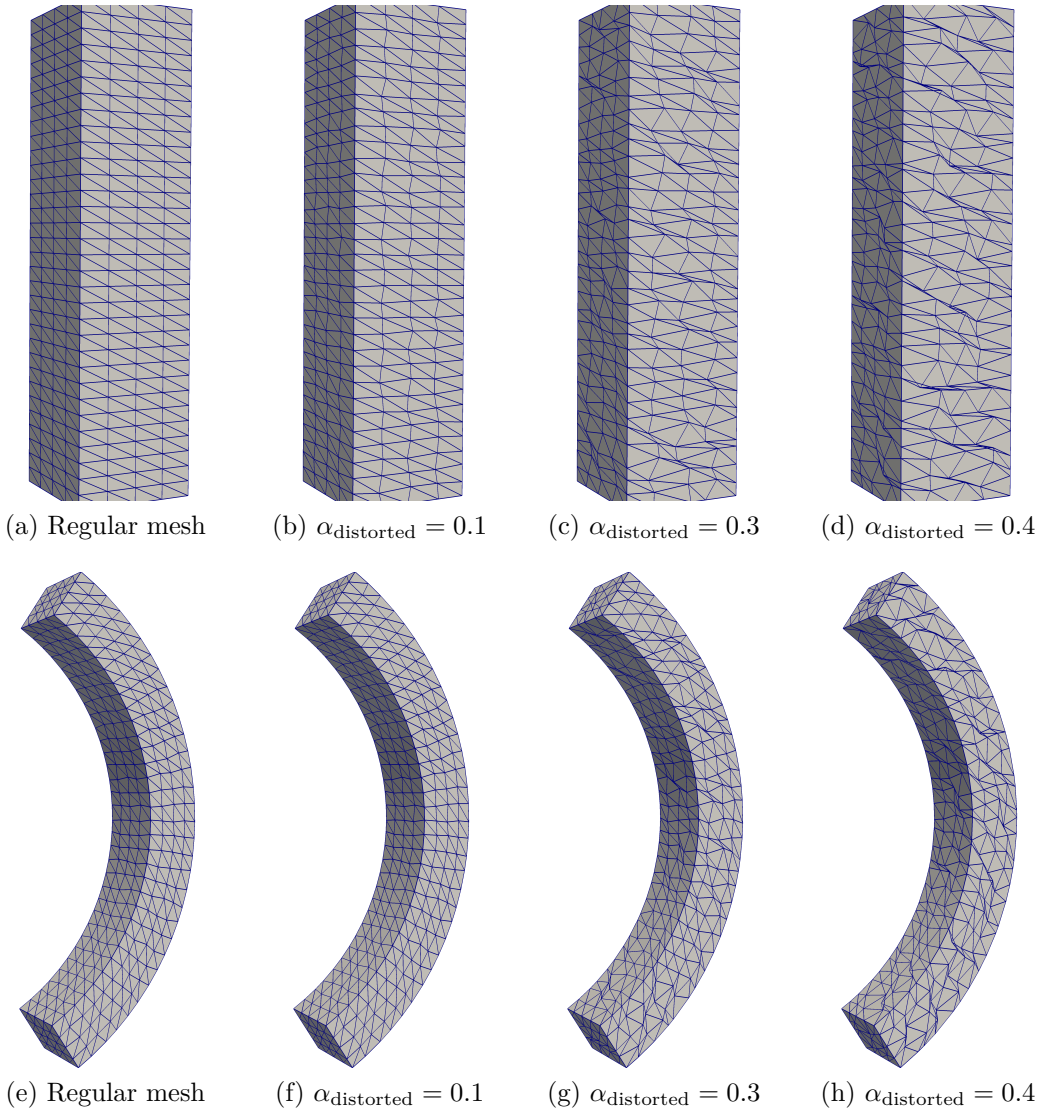

(a) Regular mesh (b) $\alpha_{\text{distorted}} = 0.1$ (c) $\alpha_{\text{distorted}} = 0.3$ (d) $\alpha_{\text{distorted}} = 0.4$

(e) Regular mesh (f) $\alpha_{\text{distorted}} = 0.1$ (g) $\alpha_{\text{distorted}} = 0.3$ (h) $\alpha_{\text{distorted}} = 0.4$

Figure 5.22: Initial and current shapes of the rectangular block with distorted meshes: (a,b,c) initial configurations with $\alpha_{\text{distorted}} = 0.1$, 0.3 and 0.4, (d,e,f) deformed configurations with $\alpha_{\text{distorted}} = 0.1$, $= 0.3$ and 0.4

For this problem, different number of elements are considered: (1) case 1 is that number of element is $2 \times 4 \times 2$, $2 \times 8 \times 2$, $2 \times 16 \times 2$, and $2 \times 32 \times 2$, and (2) case 2 is $4 \times 4 \times 4$, $4 \times 8 \times 4$, $4 \times 16 \times 4$ and $4 \times 32 \times 4$.

The convergence of strain energy of FEM, S-FEM and the MINI element for the bending is shown in Figs. 5.23 and 5.24. Also, x-axis represents the logarithm of the global degrees of freedom (GDof) and y-axis describes the logarithm of the ratio in strain energy of the numerical $W_{\text{Numerical}}$ to the analytical solution $W_{\text{Analytical}}$, respectively.

As shown in Figs. 5.23 and 5.24, when the mesh becomes severely distorted, FEM fails to converge with the fine mesh. Face-based S-FEM, on the other hand, converges smoothly to the analytical solution.

Detailed relative errors in strain energy can be found in Tables 5.9, 5.10, 5.11 and 5.12 with regular mesh and heavily distorted meshes, respectively. With severely distorted and fine meshes, the FEM solution fails to reach the analytical solution; however, FS-FEM successfully converges regardless of regular or distorted meshes. Interestingly, in this test, FS-FEM shows better performance than enriched FS-FEM as previous mesh distortion problems whereas its convergence rate is faster and more stable than the standard face-based S-FEM.

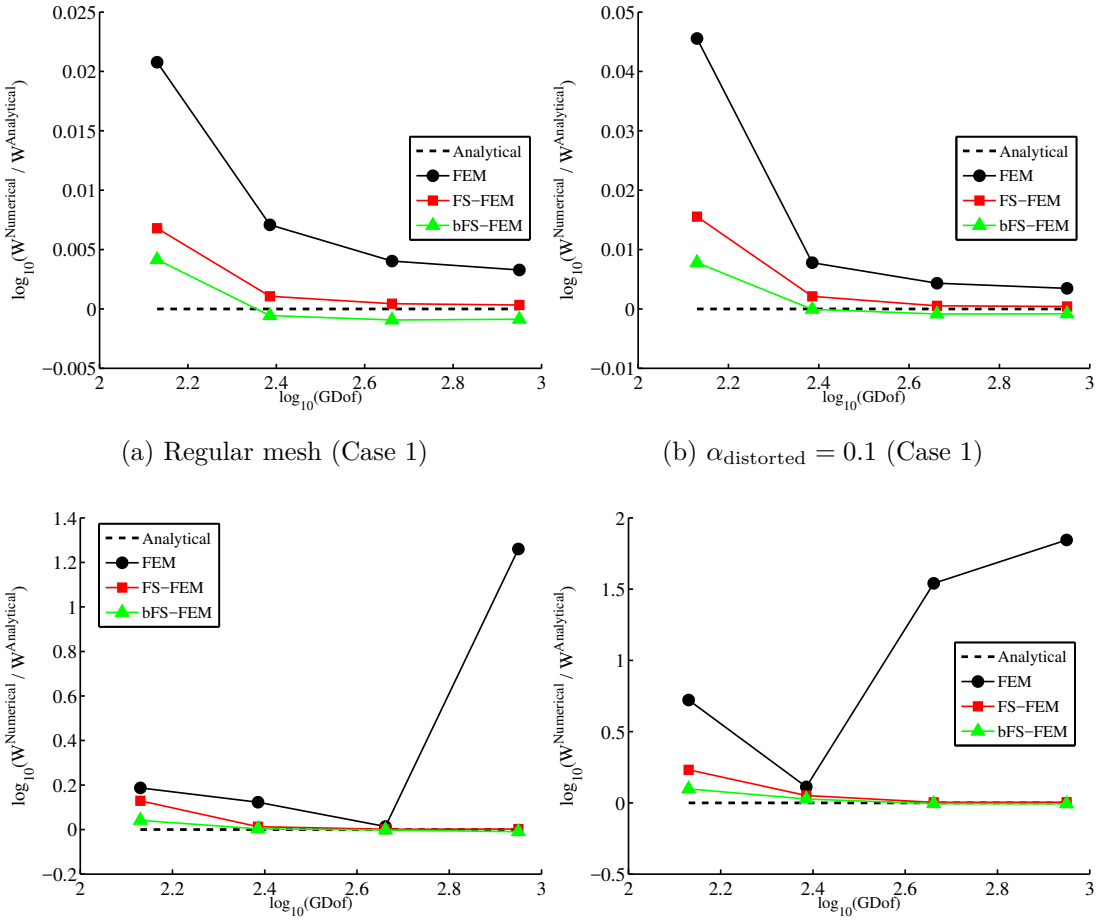

(a) Regular mesh (Case 1)

(b) $\alpha_{\text{distorted}} = 0.1$ (Case 1)

(c) $\alpha_{\text{distorted}} = 0.3$ (Case 1)

(d) $\alpha_{\text{distorted}} = 0.4$ (Case 1)

Figure 5.23: Strain energy convergence for the bending block problem (FEM, FS-FEM and bFS-FEM): (a) strain energy with regular mesh, (b) strain energy with distorted mesh $\alpha_{\text{distorted}} = 0.1$, (c) strain energy with distorted mesh $\alpha_{\text{distorted}} = 0.3$ and (d) strain energy with distorted mesh $\alpha_{\text{distorted}} = 0.4$

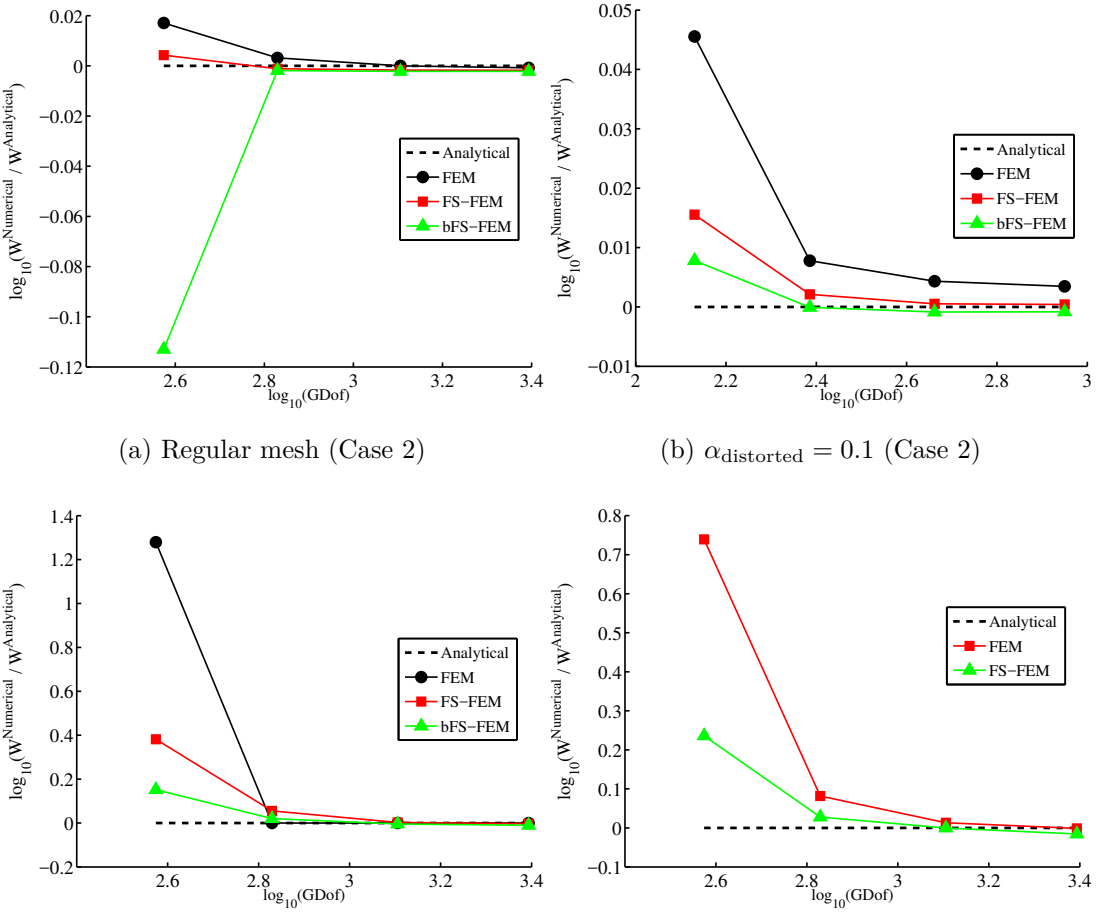

(a) Regular mesh (Case 2)

(b) $\alpha_{\text{distorted}} = 0.1$ (Case 2)

(c) $\alpha_{\text{distorted}} = 0.3$ (Case 2)

(d) $\alpha_{\text{distorted}} = 0.4$ (Case 2)

Figure 5.24: Strain energy convergence for the bending block problem (FEM, FS-FEM and bFS-FEM): (a) strain energy with regular mesh, (b) strain energy with distorted mesh $\alpha_{\text{distorted}} = 0.1$, (c) strain energy with distorted mesh $\alpha_{\text{distorted}} = 0.3$ and (d) strain energy with distorted mesh $\alpha_{\text{distorted}} = 0.4$

Table 5.9: Strain energy relative error for the bending block with regular mesh (FEM, FS-FEM and bFS-FEM)

	Regular mesh		
	FEM	FS-FEM	bFS-FEM
2×4×2	4.9001	1.5773	0.9607
2×8×2	1.6447	0.2454	-0.1297
2×16×2	0.9323	0.1016	-0.2142
2×32×2	0.7585	0.0769	-0.2005
4×4×4	4.0175	0.9849	-22.9068
4×8×4	0.7339	-0.2622	-0.4313
4×16×4	0.0032	-0.3879	-0.5017
4×32×4	-0.1797	-0.4085	-0.5065

Strain energy relative error is given by: $\left(\frac{W^{\text{Numerical}} - W^{\text{Analytical}}}{W^{\text{Analytical}}}\right) \times 100\%$.

Table 5.10: Strain energy relative error for the bending block with distorted mesh $\alpha_{\text{distorted}} = 0.1$ (FEM, FS-FEM and bFS-FEM)

	Distorted mesh $\alpha_{\text{distorted}} = 0.1$		
	FEM	FS-FEM	bFS-FEM
2×4×2	11.0568	3.6436	1.8102
2×8×2	1.8077	0.4890	-0.0157
2×16×2	1.0003	0.1209	-0.1986
2×32×2	0.8017	0.0949	-0.1916
4×4×4	19.8688	9.2666	3.3811
4×8×4	2.0408	0.4275	-0.2505
4×16×4	0.1075	-0.3392	-0.4874
4×32×4	-0.1675	-0.3984	-0.5000

Strain energy relative error is given by: $\left(\frac{W^{\text{Numerical}} - W^{\text{Analytical}}}{W^{\text{Analytical}}}\right) \times 100\%$.

Table 5.11: Strain energy relative error for the bending block with distorted mesh $\alpha_{\text{distorted}} = 0.3$ (FEM, FS-FEM and bFS-FEM)

	Distorted mesh $\alpha_{\text{distorted}} = 0.3$		
	FEM	FS-FEM	bFS-FEM
2×4×2	53.8079	34.6637	10.0197
2×8×2	32.6221	3.0031	0.7442
2×16×2	3.1583	0.3372	-0.4431
2×32×2	1721.2780	0.4674	-2.1339
4×4×4	1802.4257	140.7878	41.9260
4×8×4	Fails	13.5612	4.8012
4×16×4	Fails	0.5859	-1.0343
4×32×4	Fails	-0.7379	-2.3619

Strain energy relative error is given by: $\left(\frac{W^{\text{Numerical}} - W^{\text{Analytical}}}{W^{\text{Analytical}}}\right) \times 100\%$.

Table 5.12: Strain energy relative error for the bending block with distorted mesh $\alpha_{\text{distorted}} = 0.4$ (FEM, FS-FEM and bFS-FEM)

	Distorted mesh $\alpha_{\text{distorted}} = 0.4$		
	FEM	FS-FEM	bFS-FEM
2×4×2	426.3759	70.4614	25.3211
2×8×2	29.3479	12.5453	6.2909
2×16×2	3371.5573	0.8078	-1.2987
2×32×2	6900.4850	0.9846	-1.5653
4×4×4	Fails	448.6516	72.2076
4×8×4	Fails	20.7111	6.6395
4×16×4	Fails	3.0716	-0.0491
4×32×4	Fails	-0.2531	-3.5229

Strain energy relative error is given by: $\left(\frac{W^{\text{Numerical}} - W^{\text{Analytical}}}{W^{\text{Analytical}}}\right) \times 100\%$.

5.3.3 Mesh distortion sensitivity in incompressibility

In this section the mesh distortion sensitivity in incompressibility problems is investigated.

Bevelled cantilever beam. The bevelled cantilever beam is considered for mesh distortion sensitivity in incompressible limit. The geometry, boundary conditions and loading are shown in Fig. 5.25. The length $L = 0.5$ and the external force $P = -0.1$ are used. Poisson's ratio is $\nu \approx 0.49999997$ (the bulk modulus $\kappa = 10^7$) and regular mesh, distorted meshes $\alpha_{\text{distorted}} = 0.1$ and 0.3 are also used. For this problem, DOLFIN finite element software with the MINI element is used as the analytical solution with fine meshes (100×100).

Fig. 5.25 shows the discretisation of regular and distorted meshes and Figs. 5.26 and 5.27 illustrate its deformed shapes of S-FEM and the MINI element with displacements U_x and U_y.

The convergence of strain energy for the bevelled beam with distorted meshes is given in Fig. 5.28. The horizontal axis represents the logarithm of global degrees of freedom (GDof) and the vertical axis shows the logarithm of the ratio of the numerical solution $W^{\text{Numerical}}$ to the analytical solution $W^{\text{Analytical}}$ of strain energy, respectively. Although the meshes are distorted, ES-FEM is locked in quasi-incompressible model. However, node-based and bubble-enriched edge-based S-FEM give accurate and reliable results as does the MINI element. Also, the L2 norm in displacements for each methods are shown in Fig. 5.29.

The detailed relative errors of strain energy of FEM, S-FEM, bES-FEM and the MINI element for the bevelled beam problem are provided in Table 5.13. In particular when meshes are highly distorted, the relative error of the MINI elements is increased while that of bES-FEM remains accurate.

Consequently it is shown that the bubble-enhanced gradient smoothing effectively handles mesh distortion sensitivity alleviating locking as well.

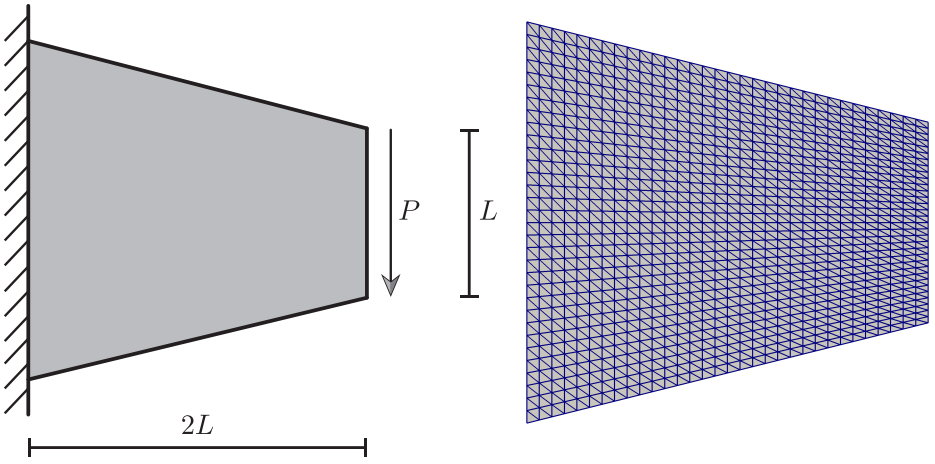

(a) Geometry, boundary conditions and loading

(b) Regular meshes

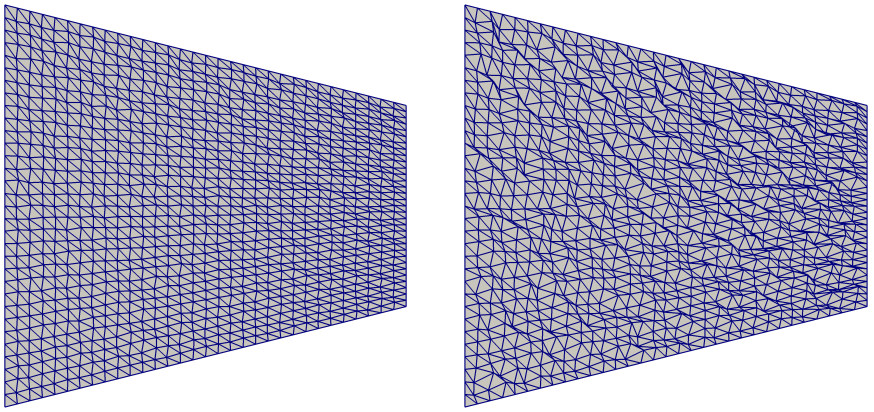

(c) Distorted Meshes: $\alpha_{\text{distorted}} = 0.1$

(d) Distorted Meshes: $\alpha_{\text{distorted}} = 0.3$

Figure 5.25: A bevelled cantilever beam: (a) the geometry, the boundary conditions and the loading, (b) discretisation of regular T3 meshes, (c) discretisation of distorted T3 meshes ($\alpha_{\text{distorted}} = 0.1$) and (d) discretisation of distorted T3 meshes ($\alpha_{\text{distorted}} = 0.3$)

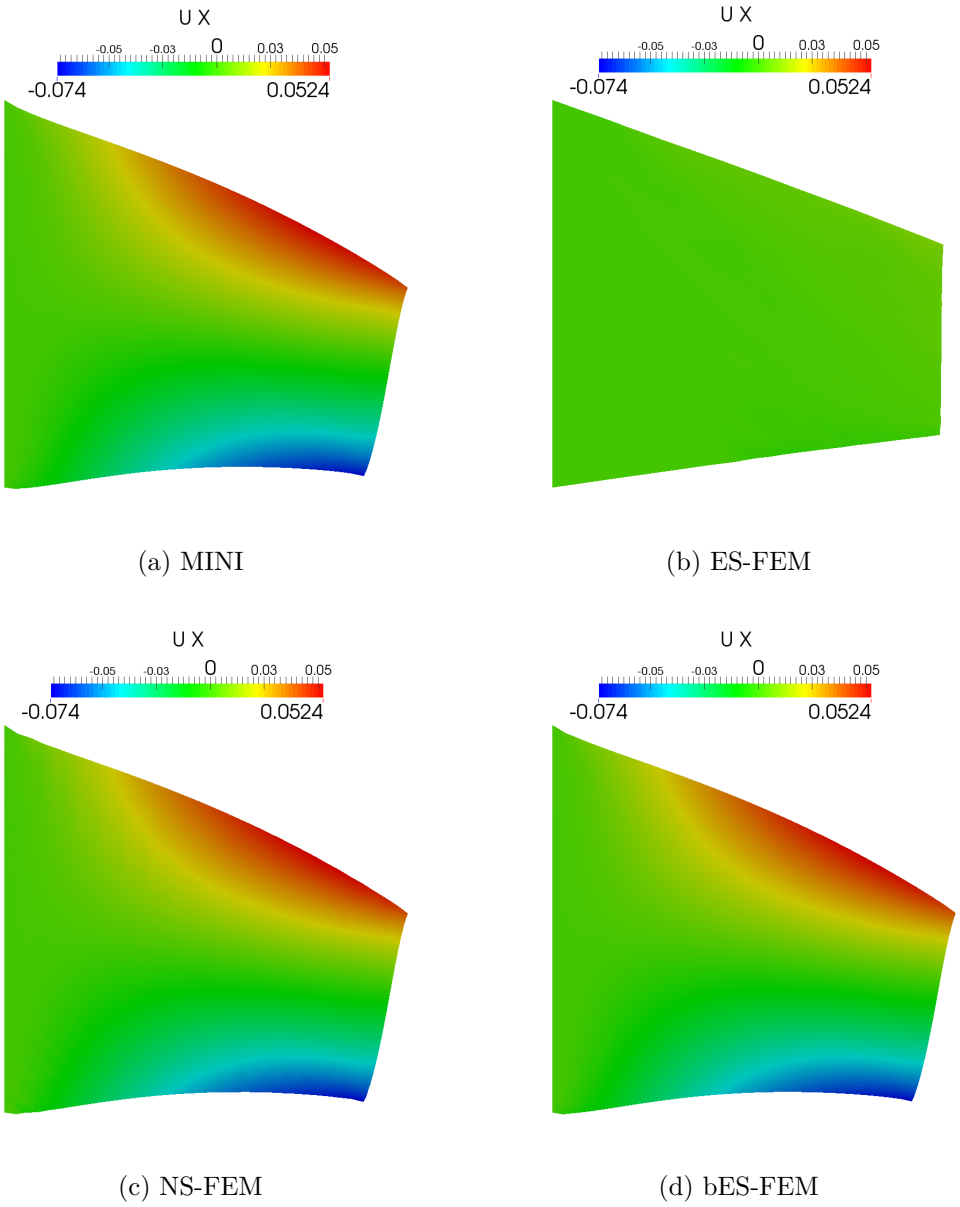

(a) MINI (b) ES-FEM

(c) NS-FEM (d) bES-FEM

Figure 5.26: Deformed shapes for the bevelled beam problem in displacements u_x with distorted meshes $\alpha_{\text{distorted}} = 0.3$ (MINI, ES-FEM, NS-FEM and bES-FEM): (a) MINI, (b) ES-FEM, (c) NS-FEM and (d) bES-FEM. Note that the displacement u_x of ES-FEM is smaller than the MINI, NS-FEM and bES-FEM. Its value is -0.00408 to 0.00846.

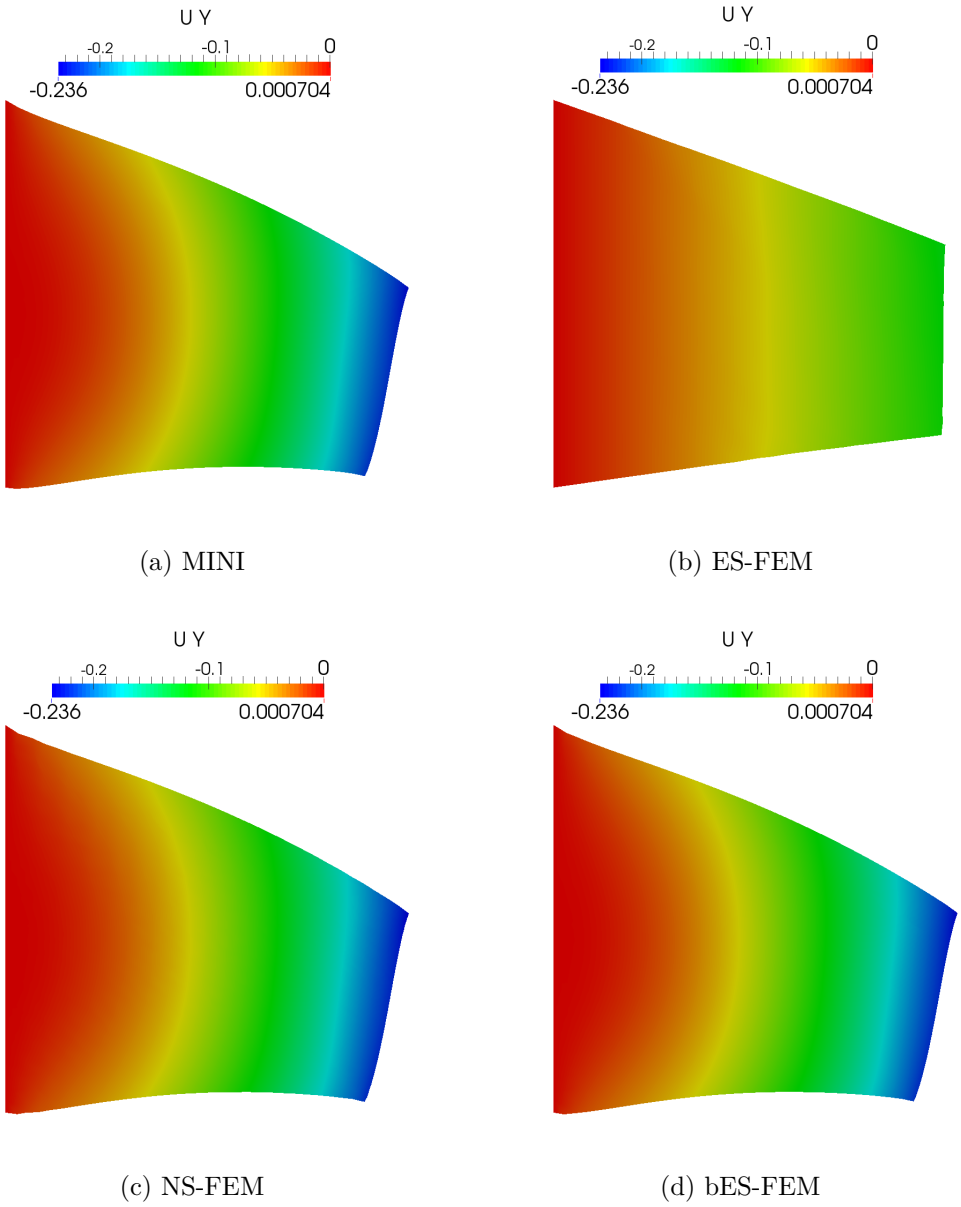

(a) MINI

(b) ES-FEM

(c) NS-FEM

(d) bES-FEM

Figure 5.27: Deformed shapes for the bevelled beam problem in displacements u_x with distorted meshes $\alpha_{\text{distorted}} = 0.3$ (MINI, ES-FEM, NS-FEM and bES-FEM): (a) MINI, (b) ES-FEM, (c) NS-FEM and (d) bES-FEM

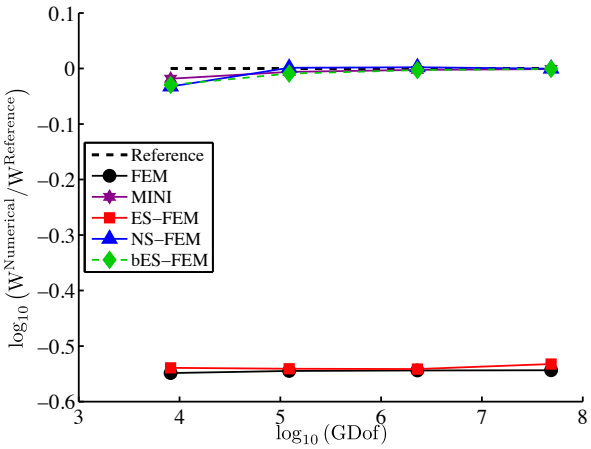

(a) Regular mesh

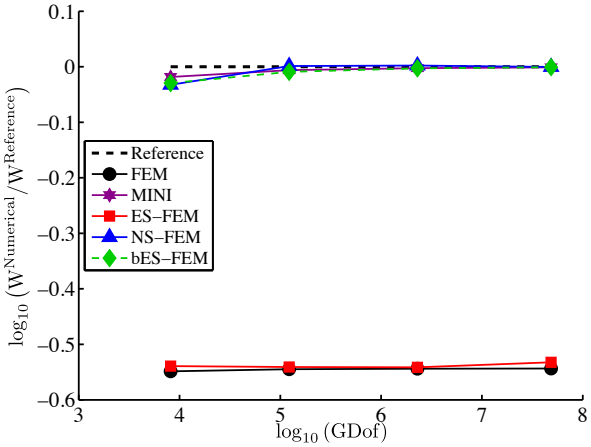

(b) Distorted mesh $\alpha_{\text{distorted}} = 0.1$

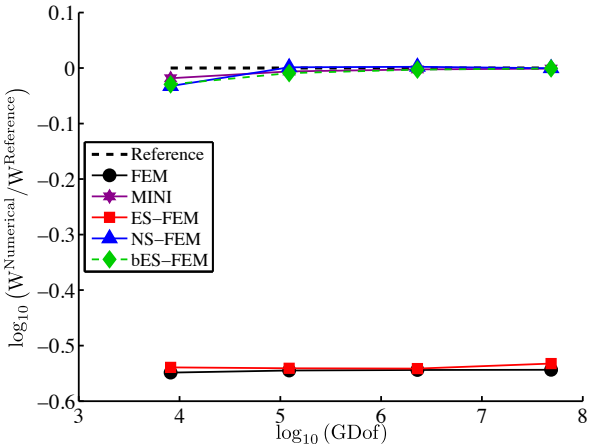

(c) Distorted mesh $\alpha_{\text{distorted}} = 0.3$

Figure 5.28: Strain energy convergence for the bevelled cantilever beam with regular and distorted meshes (FEM, the MINI, ES-FEM, NS-FEM and bES-FEM): (a) regular mesh, (b) distorted mesh $\alpha_{\text{distorted}} = 0.1$ and (c) $\alpha_{\text{distorted}} = 0.3$

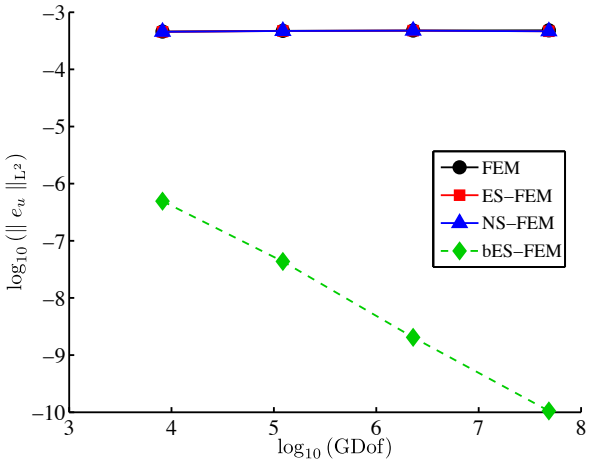

(a) Regular mesh

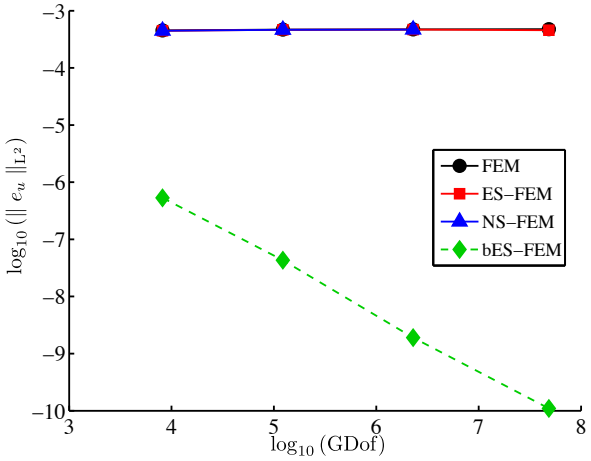

(b) Distorted mesh $\alpha_{\text{distorted}} = 0.1$

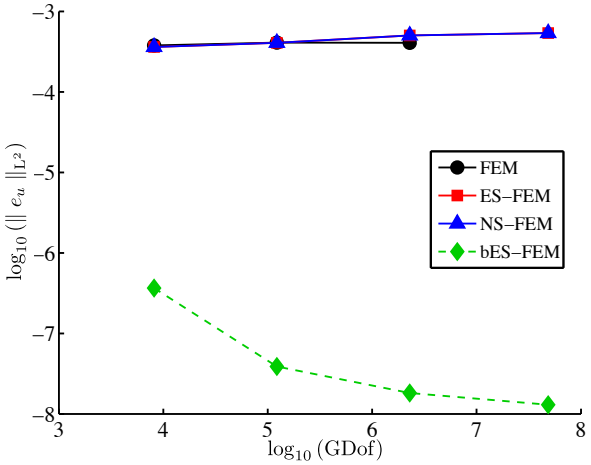

(c) Distorted mesh $\alpha_{\text{distorted}} = 0.3$

Figure 5.29: The logarithm of L2 Norm for the bevelled cantilever beam with regular and distorted meshes (FEM, the MINI, ES-FEM, NS-FEM and bES-FEM): (a) regular mesh, (b) distorted mesh $\alpha_{\text{distorted}} = 0.1$ and (c) $\alpha_{\text{distorted}} = 0.3$

Table 5.13: Strain energy relative error for the bevelled beam (FEM, ES-FEM, NS-FEM, bES-FEM and the MINI)

	FEM	ES-FEM	NS-FEM	bES-FEM	MINI
	Regular mesh				
4×4	-42.2275	-41.6822	-3.2025	-2.9028	-1.8218
8×8	-42.0075	-41.7756	0.1352	-0.9163	-0.6164
16×16	-41.9504	-41.8099	0.2182	-0.2892	-0.2515
32×32	-41.9339	-41.2806	-0.0287	-0.0728	-0.1024
	Distorted mesh $\alpha_{\text{distorted}} = 0.1$				
4×4	-43.1736	-42.6865	-3.2025	-2.9008	-1.8187
8×8	-42.2429	-41.9523	-0.5018	-0.9184	-0.6187
16×16	-42.3178	-42.1163	0.2714	-0.2874	-0.2572
32×32	-42.3472	-41.5833	Fails	-0.0718	-0.1042
	Distorted mesh $\alpha_{\text{distorted}} = 0.3$				
4×4	-43.1602	-42.3768	3.0709	-2.2570	-2.9830
8×8	-42.2698	-42.7838	2.1827	-0.8725	-1.0867
16×16	-43.0153	-46.7746	1.0500	0.0349	-0.6156
32×32	Fails	-48.1337	0.7453	0.2531	-0.3201

Strain energy relative error is given by: $\left(\frac{W^{\text{Numerical}} - W^{\text{Analytical}}}{W^{\text{Analytical}}}\right) \times 100\%$.

5.4 Summary

In this chapter, a new bubble-enriched deformation-gradient smoothing approach was introduced and a selective node/edge based smoothing technique able to preserve the beneficial properties of both edge and node based smoothing (See summary of Chapter 4.4). The behaviour of theses approaches was compared to that of the gold-standard (the MINI element), for finite elasticity problems. The effect of mesh distortion on accuracy was also examined. Tow classes of problem were tackled (1) mesh distortion for compressible finite elasticity; (2) mesh distortion for incompressible finite elasticity. The conclusions, for the selected finite elasticity problems were solved as follows:

- In most cases, bubble-enriched smoothed FEM does not lock and provides similar results of similar accuracy to the gold-standard the MINI element;
- Smoothed FEM handles better severe mesh distortion than the MINI, as it can handle a large amount of distortion before the Newton iterative solution fails to converge.

Consequently, because of its ease of implementation, the bubble-enriched strain gradient smoothing approaches appear promising for large deformation problems involving very large strains.

6 Conclusions

6.1 Conclusions

In this work, a spectrum of gradient smoothing approaches for finite elasticity was presented, developing the smoothed deformation gradient which is an essential part to construct the strain-displacement matrix, the tangent stiffness matrix, the internal force and the fourth-order elasticity tensor in Chapter 4. The transform of "Cubic" bubble function was introduced for strain smoothing approaches in Chapter 5. The employment of the proposed bubble function was shown its ease of implementation into the existing strain smoothing framework without any further mathematical formulations or numerical efforts.

Then the method was tested thoroughly on a number of benchmark problems and compared their performance to both the standard finite element method (FEM) and the gold-standard locking-free element: the MINI element using DOLFIN finite element software. Three specific cases, which can be met when soft matters are being dealt with, were considered as the numerical studies: 1) quasi-incompressibility/incompressibility, 2) mesh distortion sensitivity in compressibility and 3) mesh distortion sensitivity in incompressibility. Such investigation was conducted under highly incompressible condition with severely distorted

meshes, comparing to the psuedo-exact solution obtained by DOLFIN.

Smoothed finite elements may be seen as providing, within a single unified formulation, an intermediate class of elements situated between fast, but potentially inaccurate low-order finite elements. From the numerical experiments which were carried out, the following conclusions can be made:

Homogeneous deformations All methods tested are able to reproduce finite homogeneous deformations to machine precision. If the analytical solution lies in the approximation space, smoothed FEM is able to reproduce it to machine precision.

Locking Most strain smoothing approaches tested are able to alleviate locking. Especially, the node-based smoothing is the most accurate and can deal with severe incompressibility. However, the bubble-enhanced edge-based strain smoothing approach does not lock and provides the almost same accuracy as the MINI element in severe incompressibility.

Mesh distortion Again, strain smoothing alleviates the deleterious effects of mesh distortion to a large extent. The edge-based smoothing is superior to node-based smoothing when dealing with distorted meshes. In particular, the bubble-enriched S-FEM is immune to heavily distorted meshes rather than the MINI element, as it can handle a large amount of distortion before the Newton solution fails to converge.

Selective smoothing By selectively smoothing the volumetric (using node-based smoothing) and deviatoric (using edge-based smoothing) part of the deformation gradient, a compromise between edge and node-based smoothing can be devised, which shares properties of both.

Bubble enhancement With the cooperation of "Cubic" bubble functions, gradient strain smoothing can be easily ameliorated its robustness and stability

in incompressible medium. Particularly, the edge-based strain smoothing with the bubble is shown significant the improvement of accuracy in both incompressibility with mesh distortion and compressibility with mesh distortion.

In the context of computer-aided surgery, which is one of the central activities of Legato research team[1], achieving this would allow to simplify and automate the creation of patient-specific meshes. From the results of numerical experiments carried out in this thesis, bubble-enhanced strain smoothing can be suited to soft tissue simulation since the proposed approach overcome numerous challenges, such as incompressibility, mesh distortion and complex geometries, which are arisen during the simulation. For such realistic applications, the proposed bubble-enriched gradient smoothing approach needs to examine following consideration:

Dynamic approach Explicit integration algorithm allows the element-wise computation in FEM and can avoid solution of large systems of algebraic equations. This step-wise computations are inexpensive, therefore explicit dynamic algorithm can be effectively used for soft tissue simulation.

Parallelisation Since time step computations are performed node-wise and element-wise, the node-based and edge-based SFEM seem well-suited parallelism and easily mapped to parallel hardware. This could be, in particular, looked at within the context of Graphical Processing Units (GPUs).

The long-term aim of research efforts is to enable the use of a wide variety of finite elements, from tetrahedral to polyhedral, which are not subject to locking. Thereby following open research questions need to be answered:

Performance for extremely large deformations The methods was tested up

[1] http://legato-team.eu

to strains of 25% only. It is necessary to investigate much larger deformations, compatible with those arising in surgical practice.

Extension to polyhedral elements Perhaps the most promising aspect of strain smoothing is its ability to deal with arbitrary elements. This work was focused on tetrahedral elements. Now the behaviour of polyhedral elements is investigating and comparing this approach to the Virtual Element Method [100].

Extension to higher-order and enriched non-polynomial approximations It was shown in [24] that higher order polynomial and non-polynomial enriched approximations did not blend well with strain smoothing. This can be related to integration [52, 128]. These problems will be investigated in the context of large deformation finite elasticity.

Comparison and coupling with Arbitrary-Lagrangian-Eulerian (ALE) schemes The proposed method did not been compared to ALE approaches, which is a topic of on-going research in the group. In particular, a coupling of S-FEM and ALE could potentially help reach extreme deformations whilst minimising mesh motion.

6.2 List of publications

The following lists represent the articles published in the Journal, the international and domestic references, respectively.

- Journal papers
  - **C.K. Lee**, L.A. Mihai, J.S. Hale, P. Kerfriden and S.P.A. Bordas. Strain smoothing for compressible and nearly-incompressible finite elasticity. *Computers & Structures*, 2016 (accepted).

  - T.H. Ong, C.E. Heaney, **C.K. Lee**, G.R. Liu, and H. Nguyen-Xuan. On stability, convergence and accuracy of bES-FEM and bFS-FEM for nearly incompressible elasticity. *Computer Methods in Applied Mechanics and Engineering,* 285:315–345, 2015.
  - N. Vu-Bac, H. Nguyen-Xuan, L. Chen, **C.K. Lee**, G. Zi, X. Zhuang, G.R. Liu, and T. Rabczuk. A phantom-node method with edge-based strain smoothing for linear elastic fracture mechanics. *Journal of Applied Mathematics*, 2013, 2013.

- Conference proceedings
  - **C.K. Lee**, L.A. Mihai, P. Kerfriden, and S.P.A. Bordas. Gradient Smoothing for Nearly Incompressible Hyperelasticity. *11th World Congress on Computational Mechanics (WCCM XI)*, 2014.

- Posters
  - **C.K. Lee**, L.A. Mihai, P. Kerfriden, and S.P.A. Bordas. Gradient Smoothing for Nearly Incompressible Hyperelasticity. *SIAM Day Cardiff*, 2014.

- Internal Legato-report
  - **C.K. Lee**, L.A. Mihai, P. Kerfriden and S.P.A. Bordas. Strain smoothing technique in 3D for nearly incompressible neo-Hookean material, 2014 (https://orbilu.uni.lu/handle/10993/15705).
  - **C.K. Lee**, L.A. Mihai and S.P.A. Bordas. The Node-Based Smoothed Finite Element Method in nonlinear elasticity, 2013 (https://orbilu.uni.lu/handle/10993/15391).
  - **C.K. Lee**, S.P.A. Bordas. The Simple Shear and Simple Tension Problems in Linear and Nonlinear Elasticity, 2012 (https://orbilu.uni.lu/handle/10993/15391).

A Elasticity tensor

A.1 Neo-Hookean material

The strain density for a compressible neo-Hookean material [15] is given as

$$\begin{aligned}\mathcal{W}(\mathbf{C}) &= \frac{1}{2}\lambda(\ln J)^2 - \mu \ln J + \frac{1}{2}\mu(\mathrm{tr}\mathbf{C} - 3) \quad \text{or} \\ \mathcal{W}(\mathbf{C}) &= \frac{1}{8}\lambda(\ln I_3)^2 - \frac{1}{2}\mu \ln I_3 + \frac{1}{2}\mu(I_1 - 3)\end{aligned} \tag{A.1}$$

where $J = \det \mathbf{F}$, the deformation gradient is $\mathbf{F}$ and the principal invariants of the right Cauchy strain tensor $\mathbf{C}$ are

$$\begin{aligned}I_1 &= \mathrm{trC} = C_{ij} \\ I_2 &= \frac{1}{2}\left\{\mathrm{tr}\mathbf{C}^2 - \mathrm{tr}\left(\mathbf{C}^2\right)\right\} = \frac{1}{2}\left\{(C_{ii})^2 - C_{ij}C_{ji}\right\} \\ I_3 &= \det \mathbf{C} = \epsilon_{ijkl}C_{i1}C_{j2}C_{k3}\end{aligned} \tag{A.2}$$

Expressing the first derivatives of strain density with respect to $\mathbf{C}$, by the chain rule, the second Piola-Kirchhoff stress is given by

$$\begin{aligned}\mathbf{S} &= 2\frac{\partial \mathcal{W}}{\partial \mathbf{C}} = 2\left(\frac{\partial \mathcal{W}}{\partial I_1}\frac{\partial I_1}{\partial \mathbf{C}} + \frac{\partial \mathcal{W}}{\partial I_2}\frac{\partial I_2}{\partial \mathbf{C}} + \frac{\partial \mathcal{W}}{\partial I_3}\frac{\partial I_3}{\partial \mathbf{C}}\right) \\ &= 2\left(\frac{\partial \mathcal{W}}{\partial I_1} + I_1\frac{\partial \mathcal{W}}{\partial I_2}\right)\mathbf{I} - 2\frac{\partial \mathcal{W}}{\partial I_2}\mathbf{C} + 2I_3\frac{\partial \mathcal{W}}{\partial I_3}\mathbf{C}^{-1}\end{aligned} \tag{A.3}$$

The derivatives of the stored strain density with respect to the principal invariants are

$$\begin{aligned}\frac{\partial \mathcal{W}}{\partial I_1} &= \frac{1}{2}\mu \\ \frac{\partial \mathcal{W}}{\partial I_2} &= 0 \\ \frac{\partial \mathcal{W}}{\partial I_3} &= \frac{1}{4}\lambda \ln I_3 I_3^{-1} - \frac{1}{2}\mu I_3^{-1}\end{aligned} \tag{A.4}$$

The derivatives of the principal invariants of the right Cauchy strain tensor with respect to the tensor itself can be described as follows

$$\begin{aligned}\frac{\partial I_1}{\partial \mathbf{C}} &= \frac{\partial C_{kk}}{\partial C_{ij}} = \delta_{ki}\delta_{kj} \\ &= \sum_k \delta_{ki}\delta_{kj} = \sum_k \delta_{ik}\delta_{kj} = \mathbf{I}\cdot\mathbf{I} = \mathbf{I}\end{aligned} \tag{A.5}$$

$$\begin{aligned}2\frac{\partial I_2}{\partial \mathbf{C}} &= \frac{\partial}{\partial C_{ij}}\left(C_{ij}^2 - C_{pg}C_{qp}\right) \\ &= 2\frac{\partial C_{kk}}{\partial C_{ij}}C_{kk} - \left(\frac{\partial C_{pq}}{\partial C_{ij}}C_{qp} + C_{pq}\frac{\partial C_{pq}}{\partial C_{ij}}\right) \\ &= 2\,\mathbf{I}\,\mathrm{tr}\mathbf{C} - (\delta_{pi}\delta_{qi}C_{qp} + C_{pq}\delta_{qi}\delta_{pi}) \\ &= 2\,\mathbf{I}\,\mathrm{tr}\mathbf{C} - (C_{ji} + C_{ji})\end{aligned} \tag{A.6}$$

hence,

$$\begin{aligned}\frac{\partial I_2}{\partial \mathbf{C}} &= \mathbf{I}\,\mathrm{tr}\mathbf{C} - C - ji \\ &= \mathbf{I}\,(\mathbf{C}) - \mathbf{C}^{\mathrm{T}} = \mathbf{I}\,(\mathbf{C}) - \mathbf{C}\end{aligned} \tag{A.7}$$

and

$$\frac{\partial I_3}{\partial \mathbf{C}} = \begin{bmatrix} C_{22}C_{33} - C_{32}C_{23} & C_{31}C_{23} - C_{21}C_{33} & C_{21}C_{32} - C_{31}C_{22} \\ & C_{11}C_{33} - C_{31}C_{13} & C_{31}C_{12} - C_{11}C_{21} \\ \text{symm.} & & C_{11}C_{22} - C_{21}C_{12} \end{bmatrix}$$

since

$$\begin{aligned}\mathbf{C}^{-1} &= \begin{bmatrix} C_{11} & C_{12} & C_{13} \\ C_{21} & C_{22} & C_{23} \\ C_{31} & C_{32} & C_{33} \end{bmatrix}^{-1} \\ &= \frac{1}{\det \mathbf{C}} \begin{bmatrix} C_{22}C_{33} - C_{32}C_{23} & C_{31}C_{23} - C_{21}C_{33} & C_{21}C_{32} - C_{31}C_{22} \\ & C_{11}C_{33} - C_{31}C_{13} & C_{31}C_{12} - C_{11}C_{21} \\ \text{symm.} & & C_{11}C_{22} - C_{21}C_{12} \end{bmatrix}\end{aligned}$$

it follows that

$$\frac{\partial I_3}{\mathbf{C}} = (\det \mathbf{C})\,\mathbf{C}^{-1} = I_3\mathbf{C}^{-1} \tag{A.8}$$

Substituting Eqs. (A.4), (A.5), (A.6), (A.7) and (A.8) into Eq. (A.3), we can obtain the 2nd Piola-Kirchhoff stress as following

$$\begin{aligned}\mathbf{S} &= \mu\left(\mathbf{I} - \mathbf{C}^{-1}\right) + \frac{1}{2}\lambda \ln I_3 \mathbf{C}^{-1} \\ &= \mu\left(\mathbf{I} - \mathbf{C}^{-1}\right) + \lambda \ln J \mathbf{C}^{-1}\end{aligned} \tag{A.9}$$

The Lagrangian elasticity tensor is given by

$$\mathbb{C} = 2\frac{\partial \mathbf{S}}{\partial \mathbf{C}} = 2\frac{\partial}{\partial \mathbf{C}}\left(2\frac{\partial \mathcal{W}}{\partial \mathbf{C}}\right) = 4\frac{\partial}{\partial \mathbf{C}}\left(\frac{\partial \mathcal{W}}{\partial \mathbf{C}}\right) \tag{A.10}$$

With the first derivatives of strain density with respect to the principal invariants and the derivatives of the principal invariants of $\mathbf{C}$ with respect to itself, Eq. (A.10) can be re-expressed as

$$\begin{aligned}
\mathbb{C} &= 4\frac{\partial}{\partial \mathbf{C}}\left[\frac{1}{2}\mu\mathbf{I} + I_3\left(\frac{1}{4}\lambda \ln I_3 I_3^{-1} - \frac{1}{2}\mu I_3^{-1}\right)\mathbf{C}^{-1}\right] \\
&= 4\frac{\partial I_3}{\partial \mathbf{C}}\left[\frac{1}{4}\lambda \ln I_3 I_3^{-1} - \frac{1}{2}\mu I_3^{-1}\right]\mathbf{C}^{-1} \\
&+ 4I_3\frac{\partial}{\partial \mathbf{C}}\left[\frac{1}{4}\lambda \ln I_3 I_3^{-1} - \frac{1}{2}\mu I_3^{-1}\right]\mathbf{C}^{-1} \\
&+ 4I_3\left[\frac{1}{4}\lambda \ln I_3 I_3^{-1} - \frac{1}{2}\mu I_3^{-1}\right]\frac{\partial \mathbf{C}^{-1}}{\partial \mathbf{C}}
\end{aligned} \tag{A.11}$$

The first term of right hand side of Eq. (A.11) is

$$\begin{aligned}
&4\frac{\partial I_3}{\partial \mathbf{C}}\left[\frac{1}{4}\lambda \ln I_3 I_3^{-1} - \frac{1}{2}\mu I_3^{-1}\right] \otimes \mathbf{C}^{-1} \\
&= 4I_3\left[\frac{1}{4}\lambda \ln I_3 I_3^{-1} - \frac{1}{2}\mu I_3^{-1}\right]\mathbf{C}^{-1} \otimes \mathbf{C}^{-1} \\
&= \lambda \ln I_3 \mathbf{C}^{-1} \otimes \mathbf{C}^{-1} - 2\mu \mathbf{C}^{-1} \otimes \mathbf{C}^{-1}
\end{aligned} \tag{A.12}$$

, the second term is

$$\begin{aligned}
&4I_3\frac{\partial}{\partial \mathbf{C}}\left[\frac{1}{4}\lambda \ln I_3 I_3^{-1} - \frac{1}{2}\mu I_3^{-1}\right] \otimes \mathbf{C}^{-1} \\
&= 4I_3\left[I_3\left(\frac{1}{4}\lambda I_3^{-1} - \frac{1}{4}\lambda \ln I_3 I_3^{-2} + \frac{1}{2}\mu I_3^{-1}\right)\mathbf{C}^{-1}\right] \otimes \mathbf{C}^{-1} \\
&= \lambda \mathbf{C}^{-1} \otimes \mathbf{C}^{-1} - \lambda \ln I_3 \mathbf{C}^{-1} \otimes \mathbf{C}^{-1} + 2\mu \mathbf{C}^{-1} \otimes \mathbf{C}^{-1}
\end{aligned} \tag{A.13}$$

and the last term is

$$4I_3\left[\frac{1}{4}\lambda \ln I_3 I_3^{-1} - \frac{1}{2}\mu I_3^{-1}\right]\frac{\partial \mathbf{C}^{-1}}{\partial \mathbf{C}} = (\lambda \ln I_3 - 2\mu)\,\boldsymbol{\mathcal{I}} \tag{A.14}$$

where $\mathbf{C}^{-1} \otimes \mathbf{C}^{-1}$ and the fourth-order tensor $\boldsymbol{\mathcal{I}}$ are given in [21]

$$\mathbf{C}^{-1} \otimes \mathbf{C}^{-1} = \sum \left(C^{-1}\right)_{ij} \left(C^{-1}\right)_{kl} E_i \otimes E_j \otimes E_k \otimes E_l \tag{A.15}$$

and

$$\boldsymbol{\mathcal{I}} = -\frac{\partial \mathbf{C}^{-1}}{\partial \mathbf{C}}, \quad \text{or} \quad \mathcal{I}_{ijkl} = -\frac{\partial \left(C^{-1}\right)_{ij}}{\partial C_{kl}} \tag{A.16}$$

Hence, the components of the tensor $\boldsymbol{\mathcal{I}}$ can be written as

$$I_{ijkl} = \frac{1}{2}\left[\left(C^{-1}\right)_{ik}\left(C^{-1}\right)_{jl} + \left(C^{-1}\right)_{il}\left(C^{-1}\right)_{jk}\right] \tag{A.17}$$

Consequently, the fourth-order elasticity tensors of Eq. (A.10) in component form are

$$\begin{aligned} \mathbb{C}_{ijkl} &= \lambda\left(C^{-1}_{ij}C^{-1}_{kl}\right) + \left(\mu - \frac{1}{2}\lambda \ln I_3\right)\left[C^{-1}_{ik}C^{-1}_{jl} + C^{-1}_{il}C^{-1}_{jk}\right], \quad \text{or} \\ \mathbb{C}_{ijkl} &= \lambda\left(C^{-1}_{ij}C^{-1}_{kl}\right) + (\mu - \lambda \ln J)\left[C^{-1}_{ik}C^{-1}_{jl} + C^{-1}_{il}C^{-1}_{jk}\right] \end{aligned} \tag{A.18}$$

where the Lamé's first parameter is $\lambda = \kappa - \frac{2}{3}\mu$ with the shear modulus μ and the bulk modulus κ.

B Smoothed deformation gradient

If the deformation gradient $\mathbf{F}$ is homogeneous on an element, the displacement field on a single element can be explained as following

$$\mathbf{u}(\mathbf{X}) = \begin{bmatrix} u_1(\mathbf{X}) \\ u_2(\mathbf{X}) \end{bmatrix} = \begin{bmatrix} a_{11}X_1 + a_{12}X_2 + b_1 \\ a_{21}X_1 + a_{22}X_2 + b_2 \end{bmatrix} \tag{B.1}$$

where the undetermined coefficients a_{ij} and b_i, where $i, j \in \{1, 2\}$, are constant. We here consider the smoothed deformation gradient $\tilde{\mathbf{F}}$ for ES-FEM. The deformation gradient on a triangle $\triangle ABC$ for the standard FEM in Fig. B.1 is

$$\mathbf{F} = \begin{bmatrix} a_{11}+1 & a_{12} \\ a_{21} & a_{22}+1 \end{bmatrix} = \begin{bmatrix} \left(u_1^B - u_1^A\right)/h + 1 & \left(u_1^C - u_1^A\right)/h \\ \left(u_2^B - u_2^A\right)/h & \left(u_2^C - u_2^A\right)/h + 1 \end{bmatrix} \tag{B.2}$$

For the smoothed deformation gradient $\tilde{\mathbf{F}}$ in the smoothing domain Ω_k in Fig. B.1, the deformation gradient in the smoothing domain Ω_k^1 can be expressed as following

$$\begin{aligned} u_1(\mathcal{O}_1) &= \frac{1}{3}\left(u_1^A + u_1^B + u_1^C\right) \\ u_2(\mathcal{O}_2) &= \frac{1}{3}\left(u_2^A + u_2^B + u_2^C\right) \end{aligned} \tag{B.3}$$

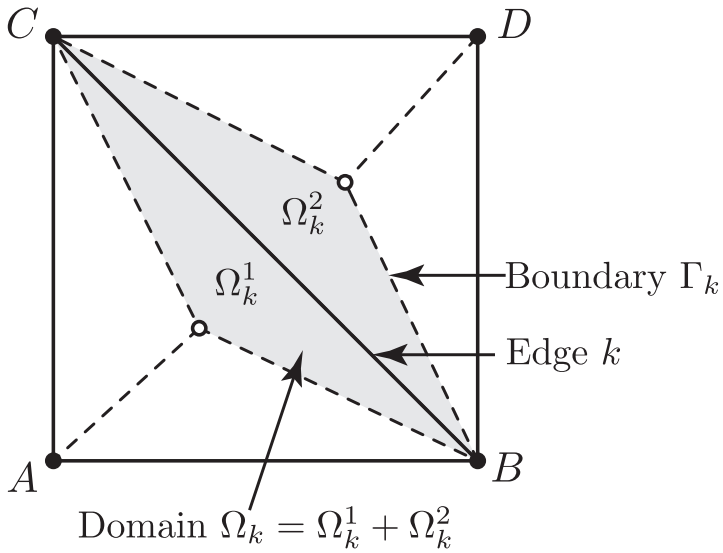

(a) Smoothing domain associated with target edge k in ES-FEM

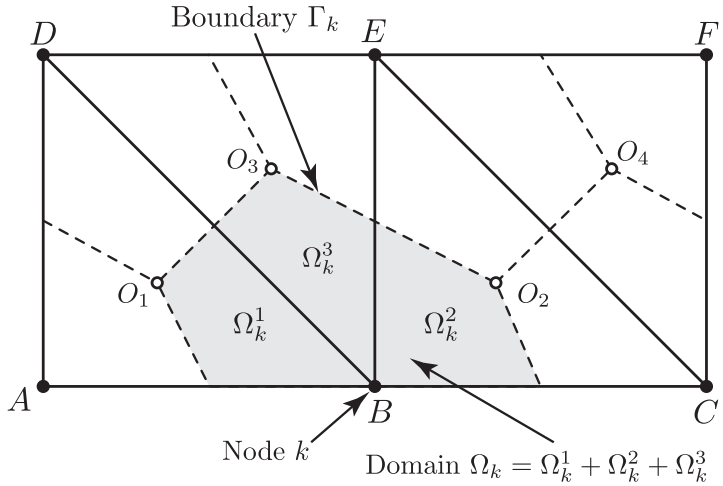

(b) Smoothing domain associated with target node k in NS-FEM

Figure B.1: Smoothing domains associated with target edge k for ES-FEM and target node k for NS-FEM to assemble the smoothed deformation gradient $\tilde{\mathbf{F}}$

Substituting Eq. (B.3) into Eq. (B.1), the displacement field on mid-point $\mathcal{O}_1$ is given by

$$\begin{aligned} \frac{1}{3}\left(u_1^A + u_1^B + u_1^C\right) &= a_{11}\frac{h}{3} + a_{12}\frac{h}{3} + b_1 \\ \frac{1}{3}\left(u_2^A + u_2^B + u_2^C\right) &= a_{21}\frac{h}{3} + a_{22}\frac{h}{3} + b_2 \end{aligned} \tag{B.4}$$

Similarly, the displacement fields on node B and C can be written as

$$u_1^B = a_{11}h + b_1, \quad u_2^B = a_{21}h + b_2 \tag{B.5}$$

and

$$u_1^C = a_{12}h + b_1, \quad u_2^C = a_{22}h + b_2 \tag{B.6}$$

Substituting Eq. (B.6) into Eq. (B.5), $a_{11} - a_{12}$ and $a_{21} - a_{22}$ can be obtained as

$$a_{11} - a_{12} = \frac{u_1^B - u_1^C}{h}, \quad a_{21} - a_{22} = \frac{u_2^B - u_2^C}{h} \tag{B.7}$$

Hence, the displacements on the mid-point $\mathcal{O}_1$ are given by

$$\begin{aligned} u_1^A + u_1^B + u_1^C &= a_{11}h + a_{12}h + 3\left(u_1^C - a_{12}h\right) \\ u_2^A + u_2^B + u_2^C &= a_{21}h + a_{22}h + 3\left(u_2^C - a_{22}h\right) \end{aligned} \tag{B.8}$$

From Eq. (B.8), the undetermined coefficients a_{ij} are defined as follows

$$a_{11} = \frac{u_1^B - u_1^A}{h}, \quad a_{12} = \frac{u_1^C - u_1^A}{h}, \quad a_{21} = \frac{u_2^B - u_2^A}{h}, \quad a_{22} = \frac{u_2^C - u_2^A}{h} \tag{B.9}$$

Similarly, the undetermined coefficients a_{ij} for triangle $\triangle DCB$ in Fig. B.1 are given by

$$a_{11} = \frac{u_1^C - u_1^D}{h}, \quad a_{12} = \frac{u_1^B - u_1^D}{h}, \quad a_{21} = \frac{u_2^C - u_2^D}{h}, \quad a_{22}\frac{u_2^B - u_2^D}{h} \tag{B.10}$$

The smoothed deformation gradient is given by Hu et al. [64]

$$\begin{aligned} \tilde{F}_{ij}(\mathbf{x}) &= \frac{1}{A_k}\int_{\Omega_k} F_{ij}(\mathbf{x}_k)\,\Phi(\mathbf{x}_k)\,\mathrm{d}\Omega \\ &= \frac{1}{A_k}\int_{\Omega_k} \left(\frac{\partial u_i^h}{\partial X_j}\right)\Phi(\mathbf{x}_k)\,\mathrm{d}\Omega + \delta_{ij} \end{aligned} \tag{B.11}$$

where Φ is

$$\Phi = \begin{cases} \dfrac{1}{A_k} & \mathbf{x} \in \Omega_k \\ 0 & \text{otherwise} \end{cases} \tag{B.12}$$

and then,

$$\begin{aligned}
\tilde{F}_{11} &= \frac{1}{A_k}\left\{\int_{\Omega_k^1}\frac{\partial u_1^{\mathrm{h}}}{\partial X_1}\mathrm{d}\Omega + \int_{\Omega_k^2}\frac{\partial u_1^{\mathrm{h}}}{\partial X_1}\mathrm{d}\Omega\right\} + 1 = \frac{3}{h^2}\left(a_{11}\frac{h^2}{6} + a_{11}^2\frac{h^2}{6}\right) + 1 \\
\tilde{F}_{12} &= \frac{1}{A_k}\left\{\int_{\Omega_k^1}\frac{\partial u_1^{\mathrm{h}}}{\partial X_2}\mathrm{d}\Omega + \int_{\Omega_k^2}\frac{\partial u_1^{\mathrm{h}}}{\partial X_2}\mathrm{d}\Omega\right\} = \frac{3}{h^2}\left(a_{12}^1\frac{h^2}{6} + a_{12}^2\frac{h^2}{6}\right) \\
\tilde{F}_{21} &= \frac{1}{A_k}\left\{\int_{\Omega_k^1}\frac{\partial u_2^{\mathrm{h}}}{\partial X_1}\mathrm{d}\Omega + \int_{\Omega_k^2}\frac{\partial u_2^{\mathrm{h}}}{\partial X_1}\mathrm{d}\Omega\right\} = \frac{3}{h^2}\left(a_{21}^1\frac{h^2}{6} + a_{21}^2\frac{h^2}{6}\right) \\
\tilde{F}_{22} &= \frac{1}{A_k}\left\{\int_{\Omega_k^1}\frac{\partial u_2^{\mathrm{h}}}{\partial X_2}\mathrm{d}\Omega + \int_{\Omega_k^2}\frac{\partial u_2^{\mathrm{h}}}{\partial X_2}\mathrm{d}\Omega\right\} + 1 = \frac{3}{h^2}\left(a_{22}\frac{h^2}{6} + a_{22}^2\frac{h^2}{6}\right) + 1
\end{aligned} \tag{B.13}$$

where $A_k = A_k^1 + A_k^2 = \dfrac{h^2}{6} + \dfrac{h^2}{6} = \dfrac{h^2}{3}$, and the matrix form is

$$\tilde{\mathbf{F}} = \begin{bmatrix} \dfrac{1}{2}\left(\dfrac{u_1^B - u_1^A}{h} + \dfrac{u_1^C - u_1^D}{h}\right) + 1 & \dfrac{1}{2}\left(\dfrac{u_1^C - u_1^A}{h} + \dfrac{u_1^B - u_1^D}{h}\right) \\ \dfrac{1}{2}\left(\dfrac{u_2^B - u_2^A}{h} + \dfrac{u_2^C - u_2^D}{h}\right) & \dfrac{1}{2}\left(\dfrac{u_2^C - u_2^A}{h} + \dfrac{u_2^B - u_2^D}{h}\right) + 1 \end{bmatrix} \tag{B.14}$$

In case of the edge in on the boundary, the smoothed deformation gradient $\tilde{\mathbf{F}}$ can be described as follows

$$\tilde{\mathbf{F}} = \begin{bmatrix} \dfrac{1}{2}\left(\dfrac{u_1^B - u_1^A}{h} + \dfrac{u_1^C - u_1^D}{h}\right) + 1 & \dfrac{1}{2}\left(\dfrac{u_1^C - u_1^A}{h} + \dfrac{u_1^B - u_1^D}{h}\right) \\ \dfrac{1}{2}\left(\dfrac{u_2^B - u_2^A}{h} + \dfrac{u_2^C - u_2^D}{h}\right) & \dfrac{1}{2}\left(\dfrac{u_2^C - u_2^A}{h} + \dfrac{u_2^B - u_2^D}{h}\right) + 1 \end{bmatrix} \tag{B.15}$$

C Imposing Dirichlet and Neumann boundary conditions

C.1 Simple shear deformation

The deformation gradient $\mathbf{F}$ for simple shear deformation is

$$\mathbf{F} = \begin{bmatrix} 1 & k & 0 \\ 0 & 1 & 0 \\ 0 & 0 & 1 \end{bmatrix} \tag{C.1}$$

where $k > 0$. The strain invariants for this deformation are given as

$$I_1 = k^2 + 3 = I_2, \quad I_3 = 1 \tag{C.2}$$

The non-zero entries of the corresponding Cauchy stress tensors are given in References [47, 97]

$$\begin{aligned} \sigma_{11} &= \beta_0 + \beta_1 \left(1 + k^2\right) + \beta_{-1} \\ \sigma_{22} &= \beta_0 + \beta_1 + \beta_{-1} \left(1 + k^2\right) \\ \sigma_{33} &= \beta_0 + \beta_1 + \beta_{-1} \\ \sigma_{12} &= k \left(\beta_1 - \beta_{-1}\right) \end{aligned} \tag{C.3}$$

where β_0, β_1 and β_{-1} are

$$\begin{aligned} \beta_0 &= 2\frac{\partial \mathcal{W}}{\partial I_3} = -\mu \\ \beta_1 &= 2\frac{\partial \mathcal{W}}{\partial I_1} = \mu \\ \beta_{-1} &= 0 \end{aligned} \tag{C.4}$$

Hence, by Eq. (C.4), Eq. (C.3) can be written

$$\begin{aligned} \sigma_{11} &= k^2\mu \\ \sigma_{22} &= \sigma_{33} = 0 \\ \sigma_{12} &= k\mu \end{aligned} \tag{C.5}$$

The first Piola-Kirchhoff stress tensor is then computed as

$$\mathbf{P} = \begin{bmatrix} \sigma_{11} - k\sigma_{12} & \sigma_{12} & 0 \\ \sigma_{12} - k\sigma_{22} & \sigma_{22} & 0 \\ 0 & 0 & \sigma_{33} \end{bmatrix} \tag{C.6}$$

Dirichlet boundary conditions. Prescribed displacement boundary conditions are imposed on all edges such that:

- All edges: $(u_1, u_2) = (kX_2, 0)$.

Fig. C.1 shows the deformed shapes provided by FEM and S-FEM.

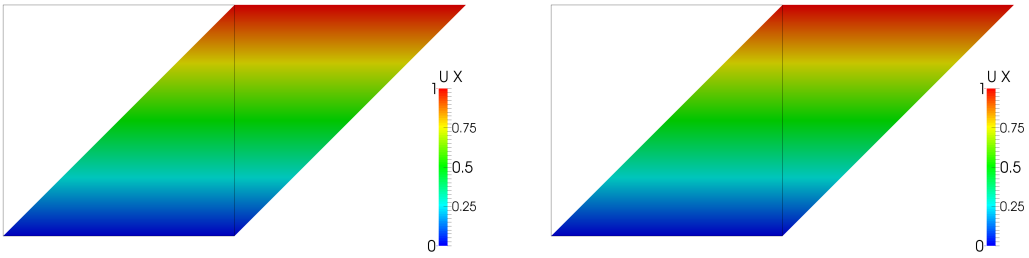

(a) FEM (b) Smoothed FEM

Figure C.1: Deformed shapes for the simple shear deformation with Dirichlet BCs (FEM and S-FEM with T3 32×32 elements)

Neumann boundary conditions. A zero prescribed displacement boundary condition is imposed on the bottom edge, tensions in the vertical direction are imposed on the left- and right-hand side edges and tension in the horizontal direction is imposed on the top edge. Neumann BCs imposed on particular edges are given as

- Top edge: $(P_1, P_2) = (\sigma_{12}, \sigma_{22})$
- Left-hand side edge: $(P_1, P_2) = (-\sigma_{11} + k\sigma_{12}, -\sigma_{12} + k\sigma_{22})$
- Right-hand side edge: $(P_1, P_2) = (\sigma_{11} - k\sigma_{12}, \sigma_{12} - k\sigma_{22})$

where stresses imposed on top, left-hand and right-hand edges are

$$\begin{aligned} \sigma_{11} &= \beta_0 + \beta_1 \left(1 + k^2\right) + \beta_{-1} = -\mu + 2\mu = \mu \\ \sigma_{22} &= \beta_0 + \beta_1 + \beta_{-1} \left(1 + k^2\right) = -\mu + \mu = 0 \\ \sigma_{12} &= k \left(\beta_1 - \beta_{-1}\right) = \mu \end{aligned} \tag{C.7}$$

Fig. C.2 depicts the current configurations of FEM and S-FEM.

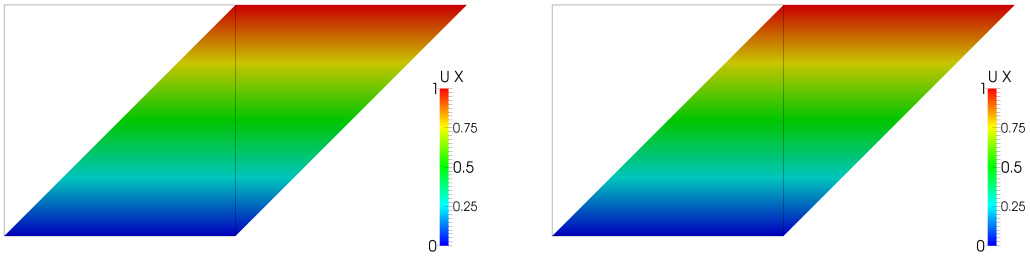

(a) FEM (b) S-FEM

Figure C.2: Deformed shapes for the simple shear deformation with mixed Dirichlet and Neumann BCs (FEM and S-FEM with T3 32×32 elements)

C.2 Uniform extension with lateral contraction

The following triaxial stretches are defined for the deformation gradient for the uniform extension with lateral contraction problem:

$$x_1 = \lambda_1 X_1, \quad x_2 = \lambda_2 X_2, \quad x_3 = \lambda_3 \lambda_3 X_3 \tag{C.8}$$

where $\mathbf{X} = [X_1, X_2, X_3]^{\mathrm{T}}$ and $\mathbf{x} = [x_1, x_2, x_3]^{\mathrm{T}}$ respectively denote the reference and current configurations and $\lambda_i > 0$, $i \in \{1, 2, 3\}$, are positive constants. Hence, the deformation gradient is

$$\mathbf{F} = \begin{bmatrix} \lambda_1 & 0 & 0 \\ 0 & \lambda_2 & 0 \\ 0 & 0 & \lambda \end{bmatrix} \tag{C.9}$$

For the triaxial deformation, the strain invariants of the left Cauchy-Green tensor ($\mathbf{B} = \mathbf{F}\mathbf{F}^{\mathrm{T}}$) are

$$\begin{aligned} I_1(\mathbf{B}) &= \lambda_1^2 + \lambda_2^2 + \lambda_3^2 \\ I_2(\mathbf{B}) &= \lambda_1^2\lambda_2^2 + \lambda_2^2\lambda_3^2 + \lambda_3^2\lambda_1^2 \\ I_3(\mathbf{B}) &= \lambda_1^2\lambda_2^2\lambda_3^2 \end{aligned} \tag{C.10}$$

In particular, if the deformation is isochoric (preserves volume), then $I_3(\mathbf{B}) = 1$. The triaxial deformation associated with a square section of the material is obtained by setting $\lambda_3 = 1$. $\lambda_2 = 1/\lambda_1$ in this case due to the fact that the deformation is isochoric and then the strain invariants are given as

$$I_1 = \mathrm{tr}\mathbf{B} = \lambda_1^2 + \frac{1}{\lambda_1^2} + 1 = I_2, \quad I_3 = \det\mathbf{B} = 1 \tag{C.11}$$

The general form of Cauchy stress can be expressed in terms of left Cauchy-Green tensor $\mathbf{B}$ as follows

$$\boldsymbol{\sigma} = \beta_0\mathbf{I} + \beta_1\mathbf{B} + \beta_{-1}\mathbf{B}^{-1} \tag{C.12}$$

with the elastic response coefficients β_0, β_1 and β_{-1} defined as

$$\begin{aligned} \beta_0 &= \frac{2}{\sqrt{I_3}}\left(I_2\frac{\partial\mathcal{W}}{\partial I_2} + I_3\frac{\partial\mathcal{W}}{\partial I_3}\right) \\ \beta_1 &= \frac{2}{\sqrt{I_3}}\frac{\partial\mathcal{W}}{\partial I_1} \\ \beta_{-1} &= -2\sqrt{I_3}\frac{\partial\mathcal{W}}{\partial I_2} \end{aligned} \tag{C.13}$$

In particular, the non-zero components of the Cauchy stress are represented as

$$\begin{aligned}\sigma_{11} &= \beta_0 + \beta_1\lambda_1^2 + \beta_{-1}\frac{1}{\lambda_1^2}\\ \sigma_{22} &= \beta_0 + \beta_1\frac{1}{\lambda_1^2} + \beta_{-1}\lambda_1^2\\ \sigma_{33} &= \beta_0 + \beta_1 + \beta_{-1}\end{aligned} \tag{C.14}$$

where

$$\beta_0 = 2\frac{\partial \mathcal{W}}{\partial I_3} = -\mu, \quad \beta_1 = 2\frac{\partial \mathcal{W}}{\partial I_1} = \mu, \quad \beta_{-1} = 0 \tag{C.15}$$

Therefore the non-zero components of the Cauchy stress can be expressed as

$$\sigma_{11} = \mu\left(\lambda_1^2 - 1\right), \quad \sigma_{22} = \mu\left(\frac{1}{\lambda_1^2} - 1\right) \tag{C.16}$$

Dirichlet boundary conditions. To obtain the triaxial stretch of a square section, assuming that sides of the square are aligned with the direction X and Y, and the bottom left-hand corner is at the origin $\mathcal{O}(0,0)$, then Dirichlet BCs are imposed as

- Bottom edge: $(u_1, u_2) = ((\lambda_1 - 1)X_1, 0)$
- Left-hand side edge: $(u_1, u_2) = (0, (1/\lambda_1 - 1)X_2)$
- Top and right-hand side edges: $(u_1, u_2) = ((\lambda_1 - 1)X_1, (1/\lambda_1 - 1)X_2)$

Fig. C.3 illustrates the deformed shapes of FEM and S-FEM respectively.

Neumann boundary conditions. Alternatively, Neumann BCs can be imposed on some of edges. For Neumann BCs, the first Piola-Kirchhoff stress tensor

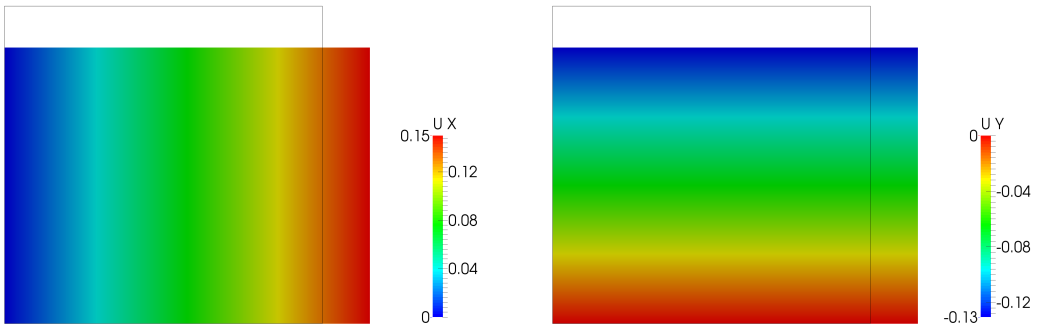

(a) FEM (u_x) (b) FEM (u_y)

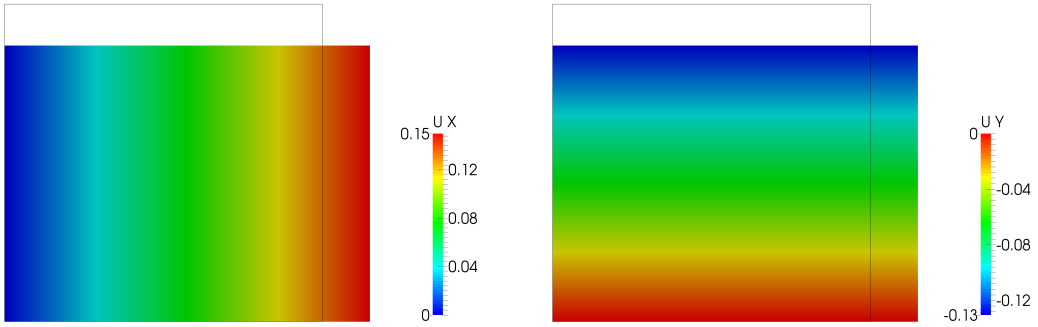

(c) Smoothed FEM (u_x) (d) Smoothed FEM (u_y)

Figure C.3: Deformed shapes for the uniform extension with lateral contraction with Dirichlet BCs (FEM and S-FEM with T3 32×32 elements)

is given as

$$\mathbf{P} = \boldsymbol{\sigma}(\mathbf{F}) = \sigma J \mathbf{F}^{-\mathrm{T}} \tag{C.17}$$

The non-zero components of the first Piola-Kirchhoff stress tensor with stretches $\lambda_2 = 1/\lambda_1$ and $\lambda_3 = 1$ can be calculated as

$$P_{11} = \frac{\sigma_{11}}{\lambda_1} = \mu \left(\lambda_1 - \frac{1}{\lambda_1} \right) = -P_{22} \tag{C.18}$$

- Top edge: $(P_1, P_2) = (0, -P_{22})$

- Right-hand side edge: $(P_1, P_2) = (P_{11}, 0)$

Zero Dirichlet BCs (prescribed displacements are zero) in the vertical direction on bottom edge and zero Dirichlet BCs in horizontal axis on left-hand side edge are imposed and consequently the left-hand sided of corner is to be zero Dirichlet BCs in both horizontal and vertical directions.

Since $\lambda_1 = 1.15$ is considered in this test with mixed Dirichlet and Neumann BCs, the first Piola-Kirchhoff stress tensors P_{11} and P_{22} are $P_{11} = -P_{22} = 0.16826087$. The strain energy for this problem is $\mathcal{W} \approx 0.02359$ with shear modulus $\mu = 0.6$ and bulk modulus $\kappa = 100$, respectively (see also Appendix D.2).

Deformed shapes of FEM and S-FEM with mixed Dirichlet and Neumann BCs are given in Fig. C.4.

C.3 "Not-so-simple" shear deformation

Current configuration of the problem is

$$x_1 = X_1 + kX_2^2, \quad x_2 = X_2, \quad x_3 = X_3 \tag{C.19}$$

and this can be expressed in the form of deformation gradient

$$\mathbf{F} = \begin{bmatrix} 1 & 2kX_2 & 0 \\ 0 & 1 & 0 \\ 0 & 0 & 1 \end{bmatrix} \tag{C.20}$$

where $k > 0$. The strain invariants are

$$I_1 = K^2 + 3 = I_2, \quad I_3 = 1 \tag{C.21}$$

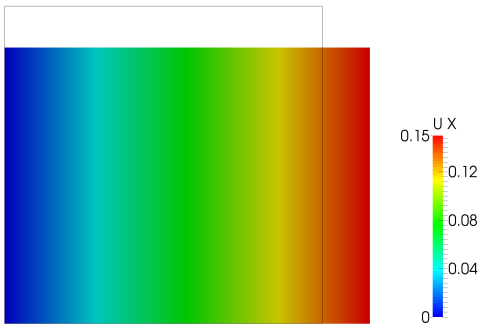

(a) FEM (u_x)

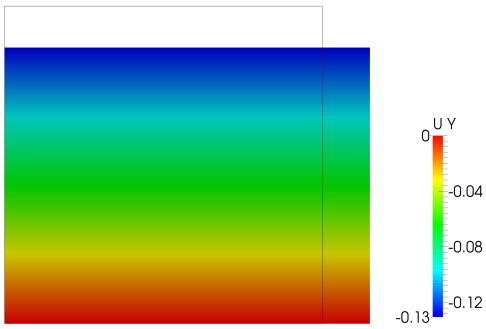

(b) FEM (u_y)

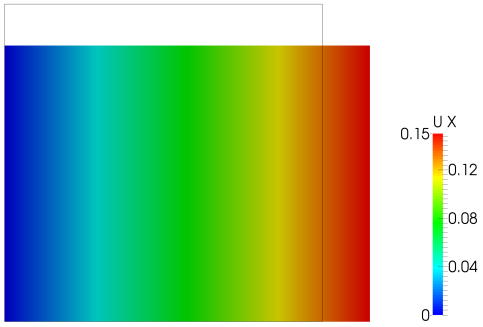

(c) Smoothed FEM (u_x)

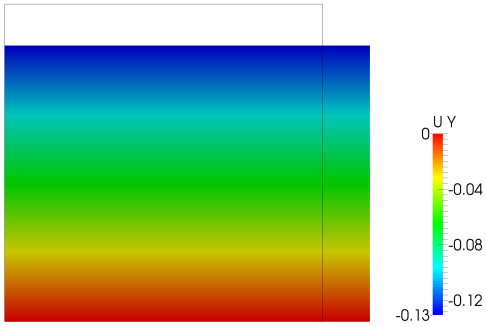

(d) Smoothed FEM (u_y)

Figure C.4: Deformed shapes for the uniform extension with lateral contraction with mixed Dirichlet and Neumann BCs (FEM and S-FEM with T3 32×32 elements)

where $K = 2kX_2$.

Dirichlet boundary conditions. Non-homogeneous Dirichlet BCs on all edges are imposed:

- All edges: $(u_1, u_2) = (kX_2^2, 0)$

Note that this function is quadratic in X_2.

The analytical strain energy for the "Not-so-simple" shear problem can be obtained

as

$$\mathcal{W} = \frac{\mu}{2} K^2 = \frac{\mu}{2} (2kX_2)^2 = 2\mu k^2 X_2^2 = 1.6 \tag{C.22}$$

where $K = 2kX_2$ is given in Appendix D.3.

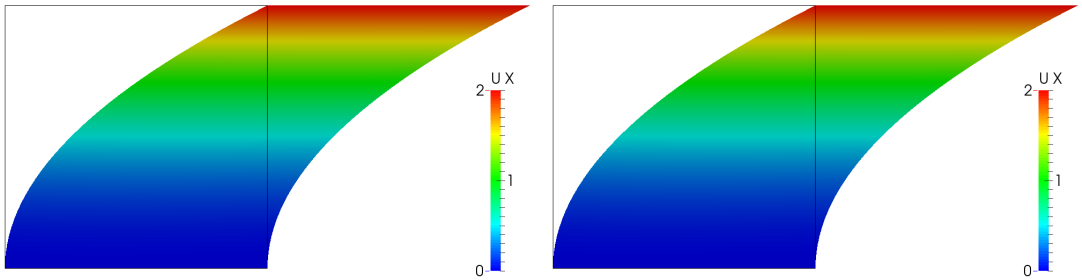

(a) FEM (u_x) (b) Smoothed FEM (u_x)

Figure C.5: Deformed shapes for the "Not-so-simple" shear deformation with Dirichlet BCs (FEM and S-FEM with T3 32×32 elements)

D Strain energy calculation

The stored energy function of compressible and incompressible neo-Hookean modes are respectively defined as

$$\mathcal{W}(\mathbf{C}) = \frac{1}{2}(\ln J)^2 - \mu_0 \ln J + \frac{1}{2}\mu_0 (\mathrm{tr}\mathbf{C} - 3) \tag{D.1}$$

and

$$\mathcal{W}(\mathbf{C}) = \frac{1}{2}\mu_0 (\mathrm{tr}\mathbf{C} - 3) \tag{D.2}$$

where Lamé's first parameter is $\lambda_0 = \kappa - (1/2)\,\mu_0$ in 2D and $\lambda_0 = \kappa - (2/3)\,\mu_0$ in 3D with Lamé's second parameter (or shear modulus) μ_0 and the bulk modulus κ. The right Cauchy-Green deformation tensor is $\mathbf{C} = \mathbf{F}^{\mathrm{T}}\mathbf{F}$ and the Jacobian $J = \det \mathbf{F}$.

The principal invariants of the right Cauchy-Green tensor and their derivatives

with respect to itself can be expressed as (or see Table 4.1)

$$\begin{aligned} I_1 &= \mathrm{tr}\,(\mathbf{C}) \\ I_2 &= \frac{1}{2}\left\{(\mathrm{tr}\mathbf{C})^2 - \mathrm{tr}\left(\mathbf{C}^2\right)\right\} \\ I_3 &= \det(\mathbf{C}) \end{aligned} \tag{D.3}$$

and

$$\begin{aligned} \frac{\partial I_1}{\partial \mathbf{C}} &= \mathbf{I} \\ \frac{\partial I_2}{\partial \mathbf{C}} &= I_1\mathbf{I} - \mathbf{C}^{\mathrm{T}} \\ \frac{\partial I_3}{\partial \mathbf{C}} &= I_3\mathbf{C}^{-\mathrm{T}} \end{aligned} \tag{D.4}$$

D.1 Simple shear deformation

For simple shear deformation, the deformation gradient $\mathbf{F}$ is given as

$$\mathbf{F} = \begin{bmatrix} 1 & k & 0 \\ 0 & 1 & 0 \\ 0 & 0 & 1 \end{bmatrix} \tag{D.5}$$

where $k = 1$ for simple shear deformation. Hence the right Cauchy-Green deformation tensor $\mathbf{C}$ can be obtained as

$$\begin{aligned} \mathbf{C} = \mathbf{F}^{\mathrm{T}}\mathbf{F} &= \begin{bmatrix} 1 & 0 & 0 \\ k & 1 & 0 \\ 0 & 0 & 1 \end{bmatrix} \begin{bmatrix} 1 & k & 0 \\ 0 & 1 & 0 \\ 0 & 0 & 1 \end{bmatrix} \\ &= \begin{bmatrix} 1 & k & 0 \\ k & k^2+1 & 0 \\ 0 & 0 & 1 \end{bmatrix} \end{aligned} \tag{D.6}$$

Therefore the strain invariant of the right Cauchy-Green tensor $\mathbf{C}$ is represented as

$$\begin{aligned} I_1(\mathbf{C}) &= \mathrm{tr}(\mathbf{C}) = k^2 + 3 \\ I_2(\mathbf{C}) &= \frac{1}{2}\left\{(\mathrm{tr}\mathbf{C})^2 - \mathrm{tr}\left(\mathbf{C}^2\right)\right\} = K^2 + 3 \\ I_3(\mathbf{C}) &= \det \mathbf{C} = 1 \end{aligned} \tag{D.7}$$

To get the strain energy for simple shear deformation, Eq. (D.7) is substituted to Eq. (D.2) and then the strain energy for simple shear deformation is

$$\mathcal{W} = \frac{1}{2}\mu_0 (I_1 - 3) = 0.3 \tag{D.8}$$

where the shear modulus is given as $\mu_0 = 0.6$.

D.2 Uniform extension with lateral contraction

The deformation gradient $\mathbf{F}$ of uniform extension with lateral contraction is

$$\mathbf{F} = \begin{bmatrix} \lambda_1 & 0 & 0 \\ 0 & \lambda_2 & 0 \\ 0 & 0 & \lambda_3 \end{bmatrix} \tag{D.9}$$

and consequently the left Cauchy-Green strain tensor can be calculated as

$$\begin{aligned} \mathbf{B} = \mathbf{F}\mathbf{F}^{\mathrm{T}} &= \begin{bmatrix} \lambda_1 & 0 & 0 \\ 0 & \lambda_2 & 0 \\ 0 & 0 & \lambda_3 \end{bmatrix} \begin{bmatrix} \lambda_1 & 0 & 0 \\ 0 & \lambda_2 & 0 \\ 0 & 0 & \lambda_3 \end{bmatrix} \\ &= \begin{bmatrix} \lambda_1^2 & 0 & 0 \\ 0 & \lambda_2^2 & 0 \\ 0 & 0 & \lambda_3^2 \end{bmatrix} \end{aligned} \tag{D.10}$$

The strain invariants of the left Cauchy-Green tensors are

$$\begin{aligned} I_1(\mathbf{B}) &= \mathrm{tr}(\mathbf{B}) = \lambda_1^2 + \lambda_2^2 + \lambda_3^2 = \lambda_1^2 + \frac{1}{\lambda_1^2} + 1 \\ I_2(\mathbf{B}) &= \frac{1}{2}\left\{(\mathrm{tr}\mathbf{B})^2 - \mathrm{tr}\left(\mathbf{B}^2\right)\right\} = \lambda_1^2\lambda_2^2 + \lambda_2^2\lambda_3^2 + \lambda_3^2\lambda_1^2 = \lambda_1^2 + \frac{1}{\lambda_1^2} + 1 \\ I_3(\mathbf{B}) &= \det(\mathbf{B}) = \lambda_1^2\lambda_2^2\lambda_3^2 = 1 \end{aligned} \tag{D.11}$$

where $\lambda_2 = 1/\lambda_1$ and $\lambda_3 = 1$ when the deformation is isochoric. Therefore the strain energy of this problem is

$$\mathcal{W} = \frac{1}{2}\mu(I_1 - 3) = \frac{1}{2}\mu\left(\lambda_1^2 + \frac{1}{\lambda_1^2} - 2\right) = 0.023593100189036 \tag{D.12}$$

where $\mu = 0.6$ and $\lambda_1 = 1.15$ are given.

D.3 "Not-so-simple" shear deformation

Current configuration of "Not-so-simple" shear deformation is given as

$$\begin{aligned} x_1 &= X_1 + kX_2^2 \\ x_2 &= X_2 \\ x_3 &= X_3 \end{aligned} \tag{D.13}$$

and thus the deformation gradient $\mathbf{F}$ for "Not-so-simple" shear deformation is

$$\mathbf{F} = \begin{bmatrix} 1 & 2kX_2 & 0 \\ 0 & 1 & 0 \\ 0 & 0 & 1 \end{bmatrix} \tag{D.14}$$

The right Cauchy-Green tensor can be expressed as

$$\begin{aligned}\mathbf{C} = \mathbf{F}^{\mathrm{T}}\mathbf{F} &= \begin{bmatrix} 1 & 0 & 0 \\ 2kX_2 & 1 & 0 \\ 0 & 0 & 1 \end{bmatrix} \begin{bmatrix} 1 & 2kX_2 & 0 \\ 0 & 1 & 0 \\ 0 & 0 & 1 \end{bmatrix} \\ &= \begin{bmatrix} 1 & 2kX_2 & 0 \\ 2kX_2 & 4k^2X_2^2+1 & 0 \\ 0 & 0 & 1 \end{bmatrix}\end{aligned} \tag{D.15}$$

Now the strain invariants of the right Cauchy-Green tensor can be computed

$$\begin{aligned} I_1(\mathbf{C}) &= \mathrm{tr}(\mathbf{C}) = 4k^2X_2^2 + 3 \\ I_2(\mathbf{C}) &= \frac{1}{2}\left\{(\mathrm{tr}\mathbf{C})^2 - \mathrm{tr}\left(\mathbf{C}^2\right)\right\} = 4k^2X_2^2 + 3 \\ I_3(\mathbf{C}) &= \det(\mathbf{C}) = 1 \end{aligned} \tag{D.16}$$

Eq. (D.1) can be re-written as

$$\mathcal{W} = \frac{\mu}{2}(I_1 - 3) = 2\mu k^2 X_2^2 \tag{D.17}$$

and finally the strain energies of "Not-so-simple" shear deformation in 2D and 3D are obtained respectively

$$\begin{aligned} W &= \int_0^2 \int_0^2 \mathcal{W}\mathrm{d}X_1\mathrm{d}X_2 \\ &= 2\int_0^2 2\mu k^2 X_2^2 \mathrm{d}X_2 \\ &= 4\mu k^2 \left(\frac{1}{3}X_2^3\Big|_0^2\right) = 1.6 \end{aligned} \tag{D.18}$$

and

$$\begin{aligned} W &= \int_0^2 \int_0^2 \int_0^2 \mathcal{W} \mathrm{d}X_1 \mathrm{d}X_2 \mathrm{d}X_3 \\ &= 4 \int_0^2 2\mu k^2 X_2^2 \mathrm{d}X_2 \\ &= 8\mu k^2 \left(\frac{1}{3} X_2^3 \Big|_0^2 \right) = 3.2 \end{aligned} \tag{D.19}$$

where shear modulus $\mu = 0.6$ and the deformation $k = 0.5$.

D.4 Bending of a rectangular block

The deformation in cylinder coordinate for bending a rectangular block given in Chapter 4.3.1 (or see in reference [123]) is recalled here:

$$f(X) = \sqrt{2\alpha X}, \quad g(Y) = \frac{1}{\alpha} Y \tag{D.20}$$

where α is a bending factor. The deformation gradient can be represented as

$$\mathbf{F} = \begin{bmatrix} f'(X) & 0 & 0 \\ 0 & f(X)\, g'(Y) & 0 \\ 0 & 0 & 1 \end{bmatrix} \tag{D.21}$$

where the principle stretches are defined as

$$\begin{aligned} \lambda_1^2 &= \left(f'(X)\right)^2 \\ \lambda_2^2 &= \left(f(X)\, g'(Y)\right)^2 \\ \lambda_3^2 &= 1 \end{aligned} \tag{D.22}$$

where

$$f'(X) = \frac{\sqrt{2\alpha}}{2\sqrt{X}} = \sqrt{\frac{\alpha}{2X}}, \quad g'(Y) = \frac{1}{\alpha} \tag{D.23}$$

A compressible neo-Hookean model is given by [15]:

$$\mathcal{W} = \frac{\mu}{2}\left(\mathrm{tr}\mathbf{C} - 3\right) + \frac{\lambda}{2}\left(\ln J\right)^2 - \mu \ln J \tag{D.24}$$

where μ is the shear modulus and the Lamé's first parameter is $\lambda = \kappa - (2/3)\,\mu$ with the bulk modulus κ. The principal invariants are

$$\begin{aligned} I_1 &= \mathrm{tr}\mathbf{C} = \lambda_1 + \lambda_2 + \lambda_3 \\ I_2 &= \frac{1}{2}\left\{\left(\mathrm{tr}\mathbf{C}\right)^2 - \mathrm{tr}\left(\mathbf{C}^2\right)\right\} = \lambda_1\lambda_2 + \lambda_2\lambda_3 + \lambda_3\lambda_1 \\ I_3 &= \det\left(\mathbf{C}\right) = \lambda_1\lambda_2\lambda_3 \end{aligned} \tag{D.25}$$

Substituting Eq. (D.22) into Eq. (D.25), the invariants can be obtained as follows

$$\begin{aligned} I_1 &= \left(f'\left(X\right)\right)^2 + \left(f\left(X\right)g'\left(Y\right)\right)^2 + 1 \\ &= \frac{\alpha}{2X} + \frac{2\alpha X}{\alpha^2} + 1 = \frac{\alpha}{2X} + \frac{2X}{\alpha} + 1 \\ I_3 &= \left(f'\left(X\right)\right)^2\left(f\left(X\right)g'\left(Y\right)\right)^2 = \frac{\alpha}{2X}2\alpha X\frac{1}{\alpha^2} = 1 \end{aligned} \tag{D.26}$$

Hence Eq. (D.24) can be re-written as

$$\begin{aligned} \mathcal{W} &= \frac{\mu}{2}\left(\frac{\alpha}{2X} + \frac{2X}{\alpha} - 2\right) \\ &= \mu\frac{\left(\alpha - 2X\right)^2}{4\alpha X} = \mu\frac{\left(0.9 - 2X\right)^2}{3.6X} \end{aligned} \tag{D.27}$$

where the Jacobian is $J = \sqrt{I_3} = 1$ and the bending factor is $\alpha = 0.9$.

Let the geometry of the rectangular block for 2D be

$$2 \le X \le 3, \quad -2 \le Y \le 2$$

thus, the strain energy in the whole domain is

$$\begin{aligned} W &= \int_2^3 \int_{-2}^2 \mathcal{W} \mathrm{d}A \\ &= 4 \int_2^3 \mathcal{W}(X)\, \mathrm{d}X \\ &= 4\mu \int_2^3 \frac{0.81 - 3.6X + 4X^2}{3.6X} \mathrm{d}X \\ &= 4\mu \int_2^3 \left(\frac{9}{40X} - 1 + \frac{10}{9}X \right) \mathrm{d}X \\ &= 4\mu \left(\frac{9}{40} \ln X \Big|_2^3 - X|_2^3 + \frac{10}{18} X^2 \Big|_2^3 \right) \end{aligned} \tag{D.28}$$

where the shear modulus $\mu = 0.6$ is used in this thesis, therefore strain energy is $W \approx 4.485618$.

E Computer Code

In this chapter, one of computer scripts for DOLFIN finite element software used in this thesis is presented. Scripts are written in Python and a given example script is for bending of a rectangular block studied in section 4.3.6 of Chapter 4.

```
#!/usr/bin/python
# -*- coding: utf-8 -*-

""" Bending Blcok problem for mesh distortion with Dirichlet boundary
  conditions
for incompressible hyperelasticity.

Based on:

http://fenicsproject.org/documentation/dolfin/dev/python/demo/pde/
  hyperelasticity/python/documentation.html

, the paper:

http://dx.doi.org/10.1016/j.cma.2008.06.004

and author: Jack S. Hale 2014 mail@jackhale.co.uk

Chang-Kye Lee 2015 changkyelee@gmail.com
"""

import dolfin as df

from dolfin import Identity, grad, ln, det, tr, dot
```

```
23          from decimal import Decimal
24          # from __future__ import division
25
26          def mini(mesh, order=1):
27          assert(order >= 1)
28          U = df.VectorFunctionSpace(mesh, "CG", order) + \
29          df.VectorFunctionSpace(mesh, "Bubble", 3)
30          P = df.FunctionSpace(mesh, "CG", order)
31          V = df.MixedFunctionSpace([U, P])
32
33          return V
34
35
36          def stokes(mesh, order=2):
37          assert(order >= 2)
38          U = df.VectorFunctionSpace(mesh, "CG", order)
39          P = df.FunctionSpace(mesh, "DG", order - 2)
40          V = df.MixedFunctionSpace([U, P])
41
42          return V
43
44
45          def BendingBlock(nx,ny):
46          ##    mesh = df.Mesh("meshes/Bending_Block_"+repr(nx)+"x"+repr(ny)+".xml
              ")
47          mesh = df.RectangleMesh(df.Point(2,-2),df.Point(3,2),nx,ny)
48          dims = mesh.type().dim()
49
50          mu_python = 0.6
51          mu = df.Constant(mu_python)
52          kappa = 1.95
53          lmbda = df.Constant(kappa - (1.0/2.0)*mu_python)
54
55          order = 2
56          V = stokes(mesh, order=order))
57          #V = mini(mesh, order=order)
58
59          # Define boundary conditions
60          def left(x, on_boundary):
61          return df.near(x[0], 2.0) and on_boundary
62
63          def right(x, on_boundary):
64          return df.near(x[0], 3.0) and on_boundary
65
```

```
66          def bottom(x, on_boundary):
67          return df.near(x[1], -2.0) and on_boundary
68
69          def top(x, on_boundary):
70          return df.near(x[1], 2.0) and on_boundary
71
72          moved = df.Expression(("sqrt(2*0.9*x[0])*cos(x[1]/0.9)-x[0]",\
73          "sqrt(2*0.9*x[0])*sin(x[1]/0.9)-x[1]"))
74          bcs_moved = [df.DirichletBC(V.sub(0), moved, face)
75          for face in [left, right, top, bottom]]
76          bcs = bcs_moved
77
78          dx = df.dx
79
80          # solution
81          up = df.Function(V)
82          # test functions
83          vq = df.TestFunction(V)
84
85          # START LAOD INCREMENT
86          nstep = 50
87
88          for istep in range(1,nstep+1):
89
90              scale = float(istep)/nstep
91
92              print "Load step Number: %f" %(scale)
93
94              LoadFactor = scale
95
96              moved = df.Expression(("LoadFactor*(sqrt(2*0.9*x[0])*cos(x[1]/0.9)-x
                    [0])",\
97              "LoadFactor*(sqrt(2*0.9*x[0])*sin(x[1]/0.9)-x[1])"),LoadFactor=
                    LoadFactor)
98
99              # print "DBC: %f" %(moved)
100
101             bcs_moved = [df.DirichletBC(V.sub(0), moved, face)
102             for face in [left, right, top, bottom]]
103             bcs = bcs_moved
104
105             # incremental solution
106             dup = df.TrialFunction(V)
107
```

```
108
109             du, dp = df.split(dup)
110             u, p = df.split(up)
111             v, q = df.split(vq)
112
113             # standard definitions,
114             # see e.g. http://dx.doi.org/10.1016/j.cma.2008.06.004
115             I = Identity(dims)
116             F = I + grad(u)
117             C = F.T*F
118             J = det(F)
119             Ic = tr(C)
120
121             # from Aurrichio et al. http://dx.doi.org/10.1016/j.cma.2008.06.004
122             psi = (mu/2.0)*(Ic - dims) - mu*ln(J) + p*ln(J) - (1.0/(2.0*lmbda))*
                  p**2
123
124             # energy function
125             Pi = psi*dx
126             # gateux derivative with respect to test functions
127             F = df.derivative(Pi, up, vq)
128             # gateux derivative with resepct to increment (linearisation)
129             J = df.derivative(F, up, dup)
130
131             # Add bcs as third parameter to this call
132             problem = df.NonlinearVariationalProblem(F, up, bcs, J)
133             solver = df.NonlinearVariationalSolver(problem)
134
135
136             # up = up + dup
137
138
139             solver.solve()
140
141
142         u_h, p_h = up.split()
143
144         #f = df.File("displacement.pvd")
145         f = df.File("./Results/BendingBlock/BendingBlock_"+repr(nx)+"x"+repr(ny)
              +".pvd")
146         f << u_h
147
148         results = {}
149         # results['Distortion_Factor'] = air
```

```
150         results['Xelem'] = nx
151         results['Yelem'] = ny
152         results['internal_work'] = df.assemble(psi*dx)
153         results['dofs'] = V.dim()
154 
155         #df.plot(u_h)
156 
157         return results
158 
159 
160         if __name__ == "__main__":
161         #    xelem = [2, 4]
162         #    yelem = [4, 8, 16, 32]
163         #    for nx in xelem:
164         #        for ny in yelem:
165         results = BendingBlock(nx=4,ny=32)
166         print results
```

References

[1] F.M. Andrade Pires, E.A. de Souza Neto, and J.L. de la Cuesta Padilla. An assessment of the average nodal volume formulation for the analysis of nearly incompressible solids under finite strains. *Communications in Numerical Methods in Engineering*, 20(7):569–583, 2004.

[2] D. Arnold, F. Brezzi, and M. Fortin. A stable finite element for the stokes equations. *Calcolo*, 21(4):337–344, 1984.

[3] H. Askes, E. Kuhl, and P. Steinmann. An ALE formulation based on spatial and material settings of continuum mechanics. Part 2: Classification and applications. *Computer Methods in Applied Mechanics and Engineering*, 193(39-41):4223–4245, 1993.

[4] F. Auricchio, L. Beirão da Veiga, C. Lovadina, and A. Reali. A stability study of some mixed finite elements for large deformation elasticity problems. *Computer Methods in Applied Mechanics and Engineering*, 194(9-11):1075–1092, 2005.

[5] F. Auricchio, L. Beirão da Veiga, C. Lovadina, and A. Reali. An analysis of some mixed-enhanced finite element for plane linear elasticity. *Computer Methods in Applied Mechanics and Engineering*, 194(27-29):2947–2968, 2005.

[6] F. Auricchio, L. Beirão da Veiga, C. Lovadina, and A. Reali. The importance of the exact satisfaction of the incompressibility constraint in nonlinear elas-

ticity: mixed FEMs versus NURBS-based approximations. *Computational Geometry and Analysis*, 199(5-8):314–323, 2010.

[7] J.L.F. Aymone, E. Bittencourt, and G.J. Creus. Simulation of 3D metal-forming using an arbitrary Lagrangian-Eulerian finite element method. *Journal of Materials Processing Technology*, 110:218–232, 2001.

[8] P.M. Baiz, S. Natarajan, S.P.A. Bordas, P. Kerfriden, and T. Rabczuk. Linear buckling analysis of cracked plates by SFEM and XFEM. *Journal of Mechanics of Materials and Structures*, 6(9-10):1213–1238, 2011.

[9] K.-J. Bathe. *Finite Element Procedures in Engineering Analysis*. Prentice-Hall, 1996.

[10] K.-J. Bathe, E. Ramm, and E.L. Wilson. Finite element formulations for large deformation dynamic analysis. *International Journal for Numerical Methods in Engineering*, 9(2):353–386, 1975.

[11] L. Beirão da Veiga, F. Brezzi, A. Cangiani, G. Manzini, L.D. Marini, and A. Russo. Basic Principles of Virtual Element Methods. *Mathematical Models and Methods in Applied Sciences*, 23(1):199–214, 2013.

[12] S. Beissel and T. Belytschko. Nodal integration of the element-free Galerkin method. *Computer Methods in Applied Mechanics and Engineering*, 139(1-4):49–74, 1996.

[13] T. Belytschko, Y. Guo, W.K. Liu, and S.P. Xiao. A unified stability analysis of meshless particle methods. *International Journal for Numerical Methods in Engineering*, 48(9):1359–1400, 2000.

[14] T. Belytschko, Y. Krongauz, D. Organ, M. Fleming, and P. Krysl. Meshless methods: An overview and recent developments. *Computer Methods in Applied Mechanics and Engineering*, 139(1-4):3–47, 1996.

[15] T. Belytschko, B. Moran, and W.K. Liu. *Nonlinear Finite Element for Continua and Structures*. Wiley, 1999.

[16] P.J. Blatz and W.L. Ko. Application of finite elastic theory to the deformation of rubbery materials. *Transactions of the Society of Rheology*, 6:223–252, 1962.

[17] D.G. Bolzon and R. Vitaliani. The Blatz-Ko material model and homogenization. *Archive of Applied Mechanics*, 63(4-5):228–241, 1993.

[18] J. Bonet and A.J. Burton. A simple average nodal pressure tetrahedral element for incompressible and nearly incompressible dynamic explicit applications. *Communications in Numerical Methods in Engineering*, 14(5):437–449, 1998.

[19] J. Bonet, H. Marriott, and O. Hassan. An averaged nodal deformation gradient linear tetrahedral element for large strain explicit dynamic applications. *Communications in Numerical Methods in Engineering*, 17(8):551–561, 2001.

[20] J. Bonet, H. Marriott, and O. Hassan. Stability and comparison of different linear tetrahedral formulations for nearly incompressible explicit dynamic applications. *International Journal for Numerical Methods in Engineering*, 50:119–133, 2001.

[21] J. Bonet and R. Wood. *Nonlinear Continuum Mechanics for Finite Element Analysis*. Cambridge University Press, second edition, 1997.

[22] J. Bonet and R.D. Wood. *Nonlinear Continuum Mechanics for Finite Element Analysis*. Cambridge University Press, second edition, 2008.

[23] S.P.A. Bordas and S. Natarajan. On the approximation in the smoothed finite element method (SFEM). *International Journal for Numerical Methods in Engineering*, 81(5):660–670, 2010.

[24] S.P.A. Bordas, S. Natarajan, P. Kerfriden, C.E. Augarde, D.R. Mahapatra, T. Rabczuk, and S. Dal Pont. On the performance of strain smoothing for quadratic and enriched finite element approximations (XFEM/GFEM/PUFEM). *International Journal for Numerical Methods in Engineering*, 86(4-5):637–666, 2011.

[25] S.P.A. Bordas, T. Rabczuk, H. Nguyen-Xuan, V.P. Nguyen, S. Natarajan, T. Bog, D.M. Quan, and N.V. Hiep. Strain smoothing in FEM and XFEM. *Computers and Structures*, 88(23-24):1419–1443, 2010.

[26] M. Botsch, M. Pauly, L. Kobbelt, P. Alliez, B. Lévy, S. Bischoff, and C. Röossl. Geometric Modeling Based on Polygonal Meshes. *SIGGRAPH 2007 course*, inria-00186820, 2007.

[27] H. Braess and P. Wriggers. Arbitrary Lagrangian Eulerian finite element analysis of free surface flow. *Computer Methods in Applied Mechanics and Engineering*, 190:95–109, 2000.

[28] F. Brezzi and M. Fortin, editors. *Mixed and Hybrid Finite Element Methods*. Springer-Verlag, New York, 1991.

[29] C. Carstensen and R. Klose. Elastoviscoplastic Finite Element analysis in 100 lines of Matlab. *Journal of Numerical Mathematics*, 10(3):157–192, 2002.

[30] I. Caylak and R. Mahnken. Stabilized mixed triangular elements with area bubble functions at small and large deformations. *Computers and Structures*, 138:172–182, 2014.

[31] M. Cervera, M. Chiumenti, and R. Codina. Mixed stabilized finite element methods in nonlinear solid mechanics. *Computer Methods in Applied Mechanics and Engineering*, 199(37-40):2559–2570, 2010.

[32] M. Cervera, M. Chiumenti, Q. Valverde, and C. Agelet de Saracibar. Mixed linear/linear simplicial elements for incompressible elasticity and plasticity. *Computer Methods in Applied Mechanics and Engineering*, 192(49-50):5249–5263, 2003.

[33] J.-S. Chen, C.-T. Wu, S. Yoon, and Y. You. A stabilized conforming nodal integration for Galerkin mesh-free methods. *International Journal for Numerical Methods in Engineering*, 50(2):435–466, 2001.

[34] J.-S. Chen, S. Yoon, H.-P. Wang, and W.K. Liu. An improved reproducing kernel particle method for nearly incompressible finite elasticity. *Computational Methods in Applied Mechanical Engineering*, 181:117–145, 2000.

[35] J.-S. Chen, S. Yoon, and C.-T. Wu. Non-linear version of stabilized conforming nodal integration for Galerkin mesh-free methods. *International Journal for Numerical Methods in Engineering*, 53(12):2587–2615, 2002.

[36] M. Chiumenti, Q. Valverde, C. Agelet de Saracibar, and M. Cervera. A stabilized formulation for incompressible elasticity using linear displacement and pressure interpolations. *Computer Methods in Applied Mechanics and Engineering*, 191(46):5253–5264, 2002.

[37] A.J. Chorin. A numerical method for solving incompressible viscous flow problems. *Journal of Computational Physics*, 2:12–26, 1967.

[38] S. Cotin, H. Delingette, and N. Ayache. A hybrid elastic model for real-time cutting, deformations, and force feedback for surgery training and simulation. *The Visual Computer*, 16(8):437–452, 2000.

[39] H. Courtecuisse, J. Allard, P. Kerfriden, S.P.A. Bordas, S. Cotin, and C. Duriez. Real-time simulation of contact and cutting of heterogeneous soft-tissues. *Medical Image Analysis*, 18(2):394–410, 2014.

[40] M.A. Crisfield. *Non-Linear Finite Element Analysis of Solids and Structures*. Wiley, 1996.

[41] X.Y. Cui, G.R. Liu, G.Y. Li, G.Y. Zhang, and G.Y. Sun. Analysis of elastic-plastic problems using edge-based smoothed finite element method. *International Journal of Pressure Vessels and Piping*, 86(10):711–718, 2009.

[42] X.Y. Cui, G.R. Liu, G.Y. Li, X. Zhao, T.T. Nguyen, and G.Y. Sun. A Smoothed Finite Element Method (SFEM) for Linear and Geometrically Nonlinear Analysis of Plates and Shells. *Computer Modelling in Engineering and Science*, 28(2):109–125, 2008.

[43] K.Y. Dai and G.R. Liu. Free and forced vibration analysis using the smoothed finite element method (SFEM). *Journal of Sound and Vibration*, 301(3-5):803–820, 2007.

[44] K.Y. Dai, G.R. Liu, and T.T. Nguyen. An n-sided polygonal smoothed finite element method (nSFEM) for solid mechanics. *Finite Elements in Analysis and Design*, 43(11-12):847–860, 2007.

[45] E.A. de Souza Neto, F.M. Andrade Pires, and D.R.J Owen. F-bar-based linear triangles and tetrahedra for finite strain analysis of nearly incompressible solids. Part I: formulation and benchmarking. *International Journal for Numerical Methods in Engineering*, 62(3):353–383, 2005.

[46] H.. Delingette, S. Cotin, and N. Ayache. A Hybrid Elastic Model allowing Real-Time Cutting, Deformations and Force-Feedback for Surgery Training and Simulation. In *Computer Animation*, pages 70–81, 1999.

[47] M. Destrade and G. Saccomandi. On the rectilinear shear of compressible and incompressible elastic slabs. *International Journal of Engineering Science*, 48:1202–1211, 2010.

[48] R. Dimitri. Isogeometric treatment of large deformation contact and debonding problems with T-splines: a review. *Curved and Layered Structures*, 2(1):59–90, 2015.

[49] C.R. Dohrmann, M.W. Heinstein, J. Jung, S.W. Key, and W.R. Witkowski. Node-based uniform strain elements for three-node triangular and four-node tetrahedral meshes. *International Journal for Numerical Methods in Engineering*, 47(9):1549–1568, 2000.

[50] J. Donea, A. Huerta, J.-Ph. Ponthot, and A. Rodríguez-Ferran. Arbitrary Lagrangian-Eulerian Methods, 2004.

[51] J. Douglas Jr. and J. Wang. An Absolutely Stabilized Finite Element Method for the Stokes Problem. *Mathematics of Computation*, 52(186):495–508, 1989.

[52] Q. Duan, X. Li, H. Zhang, and T. Belytschko. Second-order accurate derivatives and integration schemes for meshfree methods. *International Journal for Numerical Methods in Engineering*, 92:399–424, 2012.

[53] F. Duarte, R. Gormaz, and S. Natesan. Arbitrary Lagrangian-Eulerian method for Navier-Stokes equations with moving boundaries. *Computer Methods in Applied Mechanics and Engineering*, 193(45-47):4819–4836, 2004.

[54] S.Z. Feng, X.Y. Cui, and G.Y. Li. Transient thermal mechanical analyses using a face-based smoothed finite element method (FS-FEM). *International Journal of Thermal Sciences*, 74:95–103, 2013.

[55] L.P. Franca, T.J.R. Hughes, A.F.D. Loula, and I. Miranda. A New Family of Stable Elements for Nearly Incompressible Elasticity Based on a Mixed Petrov-Galerkin Finite Element Formulation. *Numerische Mathematik*, 53:123–141, 1988.

[56] T.-P. Fries and H.G. Matthies. A stabilized and coupled meshfree/meshbased method for the incompressible Navier-Stokes equations-Part I: Stabilization. *Computer Methods in Applied Mechanics and Engineering*, 195(44-47):6205–6224, 2006.

[57] M.S. Gadala. Recent trends in ALE formulation and its applications in solid mechanics. *Computer Methods in Applied Mechanics and Engineering*, 193(39-41):4247–4275, 2004.

[58] M.S. Gadala and J. Wang. ALE formulation and its application in solid mechanics. *Computer Methods in Applied Mechanics and Engineering*, 167(1-2):33–55, 1998.

[59] E.W. Gekeler. *Mathematical Methods for Mechanics: A Handbook with MATLAB Experiments*. Springer, 2008.

[60] A.E. Green and J.E. Adkins. *Large Elastic Deformations (and Non-linear Continuum Mechanics)*. Oxford University Press, 1970.

[61] Z.C. He, G.R. Liu, Z.H. Zhong, G.Y. Zhang, and A.G. Cheng. Coupled analysis of 3D structural-acoustic problems using the edge-based smoothed finite element method/finite element method. *Finite Elements in Analysis and Design*, 46(12):1114–1121, 2010.

[62] H.D. Hibbitt, P.V. Marcal, and J.R. Rice. A finite element formulation for problems of large strain and large displacement. *International Journal of Solids and Structures*, 6(8):1069–1086, 1970.

[63] C.O. Horgan. Remarks on Ellipticity for the Generalized Blatz-Ko Constitutive Model for a Compressible Nonlinearly Elastic Solid. *Journal of Elasticity*, 42:165–176, 1996.

[64] W. Hu, C.T. Wu, and M. Koishi. A displacement-based nonlinear finite element formulation using meshfree-enriched triangular elements for the

two-dimensional large deformation analysis of elastomers. *Finite Elements in Analysis and Design*, 50:161–172, 2012.

[65] A. Huerta, Y. Vidal, and P. Villon. Pseudo-divergence-free element free Galerkin method for incompressible fluid flow. *Computer Methods in Applied Mechanics and Engineering*, 193(12-14):1119–1136, 2004.

[66] T.J.R. Hughes. Multiscale phenomena: Green's functions, the Dirichlet-to-Neumann formulation, subgrid scale models, bubbles and the origins of stabilized methods. *Computer Methods in Applied Mechanics and Engineering*, 127(1-4):387–401, 1995.

[67] C. Jiang, G.R. Liu, X. Han, Z.-Q. Zhang, and W. Zeng. A smoothed finite element method for analysis of anisotropic large deformation of passive rabbit ventricles in diastole. *International Journal for Numerical Methods in Biomedical Engineering*, 33(1), 2015.

[68] C. Jiang, Z.-Q. Zhang, X. Han, and G.-R. Liu. Selective smoothed finite element methods for extremely large deformation of anisotropic incompressible bio-tissues. *International Journal for Numerical Methods in Engineering*, 2014.

[69] E.P. Kasper and R.L. Taylor. A mixed-enhanced strain method. *Computers and Structures*, 75(3):237–250, 2000.

[70] A.R. Khoei, M. Anahid, and K. Shahim. An extended arbitrary Lagrangian-Eulerian finite element method for large deformation of solid mechanics. *Finite Elements in Analysis and Design*, 44(6-7):401–416, 2008.

[71] O. Klass, A. Maniatty, and M.S. Shephard. A stabilized mixed finite element method for finite elasticity. Formulation for linear displacement and pressure interpolation. *Computer Methods in Applied Mechanics and Engineering*, 180(1-2):65–79, 1999.

[72] E. Kuhl, H. Askes, and P. Steinmann. An ALE formulation based on spatial and material settings of continuum mechanics. Part 1: Generic hyperelastic formulation. *Computer Methods in Applied Mechanics and Engineering*, 193(39-41):4207–4222, 2004.

[73] B.P. Lamichhane. Inf-sup stable finite-element pairs based on dual meshes and bases for nearly incompressible elasticity. *IMA Journal of Numerical Analysis*, 29(2):404–420, 2009.

[74] B.P. Lamichhane. A mixed finite element method for nearly incompressible elasticity and Stokes equations using primal and dual meshes with quadrilateral and hexahedral grids. *Journal of Computational and Applied Mathematics*, 260:356–363, 2014.

[75] C.V. Le, H. Askes, and M. Gilbert. Adaptive element-free Galerkin method applied to the limit analysis of plates. *Computer Methods in Applied Mechanics and Engineering*, 199(37-40):2487–2496, 2010.

[76] C.V. Le, H. Askes, and M. Gilbert. A locking-free stabilized kinematic EFG model for plan strain limit analysis. *Computers and Structures*, 106-107:1–8, 2012.

[77] C.V. Le, M. Gilbert, and H. Askes. Limit analysis of plates using the EFG method and second-order cone programming. *International Journal for Numerical Methods in Engineering*, 78(13):1532–1552, 2009.

[78] C.V. Le, H. Nguyen-Xuan, H. Askes, S.P.A. Bordas, T. Rabczuk, and H. Nguyen-Vinh. A cell-based smoothed finite element method for kinematic limit analysis. *International Journal for Numerical Methods in Engineering*, 83(12):1651–1674, 2010.

[79] P. Le Tallec. Numerical Methods For Three-dimensional Elasticity. In P.G. Ciarlet and J.L. Lions, editors, *in Handbook of Numerical Analysis*, volume III, pages 465–624. North-Holland, 1994.

[80] W. Li, Y. Chai, M. Lei, and G.R. Liu. Analysis of coupled structural-acoustic problems based on the smoothed finite element method (S-FEM). *Engineering Analysis with Boundary Elements*, 42:84–91, 2014.

[81] G.R. Liu. *Meshfree Methods: Moving Beyond and the Finite Element Method*. CRC Press, 2003.

[82] G.R. Liu, K.Y. Dai, and T.T. Nguyen. A smoothed finite element method for mechanics problems. *Computational Mechanics*, 39(6):859–877, 2007.

[83] G.R. Liu and Y.T. Gu. *An Introduction to Meshfree Methods and Their Programming*. Springer, 2005.

[84] G.R. Liu and T.T. Nguyen. *Smoothed Finite Element Methods*. CRC Press, 2010.

[85] G.R. Liu, T.T. Nguyen, K.Y. Dai, and K.Y. Lam. Theoretical aspects of the smoothed finite element method (SFEM). *International Journal for Numerical Methods in Engineering*, 71(8):902–930, 2007.

[86] G.R. Liu, T. Nguyen-Thoi, and K.Y. Lam. An edge-based smoothed finite element method (ES-FEM) for static, free and forced vibration analyses of solids. *Journal of Sound and Vibration*, 320(4-5):1100–1130, 2009.

[87] G.R. Liu, T. Nguyen-Thoi, H. Nguyen-Xuan, and K.Y. Lam. A node-based smoothed finite element method (NS-FEM) for upper bound solutions to solid mechanics problems. *Computers and Structures*, 87(1-2):14–26, 2009.

[88] G.R. Liu, H. Nguyen-Xuan, and T. Nguyen-Thoi. A theoretical study on the smoothed FEM (S-FEM) models: Properties, accuracy and conver-

gence rates. *International Journal for Numerical Methods in Engineering*, 84(10):1222–1256, 2010.

[89] G.R. Liu and G.Y. Zhang. Upper bound solution to elasticity problem: A unique property of the linear conforming point interpolation method (LC-PIM. *International Journal for Numerical Methods in Engineering*, 74(7):1128–1161, 2008.

[90] A. Logg, K.-A. Mardal, and G.N. Wells. *Automated Solution of Differential Equations by the Finite Element Method*. Springer, 2012.

[91] A. Logg and G.N. Wells. Automated Finite Element Computing. *ACM Transactions on Mathematical Software*, 37(2), 2010.

[92] C. Lovadina and F. Auricchio. On the enhanced strain technique for elasticity problems. *Computers and Structures*, 81(8-11):777–787, 2003.

[93] R. Mahnken and I. Caylak. Stabilization of bi-linear mixed finite elements for tetrahedra with enhanced interpolation using volume and area bubble functions. *International Journal for Numerical Methods in Engineering*, 75(4):377–413, 2008.

[94] R. Mahnken, I. Caylak, and G. Laschet. Two mixed finite element formulations with area bubble functions for tetrahedral elements. *Computer Methods in Applied Mechanics and Engineering*, 197(9-12):1147–1165, 2008.

[95] L.E. Malvern. *Introduction to the Mechanics of a Continua Medium*. Prentice-Hall, 1969.

[96] R.M. McMeeking and J.R. Rice. Finite-element formulations for problems of large elastic-plastic deformation. *International Journal of Solids and Structures*, 11(5):601–616, 1975.

[97] L.A. Mihai and A. Goriely. Numerical simulation of shear and the Poynting effects by the finite element method: An application of the generalised empirical inequalities in non-linear elasticity. *International Journal of Non-Linear Mechanics*, 49:1202–1211, 2013.

[98] M. Mooney. A Theory of Large Elastic Deformation. *Journal of Applied Physics*, 11(9):582–592, 1940.

[99] S. Natarajan, S. Bordas, and D.R. Mahapatra. Numerical integration over arbitrary polygonal domains based on Schwarz-Christoffel conformal mapping. *International Journal for Numerical Methods in Engineering*, 80(1):103–134, 2009.

[100] S. Natarajan, S.P.A. Bordas, and E.T. Ooi. On the equivalence between the cell-based smoothed finite element method and the virtual element method. *International Journal for Numerical Methods in Engineering*, pages 1–34, 2013.

[101] T.T. Nguyen, G.R. Liu, K.Y. Dai, and K.Y. Lam. Selective Smoothed Finite Element Method. *Tsinghua Science & Technology*, 12(5):497–508, 2007.

[102] V.P. Nguyen, C. Anitescu, S.P.A. Bordas, and T. Rabczuk. Isogeometric analysis: An overview and computer implementation aspects. *Mathematics and Computers in Simulation*, 117:89–116, 2015.

[103] V.P. Nguyen, T. Rabczuk, S. Bordas, and M. Duflot. Meshless method: A review and computer implementation aspects. *Mathematics and computers in Simulation*, 79(3):763–813, 2008.

[104] N. Nguyen-Thanh, T. Rabczuk, H. Nguyen-Xuan, and S.P.A. Bordas. An alternative alpha finite element method (AαFEM) for free and forced structural vibration using triangular meshes . *Journal of Computational and Applied Mathematics*, 233(9), 2010.

[105] T. Nguyen-Thoi, G.R. Liu, K.Y. Lam, and G.Y. Zhang. A face-based smoothed finite element method (FS-FEM) for 3D linear and geometrically non-linear solid mechanics problems using 4-node tetrahedral elements. *International Journal of Numerical Methods in Engineering*, 78(3):324–353, 2009.

[106] T. Nguyen-Thoi, G.R. Liu, K.Y. Lam, and G.Y. Zhang. A face-based smoothed finite element method (FS-FEM) for 3D linear and geometrically non-linear solid mechanics problems using 4-node tetrahedral elements. *International Journal For Numerical Methods in Engineering*, 78(3):324–353, 2009.

[107] T. Nguyen-Thoi, G.R. Liu, and H. Nguyen-Xuan. Additional Properties of The Node-Based Smoothed Finite Element Method (NS-FEM) for Solid Mechanics Problems. *International Journal of Computational Methods*, 6(4):633–666, 2009.

[108] T. Nguyen-Thoi, G.R. Liu, and H. Nguyen-Xuan. A n-sided polygonal edge-based smoothed finite element method (nES-FEM) for solid mechanics. *International Journal for Numerical Methods in Biomechanical Engineering*, 27(9):1466–1472, 2011.

[109] T. Nguyen-Thoi, G.R. Liu, H. Nguyen-Xuan, and C. Nguyen-Tran. Adaptive analysis using the node-based smoothed finite element method (NS-FEM). *International Journal for Numerical Methods in Biomedical Engineering*, 27(2):198–218, 2011.

[110] T. Nguyen-Thoi, G.R. Liu, H.C. Vu-Do, and H. Nguyen-Xuan. A face-based smoothed finite element method (FS-FEM) for visco-elastoplastic analyses of 3D solids using tetrahedral mesh. *Computer Methods in Applied Mechanics and Engineering*, 198(41-44):3479–3498, 2009.

[111] T. Nguyen-Thoi, H.C. Vu-Do, T. Rabczuk, and H. Nguyen-Xuan. A node-based smoothed finite element method (NS-FEM) for upper bound solution to visco-elastoplastic analyses of solids using triangular and tetrahedral meshes. *Computer Methods in Applied Mechanics and Engineering*, 199(45-48):3005–3027, 2010.

[112] H. Nguyen Xuan. *A strain smoothing method in finite elements for structural analysis*. PhD thesis, 2008.

[113] H. Nguyen-Xuan, S. Bordas, and H. Nguyen-Dang. Smooth finite elements: incompressibility, accuracy, superconvergence, singularities and selective integration. *International Journal for Numerical Methods in Engineering*, 74(2):175–208, 2008.

[114] H. Nguyen-Xuan, S.P.A. Bordas, and H. Nguyen-Dang. Addressing volumetric locking in instabilities by selective integration in smoothed finite elements. *Communications in Numerical Methods in Engineering*, 25:19–34, 2009.

[115] H. Nguyen-Xuan and G.R. Liu. An edge-based smoothed finite element method softened with a bubble functions (bES-FEM) for solid mechanics problems. *Computers and Structures*, 128:14–30, 2013.

[116] H. Nguyen-Xuan, G.R. Liu, S. Bordas, S. Natarajan, and T. Rabczuk. An adaptive singular ES-FEM for mechanics problems with singular field of arbitrary order. *Computer Methods in Applied Mechanics and Engineering*, 253:252–273, 2013.

[117] H. Nguyen-Xuan, G.R. Liu, T. Nguyen-Thoi, and C. Nguyen-Tran. An edge-based smoothed finite element method for analysis of two-dimensional piezoelectric structures. *Smart Materials and Structures*, 18(6):065015, 2009.

[118] H. Nguyen-Xuan, G.R. Liu, C. Thai-Hoang, and T. Nguyen-Thoi. An edge-based smoothed finite element method (ES-FEM) with stabilized discrete shear gap technique for analysis of Reissner-Mindlin plates. *Computer Methods in Applied Mechanics and Engineering*, 199(9-12):471–489, 2010.

[119] H. Nguyen-Xuan, L.V. Tran, C.H. Thai, and T. Nguyen-Thoi. Analysis of functionally graded plates by an efficient finite element method with node-based strain smoothing. *Thin-Walled Structures*, 54:1–18, 2012.

[120] J.T. Oden. *Finite Elements of Nonlinear Continua*. Dover, 2006.

[121] R.W. Ogden. Large Deformation Isotropic Elasticity - On the Correlation of Theory and Experiment for Incompressible Rubberlike Solids. *Proceedings of the Royal Society A: Mathematical, Physical and Engineering Sciences*, 326(1567):565–584, 1972.

[122] R.W. Ogden. Recent Advances in the Phenomenological Theory of Rubber Elasticity. *Rubber Chemistry and Technology*, 59(3):361–383, 1986.

[123] R.W. Ogden. *Non-Linear Elastic Deformation*. Dover, second edition, 1997.

[124] R.W. Ogden, G. Saccomandi, and I. Sgura. Fitting hyperelastic models to experimental data. *Computational Mechanics*, 34(6):484–502, 2004.

[125] L. Olovsson, L. Nilsson, and K. Simonsson. An ALE formulation for the solution of two-dimensional metal cutting problems. *Computers and Structures*, 72(4-5):497–507, 1999.

[126] T.H. Ong, C.E. Heaney, C.K. Lee, H. Nguyen-Xuan, and G.R. Liu. On stability, convergence and accuracy of bES-FEM and bFS-FEM for nearly incompressible elasticity. *Computer Methods in Applied Mechanics and Engineering*, 285:315–345, 2014.

[127] T.H. Ong, G.R. Liu, T. Nguyen-Thoi, and H. Nguyen-Xuan. Inf-suf stable bES-FEM method for nearly incompressible elasticity. 2013.

[128] A. Ortiz-Bernadin, J.S. Hale, and C.J. Cyron. Meshfree volume-averaged nodal projection method for nearly-incompressible elasticity using meshfree and bubble basis functions. *Computational Methods in Applied Mechanics and Engineering*, 285:427–451, 2015.

[129] D. Pantuso and K.-J. Bathe. A four-node quadrilateral mixed-interpolated element for solids and fluids. *Mathematical Models and Methods in Applied Science*, 5(8):1113–1128, 1995.

[130] D. Pantuso and K.-J. Bathe. On the stability of mixed finite elements in large strain analysis of incompressible solids. *Finite Elements in Analysis and Design*, 28(2):83–104, 1997.

[131] M.A. Puso, J.S. Chen, E. Zywicz, and W. Elmer. Meshfree and finite element nodal integration methods. *International Journal for Numerical Methods in Engineering*, 74(3):416–446, 2008.

[132] M.A. Puso and J. Solberg. A stabilized nodally integrated tetrahedral. *International Journal for Numerical Methods in Engineering*, 67(6):841–867, 2006.

[133] R. Rannacher. A posteriori error estimation in least-squares stabilized finite element schemes. *Computer Methods in Applied Mechanics and Engineering*, 166(1-2):99–114, 1998.

[134] J.-F. Remacle and J. Lambrechts. Fast and robust mesh generation on the sphere Application to coastal domains. *Computational Geometry*, arXiv:1607.02052, 2016.

[135] R.S. Rivlin. Large Elastic Deformation of Isotropic Materials. IV. Further Developments of the General Theory. *Philosophical Transactions of the Royal Society A: Mathematical, Physical and Engineering Sciences*, 241(835):379–397, 1948.

[136] R.S. Rivlin and D.W. Saunders. Large Elastic Deformations of Isotropic Materials. VII. Experiments on the Deformation of Rubber. *Philosophical Transactions of the Royal Society A: Mathematical, Physical and Engineering Sciences*, 243(865):251–288, 1951.

[137] H. Saraf, K.T. Ramesh, A.M. Lennon, A.C. Merkle, and J.C. Roberts. Mechanical properties of soft human tissues under dynamic loading. *Journal of Biomechanics*, 40(9):1960–1967, 2007.

[138] J. Sarrate, A. Huerta, and J. Donea. Arbitrary Lagrangian-Eulerian formulation for fluid-rigid body interaction. *Computer Methods in Applied Mechanics and Engineering*, 190(24-25):3171–3188, 2001.

[139] J. Schröder, P. Wriggers, and D. Balzani. A new mixed finite element based on different approximations of the minors of deformation tensors. *Computer Methods in Applied Mechanics and Engineering*, 200(49-52):3583–3600, 2011.

[140] A.P.S Selvadurai. Deflections of a rubber membranes. *Journal of the Mechanics and Physics of Solids*, 54(6):1093–1119, 2006.

[141] R. Sevilla, S. Fernádez-Méndez, and A. Huerta. NURBS-enhanced finite element methods (NEFEM). *International Journal for Numerical Methods in Engineering*, 76(1):56–83, 2008.

[142] J.C. Simo, R.L. Taylor, and K.S. Pister. Variational and projection methods for the volume constraint in finite deformation elasto-plasticity. *Computer Methods in Applied Mechanics and Engineering*, 51:177–208, 1985.

[143] MSC Software. Nonlinear Finite Element Analysis of Elastomers, 2005.

[144] M. Souli, A. Ouahsine, and L. Lewin. ALE formulation for fluid-structures interaction problems. *Computer Methods in Applied Mechanics and Engineering*, 190(5-7):659–675, 2000.

[145] M. Souli and I. Shahrour. Arbitrary Lagrangian Eulerian formulation for soil structure interaction problems. *Soli Dynamics and Earthquake Engineering*, 35:72–79, 2012.

[146] M. Souli and J.P. Zolesio. Arbitrary Lagrangian-Eulerian and free surface methods in fluid mechanics. *Computer Methods in Applied Mechanics and Engineering*, 191(3-5):451–466, 2001.

[147] N. Sukumar and A. Tabarraei. Conforming polygonal finite elements. *International Journal for Numerical Methods in Engineering*, 61(12):2045–2066, 2004.

[148] K.Y. Sze, J.S. Chen, N. Sheng, and X.H. Liu. Stabilized conforming nodal integration: exactness and variational justification. *Finite Elements in Analysis and Design*, 41(2):147–171, 2004.

[149] C. Talischi, G.H. Paulino, A. Pereira, and I.F.M. Menezes. PolyMesher: A general-purpose mesh generator for polygonal elements written in Matlab. *Journal of Structural and Multidisciplinary Optimization*, 45(3):309–328, 2012.

[150] R.L. Taylor. A mixed-enhanced formulation for tetrahedral finite elements. *International Journal for Numerical Methods in Engineering*, 47(1-3):205–227, 2000.

[151] C. Truesdell. *The Mechanical Foundations of Elasticity and Fluid Dynamics*. Gordon and Breach Publishers, Inc., 1966.

[152] D. Wang and J.-S. Chen. Locking-free stabilized conforming nodal integration for meshfree Mindlin-Reissner plate formulation. *Computer Methods in Applied Mechanics and Engineering*, 193(12-14):1065–1083, 2004.

[153] J. Wang and M.S. Gadala. Formulation and survey of ALE method in nonlinear solid mechanics. *Finite Elements in Analysis and Design*, 24(4):253–269, 1997.

[154] A. Wineman. Some results for generalized neo-Hookean elastic materials. *International Journal of Non-Linear Mechanics*, 40(2-3):271–279, 2005.

[155] P. Wriggers and S. Reese. A note on enhanced strain methods for large deformations. *Computer Methods in Applied Mechanics and Engineering*, 135(3-4):201–209, 1996.

[156] C.T. Wu, W. Hu, and G.R. Liu. Bubble-enhanced smoothed finite element formulation: a variational multi-scale approach for volume-constrained problems in two-dimensional linear elasticity. *International Journal for Numerical Methods in Engineering*, 2014.

[157] C.T. Wu and H.P. Wang. An enhanced cell-based smoothed finite element method for the analysis of Reissner-Mindlin plate bending problems involving distorted mesh. *International Journal for Numerical Methods in Engineering*, 95(4):288–312, 2013.

[158] H. Yamaguchi and A. Takushima. Simulating interfacial deformation by arbitrary Lagrangian-Eulerian approach. *Computer Methods in Applied Mechanics and Engineering*, 193(39-41):4439–4456, 2004.

[159] L.Y. Yao, D.J. Yu, X.Y. Cui, and X.G. Zang. Numerical treatment of acoustic problems with the smoothed finite element method. *Applied Acoustics*, 71(8):743–753, 2010.

[160] O.H. Yeoh. Some forms of the strain energy function for rubber. *Rubber Chemistry and Technology*, 66(5):754–771, 1993.

[161] J.W. Yoo, B. Moran, and J.-S. Chen. Stabilized conforming nodal integration in the natural-element method. *International Journal for Numerical Methods in Engineering*, 60(5):861–890, 2004.

[162] Q. Zhang and T. Hisada. Analysis of fluid-structure interaction problems with structural buckling and large domain changes by ALE finite element method. *Computer Methods in Applied Mechanics and Engineering*, 190:6341–6357, 2001.

[163] Z.-Q. Zhang and G.R. Liu. Temporal stabilization of the node-based smoothed finite element method and solution bound of linear elastostatics and vibration problems. *Computational Mechanics*, 46(2):229–246, 2010.

[164] Z.-Q. Zhang and G.R. Liu. Upper and lower bounds for natural frequencies: A property of the smoothed finite element method. *International Journal for Numerical Methods in Engineering*, 84(2):149–178, 2010.

[165] Z.-Q. Zhang and G.R. Liu. An edge-based smoothed finite element method (ES-FEM) using 3-node triangular elements for 3D non-linear analysis of spatial membrane structures. *International Journal of Numerical Methods in Engineering*, 86(2):135–154, 2011.

[166] X. Zhao, S.P.A. Bordas, and J. Qu. A hybrid smoothed extended finite element/level set method for modelling equilibrium shapes of nano-inhomogeneities. *Computational Mechanics*, 52(6):1417–1428, 2013.

[167] O.C. Zienkiewicz, J. Rojek, R.L. Taylor, and M. Pastor. Triangles and tetrahedra in explicit dynamic codes for solids. *International Journal for Numerical Methods in Engineering*, 43(3):565–583, 1998.